NAVAL POSTGRADUATE SCHOOL
Monterey, California

AD-A262 150

THESIS

ALONGSHORE SUB-THERMOCLINE CURRENT VARIABILITY IN THE CENTRAL CALIFORNIA CURRENT SYSTEM

by

Michael R. Hicks

December 1992

Thesis Advisor: Steven R. Ramp

Approved for public release; distribution is unlimited

93-06697

REPORT DOCUMENTATION PAGE

1a. REPORT SECURITY CLASSIFICATION Unclassified		1b. RESTRICTIVE MARKINGS		
2a. SECURITY CLASSIFICATION AUTHORITY		3. DISTRIBUTION/AVAILABILITY OF REPORT Approved for public release; distribution is unlimited.		
2b. DECLASSIFICATION/DOWNGRADING SCHEDULE				
4. PERFORMING ORGANIZATION REPORT NUMBER(S)		5. MONITORING ORGANIZATION REPORT NUMBER(S)		
6a. NAME OF PERFORMING ORGANIZATION Naval Postgraduate School	6b. OFFICE SYMBOL (If applicable) OC	7a. NAME OF MONITORING ORGANIZATION Naval Postgraduate School		
6c. ADDRESS (City, State, and ZIP Code) Monterey, CA 93943-5000		7b. ADDRESS (City, State, and ZIP Code) Monterey, CA 93943-5000		
8a. NAME OF FUNDING/SPONSORING ORGANIZATION	8b. OFFICE SYMBOL (If applicable)	9. PROCUREMENT INSTRUMENT IDENTIFICATION NUMBER		
8c. ADDRESS (City, State, and ZIP Code)		10. SOURCE OF FUNDING NUMBERS		

	Program Element No.	Project No.	Task No	Work Unit Accession Number

11. TITLE (Include Security Classification)
ALONGSHORE SUB-THERMOCLINE VARIABILTY IN THE CENTRAL CALIFORNIA CURRENT SYSTEM

12. PERSONAL AUTHOR(S) Hicks, Michael Robert

13a. TYPE OF REPORT Master's Thesis	13b. TIME COVERED From To	14. DATE OF REPORT (year, month, day) December 1992	15. PAGE COUNT 126

16. SUPPLEMENTARY NOTATION
The views expressed in this thesis are those of the author and do not reflect the official policy or position of the Department of Defense or the U.S. Government.

17. COSATI CODES			18. SUBJECT TERMS (continue on reverse if necessary and identify by block number)
FIELD	GROUP	SUBGROUP	California Current, California Undercurrent, coastal trapping, Monterey Bay Meander

19. ABSTRACT (continue on reverse if necessary and identify by block number)

Moored current meter observations were made along the central California contintental slope from Pt. Piedras Blancas to the Farallon Islands. The study area covered an alongshore distance of approximately 290 km and examined the data from off Pt. Piedras Blancas (P4), Pt. Sur (P2 and P3), Monterey Bay (MB1 and MB2) and the Farallon Islands (D and E). Time and frequency domain analyses were performed on three time segments that included data from combinations of the above mooring locations based on common time periods and depths (350 - 500 m). Segment 1 revealed a mean poleward flow attributed to the California Undercurrent at all moorings. Segment 2 had a similar mean poleward flow but also exhibited an equatorward reversal at periods between 19.5 and 58.5 days at P2 and MB2 that was less apparent at P3 further offshore and appeared to be coastally trapped. Observed wavelengths were compared with simple wave theory indicating that the observed signal may have resulted from a combination of two theories i.e. a coastally trapped wave. The complex bottom topography between Pt. Sur and the Monterey Bay prohibited more rigorous comparison between theory and the observations. Satellite sea surface temperature imagery during Segment 3 showed an anti-cyclonic meander with a 65 km radius outside of the Monterey Bay. Current and temperature records at P2 and MB2 indicated that the surface feature's position varied and influenced the currents at depths down to 500 m. Time domain empirical orthogonal functions were calculated for alongshore and across-shore components separately. The first two empirical modes accounted for between 81% and 86% of the alongshore variance in all segments and were attributed to the California Undercurrent (mode 1) and to the deviations from the mean state (mode 2). The first two across-shore modes explained between 66% and 81% of the variance and consistently demonstrated opposing current structure between the Pt. Sur and Monterey Bay moorings, likely due to the Monterey Bay meander influence.

20. DISTRIBUTION/AVAILABILITY OF ABSTRACT ☒ UNCLASSIFIED/UNLIMITED ☐ SAME AS REPORT ☐ DTIC USERS	21. ABSTRACT SECURITY CLASSIFICATION Unclassified	
22a. NAME OF RESPONSIBLE INDIVIDUAL Steven R. Ramp	22b. TELEPHONE (Include Area code) (408) 646-3162	22c. OFFICE SYMBOL OC/Ra

DD FORM 1473, 84 MAR   83 APR edition may be used until exhausted   SECURITY CLASSIFICATION OF THIS PAGE
All other editions are obsolete   Unclassified

Alongshore Sub-Thermocline Variability
in the Central California Current System

by

Michael R. Hicks
Lieutenant, United States Coast Guard
B.S., United States Coast Guard Academy, 1986

Submitted in partial fulfillment
of the requirements for the degree of

MASTER OF SCIENCE IN PHYSICAL OCEANOGRAPHY

from the

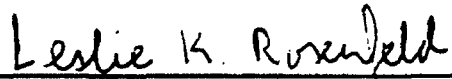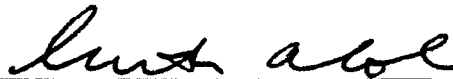NAVAL POSTGRADUATE SCHOOL
December 1992

Author: _____
Michael R. Hicks

Approved by: _____
Steven R. Ramp, Thesis Advisor

_____
Leslie K. Rosenfeld, Second Reader

_____
Curtis A. Collins, Chairman
Department of Oceanography

ABSTRACT

Moored current meter observations were made along the central California continental slope from Pt. Piedras Blancas to the Farallon Islands. The study area covered an alongshore distance of approximately 290 km and examined the data from off Pt. Piedras Blancas (P4), Pt. Sur (P2 and P3), Monterey Bay (MB1 and MB2) and the Farallon Islands (D and E). Time and frequency domain analyses were performed on three time segments that included data from combinations of the above mooring locations based on common time periods and depths (350 m - 500 m). Segment 1 revealed a mean poleward flow attributed to the California Undercurrent at all moorings. Segment 2 had a similar mean poleward flow but also exhibited an equatorward reversal at periods between 19.5 and 58.5 days at P2 and MB2 that was less apparent at P3 further offshore and appeared to be coastally trapped. Observed wavelengths were compared with simple wave theory indicating that the observed signal may have resulted from a combination of two theories i.e. a coastally trapped wave. The complex bottom topography between Pt. Sur and the Monterey Bay prohibited more rigorous comparison between theory and the observations. Satellite sea surface temperature imagery during Segment 3 showed an anti-cyclonic meander with a 65 km radius outside of the Monterey Bay. Current and temperature records at P2 and

iii

For
'A&I
B
:ed

Distribution /

Availability Codes

Dist	Avail and / or Special
A-1	

DTIC QUALITY

MB2 indicated that the surface feature's position varied and influenced the currents at depths down to 500 m. Time domain empirical orthogonal functions were calculated for alongshore and across-shore components separately. The first two empirical modes accounted for between 81% and 86% of the alongshore variance in all segments and were attributed to the mean California Undercurrent influence (mode 1) and to the deviations from the mean state (mode 2). The first two across-shore modes explained between 66% and 81% of the variance and consistently demonstrated opposing current structures between the Pt. Sur and Monterey Bay moorings, likely due to the Monterey Bay meander influence.

TABLE OF CONTENTS

LIST OF TABLES

LIST OF FIGURES

ACKNOWLEDGMENTS

I. INTRODUCTION

A. EXPERIMENT BACKGROUND

The paper's objective is to examine and describe the alongshore variability of sub-thermocline currents (350 m - 500 m) over the California continental slope. The investigation employs conventional frequency domain (spectral) analysis as well as time domain empirical orthogonal function (EOF) analysis to provide a detailed picture of three different time segments. The analysis incorporated current meter data from several moorings between Point Sur and the Farallon Islands along the California coast (Figure 1). The study encompassed an alongshore distance of approximately 290 km. All moorings were deployed on the middle slope between the 800 m and 2000 m isobaths. Mooring P4, the furthest south of all moorings was located off Point Piedras Blancas, approximately 100 km to the south of Point Sur. Two moorings, P2 and P3 were positioned off Point Sur. Mooring P3, provided data from the lower continental slope (1800 m) while P2, approximately 26 km east of P3, was positioned over the upper slope (800 m). MB2, located 41 km to the north of P2, was positioned outside of the Monterey Bay (1979 m) while MB1, approximately 31 km to the east of MB2 was inside the Monterey Bay over the axis of the Monterey Canyon. Positioned

1
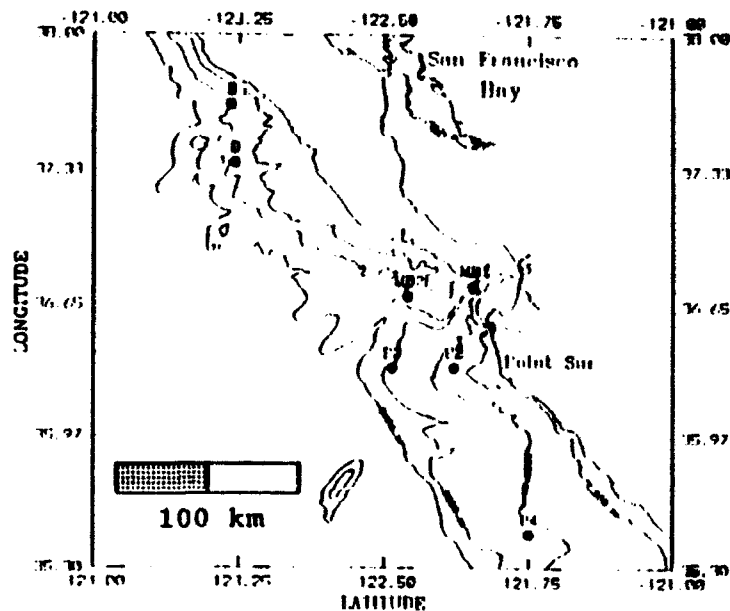
Figure 1. **Current Meter Mooring Locations:** A map of the central California coastal region. Moorings are shown as solid circles with alphanumeric labels.

approximately 111 km to the north of MB2, mooring D marked the southern boundary of the Farallon Islands data set. Finally, mooring E was located 32 km north of D in the vicinity of the Farallon Islands outside San Francisco Bay. (Figure 1)

The analysis of alongshore propagation required common time segments from each location. Various organizations collected data for different purposes, limiting the number of common time segments available. Instruments at depths between 350 m and 500 m provided the most continuous alongshore data records so the analysis focused on these depths. The experiment used three segments of 110, 199 and 177 days that spanned an overall time period from December 1989 to November 1991 (Figure 2).

2

SEGMENT 1 SEGMENT 2 SEGMENT 3

17 DEC 89-04 APR 90 14 AUG 90-17 MAR 91 24 MAY 91-14 NOV 91
(119 DAYS) (199 DAYS) (177 DAYS)

POINT PIEDRAS BLANCAS DATA

P4 350 m

P4 500 m

POINT SUR DATA

P2 350 m P2 350 m P2 350 m

P2 500 m   P2 500 m

P3 350 m P3 350 m

P3 500 m

MONTEREY BAY DATA

MB1 500 m MB1 500 m MB1 500 m

MB3 416 m MB3 416 m

FARALLON DATA

F 500 m

F 500 m
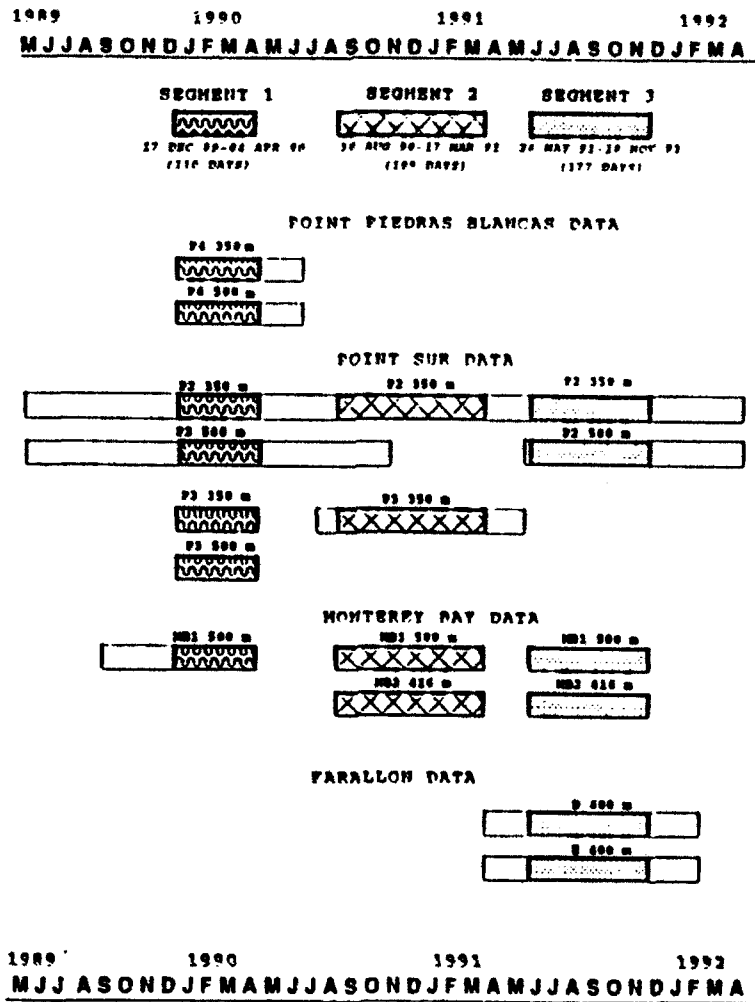
Figure 2. **Current Meter Time Line**: Common time periods are labeled as Segments 1, 2 and 3 and are shown by different cross-hatching styles.

The remainder of this chapter provides background information on the California Current System and describes various deviations from the mean flow observed there. A discussion on coastal trapped waves is presented here to include the derivation of the dispersion relationship for internal Kelvin waves. The second and third chapters review data collection and analysis techniques respectively. The fourth chapter presents the results and is followed by a

3

discussion chapter that applies theory to the observations. The final chapter gives the conclusions with recommendations for future research.

B. THE CALIFORNIA CURRENT SYSTEM

1. The Mean State

The data were collected from within the California Current System (CCS), the eastern boundary current of the North Pacific gyre. This sub-tropical gyre consists of an anti-cyclonic surface flow bounded by the westward flowing North Equatorial Current (20° N) to the south, the poleward flowing Kuroshio current to the west and the West Wind Drift to the north. When the West Wind Drift strikes the North American continent, it splits to the north to feed the poleward flowing Alaskan current and to the south to form the California Current. (Wooster and Reid, 1963)

Large scale atmospheric forcing creates this anti-cyclonic circulation. During the Coastal Ocean Dynamics Experiments (CODE 1 in 1981 and CODE 2 in 1982), Halliwell and Allen (1987) attribute persistent, summertime equatorward wind stress to the interaction of the North Pacific subtropical high with the persistent low over the southwestern United States. The pressure differences between these two stationary systems are largest during the summer and hence equatorward wind stress is also largest in summer (Huyer, 1983). Huyer (1983) describes the southwestward migration of the

subtropical high to about 28° N in February. Halliwell and Allen (1987) attribute winter time poleward wind stress to northward propagating cyclones and anti-cyclones. In general, atmospheric forcing drives an equatorward surface flow during summer which is often described as slow, broad and shallow (Wooster and Reid 1963). When these equatorward winds relax, the current reverses within 150 km of the coast (Winant et al., 1987; Chelton et al., 1988). This winter reversal is known as the California Countercurrent or the Davidson Current north of Point Conception (Chelton, 1984).

Since this paper focused on the 350 m to 500 m depth interval, the poleward flowing California Undercurrent (CUC) influenced the data set more than any other feature of the CCS. Hickey (1979) observed the CUC at a depth of 300 m off southern Washington in 1972. Chelton (1984) also observed this flow off central California and found an annual variation at Point Sur, in contrast with the semi-annual variation in the northern CCS such as that observed by Hickey (1979). Wickham et al. (1987) observed a "jet-like core" with velocity greater than 15 cm/s confined to within 30 km of the coast near Point Sur. Like Chelton (1984), they also found that the CUC varied annually with maximum poleward currents during May and June of 1979 and 1980. Chelton et al. (1988) found poleward flowing currents from the surface down to 400 m as far as 100 km beyond the central California shelf break during the summer of 1981 and 1984. They attributed this unusual

5

occurrence to an extended period of anomalously weak summertime equatorward winds. Such poleward flow had been previously observed only during winter as the Davidson Current.

Hickey (1989) studied the shelf and slope undercurrent off Washington and the Southern California Bight, nearly encompassing the entire CCS. Of particular relevance to this paper, Hickey discussed interruptions or anomalous cases where the generally poleward flowing undercurrent became equatorward. For example, in winter off Washington, alongshore wind stress and pressure gradient were opposite in direction and reversed from the summer case creating a wintertime equatorward undercurrent off the Washington slope. Additionally, Huyer et al., (1984) related equatorward flow over the slope to the presence of an eddy. Equatorward deviations likewise occurred in this data set and will be discussed on a case by case basis.

2. The Baroclinic Equatorward Jet

Contrary to Wooster and Reid's (1963) California surface current description, data from the Coastal Transition Zone (CTZ) experiment revealed a strong baroclinic jet (core speed > 50 cm s^{-1}) between 37° N and 38° N (Ramp et al., 1991; Huyer et al., 1991; Kosro et al., 1991). Huyer et al. (1991) superimposed acoustic doppler current profiler (ADCP) vectors onto satellite imagery and clearly showed a highly energetic

meandering surface flow. This jet displaced isopycnals to depths greater than 500 m (Ramp et al., 1991). Daggett (1989) combined CTD and ADCP data to describe an equatorward meandering jet off Point Arena, California during CTZ. Equatorward velocity in excess of 25 cm sec^{-1} was observed in a shallow (50 m) core with weaker equatorward flow extending down to 500 m. Additionally, in May 1988 Tisch (1990) observed an equatorward jet with velocity exceeding 25 cm sec^{-1} off Point Sur down to 200 m. This flow was attributed to strong (-2.0 dyne cm^{-2}) wind stress present during the week prior to hydrographic observations. In November 1988, equatorward geostrophic velocity was observed from the surface to depths exceeding 600 m (Tisch 1990). This paper provides additional evidence that an onshore meandering of this equatorward jet can interrupt the otherwise persistent poleward flow at depths down to 500 m (Chapter IV).

3. Low Frequency Current Fluctuations

In addition to the baroclinic jet interaction, several researchers have observed more periodic current fluctuations at periods from 5 to 40 days. Kundu, Allen and Smith (1975) compared dynamic and empirical modes of the velocity field near the Oregon coast. Although their observations were limited to the shelf (100 m), they found high mutual coherence between the wind stress and barotropic u and v modes at periods between 7 and 16 days. Battisti and Hickey (1984)

found significant coherence between two synthetic sub-surface pressure (SSP) levels over the entire low frequency spectrum band for coastally trapped waves (CTW) with periods greater than 5 days. They calculated the o..shore-vertical structure and dispersion relationship of a free CTW and compared model results with observations. Again, these results were largely confined to the surface flow.

Romea and Allen (1983) used an f-plane model to study vertically propagating, coastal trapped, internal Kelvin waves (IKW). They paid particular attention to low frequency behavior with periods between 20 and 40 days, using three different types of wind forcing: an impulse wind at a point, a steady wind at a point, and a travelling wind. Their model showed that poleward travelling winds forced vertically propagating IKW while equatorward travelling winds forced waves that became surface trapped. They addressed the circumstances under which waves may propagate vertically without dissipation and their results will be compared to the observations in this paper in greater detail. Vertical IKW propagation must be considered here as it provides a viable means by which a remotely forced wave could propagate between Point Sur and the Monterey Bay. Denbo and Allen (1987), Chapman (1987) and Lopez and Clarke (1989) found that remote atmospheric forcing to the south was an important source of current variability on the western U.S. continental shelf.

8

C. COASTAL TRAPPED WAVE THEORY

A coherent, low frequency fluctuation (T ≈ 19-29 days) persisted during the second time segment of this paper's data set. The dispersion relationships for simple internal Kelvin waves and barotropic continental shelf waves are presented as possible points of comparison for these observations.

By using the inviscid momentum equations with the continuity equation, a series of wave-like solutions whose amplitudes decay exponentially with distance from a straight coastline can be produced. These solutions are generally referred to as "coastal trapped waves" (CTW) (Huyer, 1990). Huyer (1990) described two extreme types of CTW. On one extreme is the continental shelf wave (CSW) which assumes a homogeneous fluid and relies solely on a sloping bottom for trapping. This wave is also referred to as a topographic Rossby wave and has the following dispersion relationship (Gill 1982):

$$\omega = \frac{2fk\lambda}{(k^2 + l^2 + \lambda^2)}$$

where ω is the wave frequency in radians sec^{-1}, f is the Coriolis parameter, k and l are the across-shore and alongshore wave numbers respectively and λ is the bottom slope parameter $= -\frac{1}{H}\frac{dH}{dx}$, where x is the distance offshore and

H is the bottom depth. The derivation of this relationship

9

assumes a depth which increases exponentially with distance from the coast.

On the other extreme, Kelvin wave theory assumes a flat bottom with a vertical boundary to trap waves of sufficiently low frequencies i.e., $\omega \ll f$. Internal Kelvin waves (IKW) represent the higher order modes of the Kelvin wave solution and depend only on the fluid's density stratification (Huyer, 1990). The IKW dispersion relationship is derived below following Gill (1982):

Applying a vertical boundary at $x = 0$, all u (across-shore) components equal zero (i.e., current may not flow into the wall) and the following governing equations result:

$$-fv = -\frac{1}{\rho} \frac{\partial p}{\partial x} \tag{1}$$

$$\frac{\partial v}{\partial t} = -\frac{1}{\rho} \frac{\partial p}{\partial y} \tag{2}$$

$$\frac{\partial w}{\partial t} = -\frac{1}{\rho} \frac{\partial p}{\partial z} - \frac{\rho' g}{\rho_o} \tag{3}$$

$$\frac{\partial v}{\partial y} + \frac{\partial w}{\partial z} = 0 \tag{4}$$

$$\frac{\partial \rho'}{\partial t} + w \frac{\partial \rho_o}{\partial z} = 0 \qquad (5)$$

Equations (1) through (3) represent u, v, and w momentum respectively while (4) and (5) represent continuity and the equation of state respectively. They assume an incompressible, inviscid linear flow where x, y, z, u, v, and w refer to the alongshore, across-shore and vertical directions and velocity components respectively, p is pressure, ρ_o is the mean density under the Boussinesq approximation, $\frac{\rho' g}{\rho_o}$ is the reduced gravity (i.e., assuming water column is stratified), f is the Coriolis parameter, and t is time.

A pressure response form similar to that of Battisti and Hickey (1984)

$$p = P(z) \; e^{-kx} \; e^{i[ly - \omega t]} \qquad (6)$$

is assumed where ω equals wave frequency in radians sec^{-1}. Solving for v from equation (2) yields:

$$v = \frac{l}{\omega \rho_o} P(z) e^{-kx} e^{i[ly - \omega t]} \qquad (7)$$

Combining equations (3) and (5) produces a second order, linear differential equation for w:

11

$$\frac{\partial^2 w}{\partial t^2} + N^2 w = \frac{-i\omega}{\rho_o} \frac{dP}{dz} e^{-kx} e^{i[ly-\omega t]} \qquad (8)$$

Where N^2 is the Brunt-Vaisala frequency equal to $g[-\frac{1}{\rho_o} \frac{\partial \rho_o}{\partial z}]$ in

radians sec^{-1}. Solving for w:

$$w = \frac{i\omega}{\rho_o (N^2 - \omega^2)} \frac{dp}{dz} \qquad (9)$$

The v and w velocities are then eliminated by substituting (7) and (9) into (4) producing a second order differential equation in P:

$$\frac{d^2P}{dz^2} + \frac{l^2(N^2 - \omega^2)}{\omega^2} P = 0 \qquad (10)$$

The rigid lid and flat bottom boundary conditions state that w = 0 at z = 0 and -H (where H is the bottom depth). The solution to equation (10) takes a sinusoidal form and applying the above boundary conditions yields:

$$\frac{l^2(N^2 - \omega^2)}{\omega^2} = \left(\frac{n\pi}{H}\right)^2 \qquad (11)$$

where n is the internal mode number. Finally, solving for ω^2:

$$\omega^2 = \frac{l^2 N^2}{\left(\frac{n\pi}{H}\right)^2 + l^2} \qquad (12)$$

This relationship and that for a CSW are used to examine the coherent low frequency current fluctuations observed during Segment 2 of the data set (Chapter V).

II. DATA COLLECTION

A. CURRENT METER DATA

Current data were collected at seven different sites from Pt. Piedras Blancas to the Farallon Islands. Three separate time segments were chosen based on common periods when the data overlapped. Tables 1 through 3 summarize these segments.

TABLE 1. **CURRENT METER MOORING LOCATIONS AND DATA SOURCES: SEGMENT 1 (17 DEC 89 - 06 APR 90).**

Mooring	Bottom depth (m)	Meter depth (m)	Latitude	Longitude	Current Meter Type	Rotation Axis (° T)	Data Source
P4	1090	350	35° - 28.3'N	121° - 44.9'W	RCM 8	354	NPS
P4	1090	500	35° - 28.3'N	121° - 44.9'W	RCM 8	354	NPS
P2	800	350	36° - 20.0'N	122° - 10.2'W	RCM 8	344	NPS
P2	800	500	36° - 20.0'N	122° - 10.2'W	RCM 8	344	NPS
P3	1800	350	36° - 20.0'N	122° - 27.6'W	RCM 8	344	NPS
P3	1800	500	36° - 20.0'N	122° - 27.6'W	RCM 8	344	NPS
MB1	650	500	36° - 44.3'N	122° - 02.4'W	RCM 5	322	MBARI

Since current meter depths from 350 m to 500 m provided the most complete and continuous data set, the analysis focused on these depths. Although other current meters were deployed, only the instruments at the common depths of interest are shown. Most of the data were collected with the Aanderaa RCM 8 current meter with exceptions noted in Tables 1-3.

13

Table 2. **CURRENT METER MOORING LOCATIONS AND DATA SOURCES:** SEGMENT 2 (30 AUG 90 - 17 MAR 91).

Mooring	Bottom depth (m)	Meter depth (m)	Latitude	Longitude	Current Meter Type	Rotation axis (° T)	Data Source
P2	807	350	36° - 20.1'N	122° - 10.3'W	RCM 8	344	NPS
P3	1800	350	36° - 20.1'N	122° - 27.6'W	RCM 8	344	NPS
MB1	650	506	36° - 44.3'N	122° - 02.4'W	RCM 5	322	MBARI
MB2	1979	416	36° - 42.5'N	122° - 22.5'W	RCM 5	344	MBARI

Table 3. **CURRENT METER MOORING LOCATIONS AND DATA SOURCES:** SEGMENT 3 (26 MAY 91 - 18 NOV 91).

Mooring	Bottom depth (m)	Meter depth (m)	Latitude	Longitude	Current Meter Type	Rotation axis (° T)	Data Source
P2(INT)	807	400*	36° - 20.1'N	122° - 10.3'W	RCM 8	344	NPS
MB1	650	478	36° - 44.3'N	122° - 02.5'W	RCM 8	322	MBARI
MB2	1792	418	36° - 40.1'N	122° - 22.5'W	RCM 8	344	MBARI
D	1400	400	37° - 21.8'N	123° - 16.0'W	RCM 5	328	SAIC
E	1975	400	37° - 39.0'N	123° - 17.4'W	RCM 8	328	NPS

* Indicates linear interpolation between 350 m and 500 m

1. RCM 8 Velocity Measurements

A large vane assembly (48.5 cm by 50 cm) kept the instrument aligned into the current. A magnetic compass inside the recording unit recorded the direction of orientation via a potentiometer ring fastened to the lid of the compass. Current direction was resolved to 0.35° with an accuracy of ± 5° for current speeds from 5 to 100 cm/sec and ± 7.5° for speeds from 2.5 to 5 and 100 to 200 cm/sec (Aanderaa, 1987). Combined magnetic deviation and variation of each unit

was determined on a surveyed test bench at the Naval Postgraduate School prior to each deployment.

A shrouded paddlewheel with magnetic coupling through the top end plate measured current speeds in a range from 2 to 250 cm/sec with accuracies of ± 1 cm/sec or ± 2% of actual speed, whichever was greater. The instrument performed a vector averaging by sampling the number of rotor revolutions and direction every 36 seconds for a 30 minute sampling interval. The meter maintained and intermediately stored a running sum of North-South and East-West speed components until the data sampling interval elapsed. At this time, the resultant average speed and its angle were calculated and recorded (Aanderaa, 1987).

2. Temperature Measurements

The RCM 8 used a thermistor with a variable resistance (5700 ohm at $0°$ C and 2001 ohm at $25°$ C) for temperature measurements. The thermistor is connected in series with low range ($-2.46°$ C to $21.48°$ C), high range ($6.08°$ C to $31.04°$ C) and wide range ($-0.34°$ C to $32.17°$ C) resistors. Temperature values were then determined by various polynomials for corresponding temperature ranges based on the measured resistances. Temperature readings were resolved to 0.1% of the range and accuracy was $±0.06°$ C.

3. RCM 5/RCM 8 Differences

Current meter moorings MB1, MB2 (Pillsbury, et al., 1992) and D deployed the Aanderaa RCM 5 current meter. An older version of the RCM 8, the RCM 5 differed in several important aspects. First, instead of the solid state data storage unit (DSU) used in the RCM 8, the RCM 5 relied on a 1/4" magnetic tape and tape reader to store and retrieve data. Also, the RCM 5 used a Savonius type rotor instead of the shrouded paddlewheel used on the RCM 8. The shrouded paddlewheel was designed to eliminate the unwanted effect of pumping the Savonius rotor through vertical heave in the mooring. Additionally, the RCM 8 vane area was redesigned from that of the RCM 5 to decrease the response time for current direction shifts. Finally, the RCM 5 does not use vector averaging. It recorded speed continuously but used a snapshot direction at the end of the sampling interval, introducing possible errors in current direction measurements.

III. ANALYSIS METHODS

A. NPS DATA

1. Data Retrieval, Calibration and Editing

The Aanderaa RCM 8 used a solid state data storage unit (DSU) to record current speed and direction, temperature, pressure and, when so equipped, conductivity. The DSU had a maximum storage capacity of 65,530 ten bit words, which corresponds to seven months of data when using a sampling interval of 30 minutes. All instruments used a 30 minute sampling interval except those at the Monterey Bay moorings and mooring D, which sampled data every hour. The RCM 8 determined sampling time with an internal quartz clock. Within all operating temperatures, the clock accuracy was ± 2 sec day^{-1}.

Upon instrument retrieval, the DSUs were removed and downloaded to an IBM compatible personal computer (PC) via the DSU reader 2995. The reader converted bit codes to ASCII coded format (Aanderaa, 1987) and stored the converted data on the PC. Next, a calibration program applied conductivity, pressure, speed, time and direction calibrations to convert the raw data to engineering units of current speed (cm/s), direction (^{o}T), water temperature (^{o}C), salinity (PPT) and pressure (decibars). At this point, velocity records were

17

truncated to eliminate unusable data entries i.e., data from instrument failures and zero data records obtained before and after instrument deployment. The records were plotted and visually inspected for obvious outliers. A despiking program then checked the data to ensure all parameters were within certain tolerance ratios.

2. Filtering

A filtering program (Denbo et al., 1984) first employed a low pass (LP) Cosine-Lanczos filter (half power period at 2.9 hours) to remove high frequency noise from the data. Signals with periods greater than 3.6 hours passed unattenuated and signals with periods shorter than 2 hours were removed entirely. The program applied filtering weights to successive 25 point segments. A Lagrangian interpolation subroutine shifted the start time of the filtered series to an even hour. This interpolation scheme employed a third order polynomial whose coefficients were based on the desired fractional distance between two successive data points. Only data with 30 minute sampling intervals were LP filtered. This included Farallon (mooring E), Point Sur and Point Piedras Blancas data.

A low low pass (LLP) filter (half power period at 46.6 hours) used the output from the LP interpolated filter to form six hourly records. This filter, also a Cosine-Lanczos type, applied filtering weights to 121 point segments to

18

remove diurnal and shorter period energy as well as any inertial period energy. Monterey Bay data had an hourly sampling interval already and thus only used LLP filtering. The data sets now contained despiked 6 hourly records with tidal and inertial influences removed (Figure 3).

3. Bridging

Gaps were present in various time series due to instrument failure or during mooring turnarounds. Gaps of four days or less were bridged using a special program described below. All discontinuities greater than a few days were not filled. The bridge program first determined the width of the gap between the two input time series. With Lagrangian interpolation, the program then shifted the start time of the second series so that it started exactly 6 hours after the last time of the gap. A prediction error filter (Anderson, 1974) based on data from 25 days on either side of the gap determined the data points within the gap. The program accomplished this by extending the first time series 3/4 of the way across the gap forward in time and the second time series 3/4 of the way across the gap backwards in time. It melded the overlapping data using the prediction filter, stored the data separately, and finally combined all data to fill the gap. Tests showed that this procedure had no detrimental effects on the autospectra. The requirement for
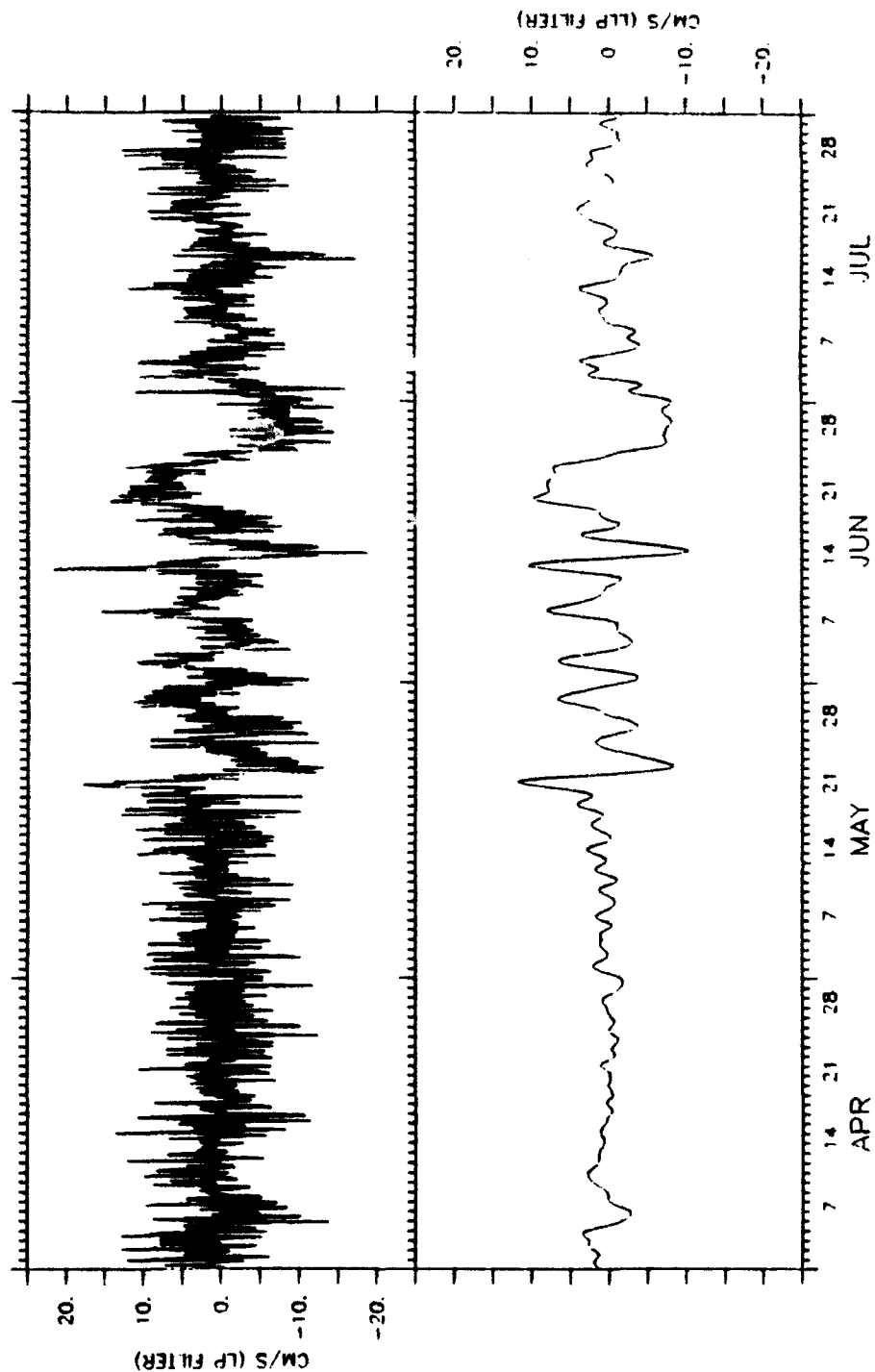
Figure 3. **Sample Current Meter Filtering:** Across-shore time series from mooring E 400 m with LP (top) and LLP filtering (bottom).

20

a continuous time series for spectral and EOF analysis made this procedure particularly useful.

4. Coordinate Axes Rotation

The interpretation of geophysical time series is often more straightforward in an alongshore vs across-shore rather than an east-north coordinate system. Thus, coordinate axes rotation facilitated across-shore vs. alongshore analysis. This procedure first required primary axis determination (Tables 1-3). A computer program determined the lengths of the semi-major axis, semi-minor axis and the angle from the positive x axis to the semi-major axis (Kundu, 1976). The program used demeaned u and v to determine the angle from the positive x axis, θ:

$$\theta = 1/2 \ \tan^{-1} \left[\frac{\frac{2}{N} \sum_{i=1}^{N} (covariance)}{\frac{1}{N} \sum_{i=1}^{N} (u_i^2 - v_i^2)} \right] \tag{13}$$

where covariance = $u_i * v_i$, u and v are the component speeds in the x and y directions respectively and N is the number of data points in the record. Based on these results, data were rotated locally with the exception of mooring P3. Because of the limited amount of data at P3 and to provide a consistent axis in the vicinity of Point Sur, P3 was rotated according to

21

the results from P2 and MB2. The rotation computed new component speeds based on

$$u_{rot} = u_o \cos(\phi) + v_o \sin(\phi)$$

$$v_{rot} = v_o \cos(\phi) - u_o \sin(\phi)$$

where u_{rot} and v_{rot} are the rotated component speed in the x and y direction respectively, u_o and v_o are the initial component speeds and ϕ is the degrees counterclockwise from true north ($\phi = 90° - |\theta|$ from equation (13) above). The rotation process concluded the preliminary data processing procedures.

B. OTHER DATA

Portions of the data were collected by organizations other than the Naval Postgraduate School (NPS). Specifically, data from the Monterey Bay moorings were generously supplied by Dr. C.H. Pilskaln of the Monterey Bay Aquarium Research Institute (MBARI). The data were received as calibrated, hourly records and were subsequently filtered to form 6-hourly records (Pillsbury et al., 1992). The data set provided a critical piece linking the Farallon Islands and Point Sur current meter moorings. Additionally, the Science Applications International Corporation (SAIC) worked in conjunction with NPS on a project that described the general circulation in the vicinity of the Farallon Islands. SAIC conducted calibration, maintenance, deployment and data

22

retrieval of all current meters at mooring D. The data at mooring D were provided by M. Noble (USGS), who carried out additional quality control, filtering and axis rotation. For continuity, all Farallon data (moorings D and E) were rotated to $328°$ T based on these results.

C. TIME DOMAIN ANALYSIS

1. Time Series Plots

Vector velocities, across-shore and alongshore velocity components and temperature time series were plotted for the common time segments. To facilitate alongshore comparisons, stack plots were formed presenting a picture of the moorings in a south to north direction; i.e., data from the southern most mooring from each segment is on top, the northern mooring on the bottom and the others in between. These plots proved critical in identifying the various events on which to focus additional analysis techniques.

2. Empirical Orthogonal Function Analysis

Time domain empirical orthogonal function (EOF) analysis (Kundu et al., 1975; Beardsley et al., 1985; Winant et al., 1987) provided a compact description of the alongshore variability of the current structure. The technique found the orthogonal eigenvectors and eigenvalues of a covariance matrix containing the desired variables. The number of time series equalled the number of eigenvalues, with each eigenvalue having a corresponding eigenvector or eigenfunction. The sum

23

of eigenvalues equalled the total variance among all components of the covariance matrix and thus each eigenvalue represented a percentage of the total variance for its corresponding mode. Modes were "ranked" according to the percent variance contained, i.e., the eigenfunction with the greatest variance was called mode 1, the next most mode 2, and so on.

The technique allows one to decompose some parameter into a few primary modes representing the essential variability. Although meteorologists first employed this technique, its applicability to ocean phenomena became quickly apparent. Kundu et al. (1975) decomposed current velocity fields off the Oregon coast into both dynamical and empirical modes. They found that the empirical modes did not depend on the accuracy of simplifying dynamical assumptions but only on the statistics of the data. They also found that empirical modes were discretely orthogonal while dynamical modes were not. Beardsley et al., (1985) used both time and frequency domains to describe current and temperature variability in the Nantucket Shoals Flux Experiment (NFSE79). Finally, Winant et al., (1987) described moored wind, temperature and current observations made during the Coastal Ocean Dynamics Experiments (CODE) 1 & 2. In all cases, these researchers described the spatial structure of multiple variables in a powerful, compact manner.

3. EOF Theory

Following Kundu et al., (1975) a brief outline of the EOF expansion technique is given. For this example, let $v_k(x_i)$ denote demeaned, alongshore velocity at time t_k ($k = 1, \ldots, K$) and at mooring location x_i ($i = 1, \ldots, N$). The matrix of time series at different mooring locations can be decomposed into a modal amplitude and a corresponding eigenfunction so that

$$v_k(x_i) = \sum_{n=1}^{N} E_k(x_i) \phi_n \quad n = 1, \ldots, N$$

where ϕ_n defines the empirical orthogonal eigenfunction and E_k the modal amplitude for each record in the time series. Determining the least squares error between the actual velocity and the summation of decomposed velocities shows that

$$\sum_{i=1}^{N} R(x_i, x_j) \phi_n(x_i) = \lambda_n \phi_n(x_j), \quad n = 1, \ldots, N$$

where

$$R(x_i, x_j) = \frac{1}{K} \sum_{k=1}^{K} v_k(x_i) v_k(x_j)$$

represents the real and symmetric covariance matrix, λ_n corresponds to each eigenvalue and ϕ_n obeys the orthogonality condition:

$$\sum_{i=1}^{N} \phi_n(x_i) \phi_m(x_i) = \delta_{m,n}$$

where $\delta_{m,n} = 1$ for m = n and 0 for m $\neq$ n. The eigenvalues, λ_n represent the time average energy in each mode i.e., the variance and the sum of the eigenvalues both equal the total energy.

A simple MATLAB function calculated the covariance matrix for the desired variables by first removing the time mean from each series. The function then found the eigenvalues λ_n, eigenvectors ϕ_n and modal amplitudes, E_k as described above.

D. FREQUENCY DOMAIN ANALYSIS

Spectral analysis employed the Fourier transform to provide energy estimates as a function of frequency. A modified version of the Matrix Laboratory (MATLAB) function, SPECTRUM computed spectral characteristics of across-shore and alongshore series. To allow investigation of the maximum frequency range without statistical degradation, the data segments were divided into five, equal length, overlapping pieces. A Hanning window, applied to each piece separately, damped the effects of the Gibbs phenomenon resulting from the

26

discontinuity created by the truncation of an infinite series. The coefficients of the Hanning window were computed by

$$w(n) = 0.5(1 - \cos(2\pi \frac{n}{N+1})), \quad n = 1, \ldots, N$$

where w represented Hanning window weights and N the number of data points in each piece.

Since the piece lengths were not powers of two, the modified program applied a mixed-base fast Fourier Transform (FFT) to each piece. The transform used by the FFT is:

$$X(k+1) = \sum_{n=0}^{N-1} x(n+1) e^{-i(2\pi/n)}$$

where X defined the transformed time series, x the Hanning windowed time series and N the number of records in each piece (Little and Shure, 1992). The program then calculated the power spectral density, cross spectral density, complex transfer function, coherence and phase functions and accumulated results from each piece. The pieces were averaged together to provide the final spectral estimates with confidence limits. Data were also plotted in variance conserving form, obtained by normalizing each spectral estimate by the frequency bandwidth and multiplying it by 2.3. The results from this and all analysis techniques are presented in Chapter IV.

IV. RESULTS

Each time segment presented its own unique results. Specifically, currents appeared to vary seasonally between each segment. Fluctuations could have been influenced by surface seasonal transitions or perhaps deeper current variations. This seasonality coupled with distinct, mesoscale deviations from the mean flow made it sensible to describe each segment separately.

A. SEGMENT 1

The first time segment included data from 17 December 1989 through 04 April 1990 (110 days) (Figure 2). Data were collected from current meters at P4 off Pt. Piedras Blancas, P2 and P3 off Pt. Sur and MB1 in Monterey Bay. Instruments at 350 m and 500 m provided data at all moorings except MB1 (500 m only). P4 was located approximately 100 km to the south of Pt. Sur and 47 km offshore along the 1100 m isobath. Located in 650 m of water, MB1 was 35 km to the north of Pt. Sur, 14 km offshore and very close to the axis of the Monterey Canyon. P2 was positioned 24 km offshore and 13 km from the shelf break (200 m isobath). Figure 4 schematically illustrates mooring locations and separation distances.
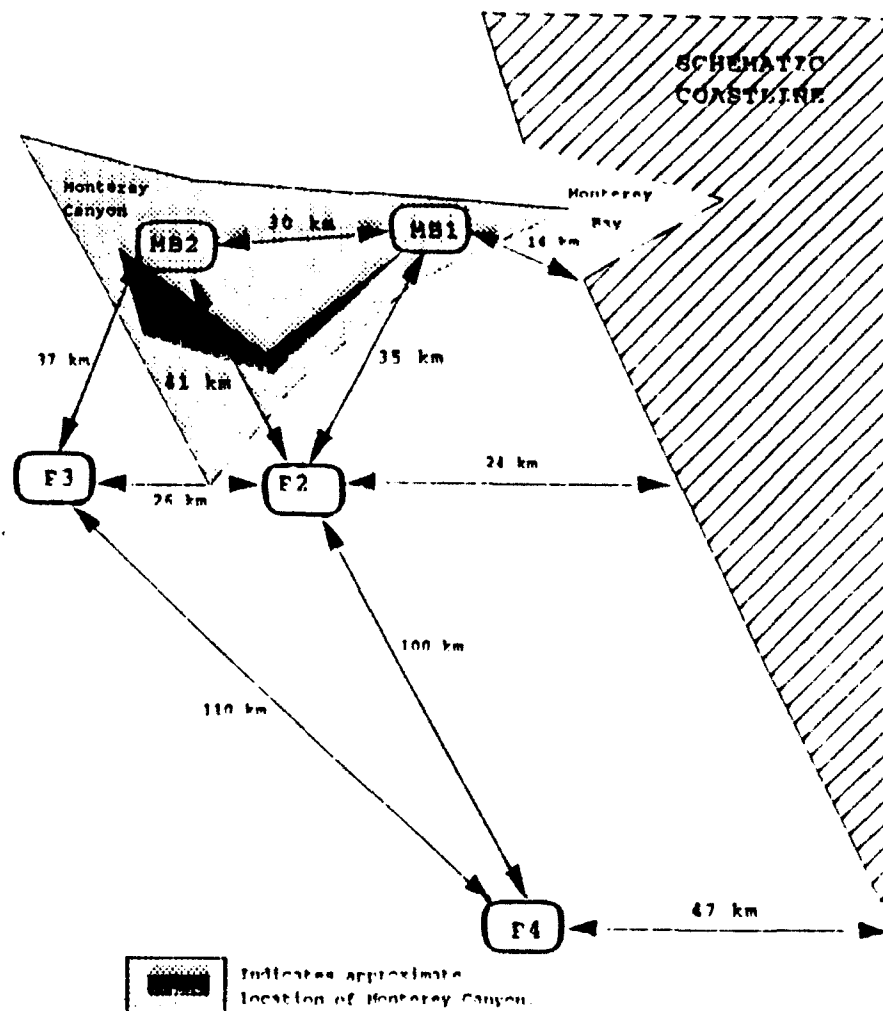
Figure 4. **Segment 1 Mooring Separation Distances:**
Alongshore and offshore distances are shown with
the approximate relative position of the Monterey
Canyon. The canyon axis is indicated by the
darker shading.

1. Time Domain Analysis

Basic time domain current statistics for Segment 1 were calculated for the time period (Tables 4a and 4b) and are described for each mooring below. At P4, basic statistics showed a mean alongshore (ALS) component speed of approximately 1.5 cm sec^{-1} at both depths with a maximum of 14.4 cm sec^{-1} and a minimum of -10.3 cm sec^{-1} (Table 4a). The across-shore (ACS) component mean (-1 cm sec^{-1}) was offshore at both depths but is likely within the error of the axis rotation. Mean currents were primarily in the alongshore direction. The maximum offshore current was -11.9 cm sec^{-1} while the maximum onshore current was 5.9 cm sec^{-1} (Table 4b). From 17 December until 06 January, a vertical shear existed at P4 between 350 m and 500 m with poleward flow at 350 m and equatorward flow at 500 m (Figures 5 and 6). Flow became equatorward at both depths from 06 to 16 January when it turned poleward until late winter. Around 08 March, the current shifted to equatorward and remained so until the end of the segment. The currents looked coherent vertically from 06 January to the end of the segment.

30

Figure 5.   **Segment 1 Vector Velocities (350 m):** Velocity
vectors are shown in cm sec^{-1} with poleward
alongshore, as defined in text, towards the top
of the plot. Data are from P4 (top), P2 (middle)
and P3 (bottom).

31

Figure 6. **Segment 1 Vector Velocities (500 m):** Same as Figure 5, except for the 500 m depth level. The data from MB1 (bottom) are also included in this figure.

Table 4a. **TIME DOMAIN STATISTICS FOR SEGMENT 1**
(ALONGSHORE COMPONENT)

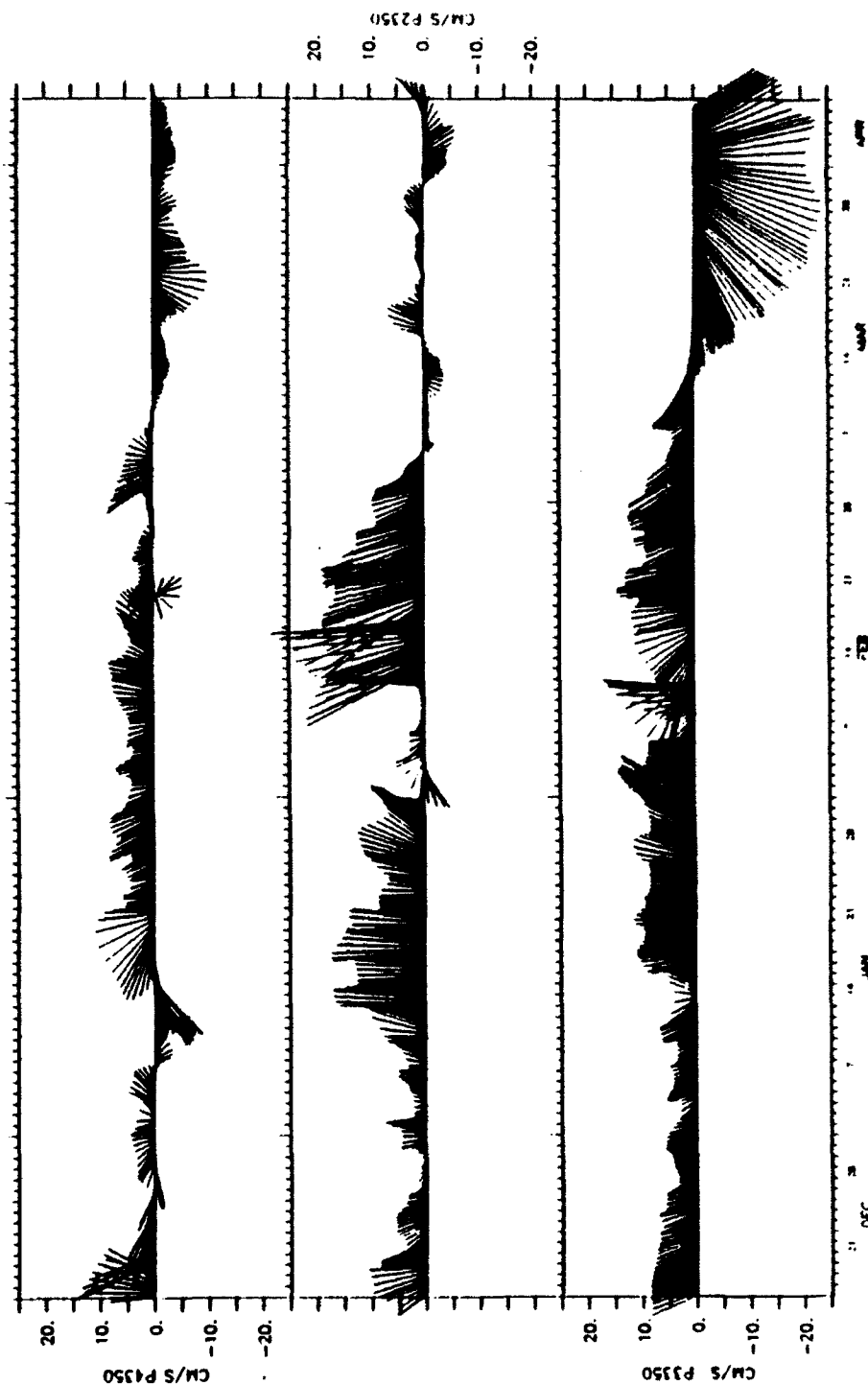| Mooring	Meter depth (m)	Mean (cm/s)	Maximum (cm/s)	Minimum (cm/s)	Standard Deviation (cm/s)	Mode 1 Eigenfunction (Eigenvalue = 172.0 (cm/s)2 for 66.9% of total variance)	Mode 2 Eigenfunction (Eigenvalue = 47.8 (cm/s)2 for 18.6% of total variance)
P4	350	1.5	14.4	-10.3	4.9	0.22	0.22
P4	500	1.3	10.7	-7.8	4.0	0.19	0.03
P2	350	6.8	28.4	-5.9	7.3	0.42	-0.66
P2	500	3.9	26.0	-6.7	5.6	0.29	-0.53
P3	350	4.3	16.8	-24.4	9.0	0.64	0.41
P3	500	3.4	11.5	-17.8	6.8	0.49	0.23
MB1	500	1.2	8.8	-7.2	2.5	0.04	0.11

Table 4b. **TIME DOMAIN STATISTICS FOR SEGMENT 1**
(ACROSS-SHORE COMPONENT)

Mooring	Meter depth (m)	Mean (cm/s)	Maximum (cm/s)	Minimum (cm/s)	Standard Deviation (cm/s)	Mode 1 Eigenfunction (Eigenvalue = 45.22 (cm/s)2 for 52.8% of total variance)	Mode 2 Eigenfunction (Eigenvalue = 17.51 (cm/s)2 for 20.4% of total variance)
P4	350	-1.0	5.9	-11.5	3.8	0.19	-0.64
P4	500	-0.7	3.3	-10.7	2.5	0.17	-0.37
P2	350	-0.7	7.4	-13.7	3.4	-0.12	0.50
P2	500	0.5	7.9	-8.1	2.7	-0.12	0.33
P3	350	-3.4	9.1	-16.5	5.4	-0.78	-0.25
P3	500	-2.6	5.2	-11.6	3.8	-0.54	-0.16
MB1	500	1.1	5.2	-2.0	1.4	0.03	-0.03

At P2, the mean alongshore current at 350 m for the entire segment was 6.8 cm sec^{-1} with a maximum of 28.4 cm sec^{-1} and minimum of -5.9 cm sec^{-1}. The 500 m instrument exhibited a similar mean (3.9 cm sec^{-1}) with a maximum of 26 cm sec^{-1}

33

cm sec^{-1} and minimum of -6.7 cm sec^{-1} (Table 4a). The across-shore component mean was offshore (-0.7 cm sec^{-1}) at 350 m with a maximum offshore velocity of -13.7 cm sec^{-1} and a maximum onshore velocity of 7.4 cm sec^{-1}. At 500 m, the mean was onshore (0.5 cm sec^{-1}) (Table 4b). The small across-shore means are again due to the coordinate rotation, which statistically minimized the ACS component.

P2 exhibited much stronger poleward flow than P4 from the beginning of the segment until 01 February. On this date, the poleward current abruptly diminished, then shifted to equatorward for 1 day at 350 m and 10 days at 500 m (Figures 5 and 6). As suddenly as the current changed, it shifted back to poleward and reached the segment's maximum of 28 cm sec^{-1} at 350 m on 16 February. This short relaxation was not observed at the other moorings. The current remained poleward until 05 March when the current at both instrument depths oscillated with a period of about 10 days for the final month of the time segment. The records from 350 and 500 m looked vertically coherent the entire time.

The most consistent poleward flow occurred at P3. With a mean alongshore current of about 4.3 cm sec^{-1} at 350 m and 3.4 cm sec^{-1} at 500 m, the flow remained steadily poleward and offshore (across-shore component mean -3.4 and -2.6 for 350 m and 500 m respectively) from the beginning of the segment until 17 March (Tables 4a and 4b). On 10 February, the 350 m current reached a maximum of 17 cm sec^{-1}.

34

This occurred about one week prior to the maximum at P2. From 10 February until 17 March, the flow at P3 rapidly shifted to equatorward at both depths. Additional data (not shown) show that this event exceeded 1000 m depth. During this event, current vectors rotated counterclockwise so that the flow was directed offshore until 01 April at which time the current shifted to onshore until the end of the segment (Figures 5 and 6). The maximum equatorward flow exceeded 24 cm sec^{-1} at 350 m and 17 cm sec^{-1} at 500 m.

With a mean alongshore current of 1.2 cm sec^{-1}, the flow at MB1 500 m demonstrated significantly different characteristics throughout the time segment (Table 4a). The poleward currents reached a maximum of 9 cm sec^{-1} on 03 March and a maximum equatorward flow of -7 cm sec^{-1} on 20 March. Weak ($\approx$ 5 cm sec^{-1}) equatorward bursts appeared with a period of about 12 days. Mooring MB1 did not display the dominant poleward current observed at the other moorings (Figure 6). MB1's location near the axis of the Monterey Canyon seemed to isolate the mooring from the general flow pattern offshore during this time segment.

The alongshore and across-shore velocity components were separately decomposed into empirical modes using the method outlined in Chapter III. Beginning with the alongshore component, the first two modes accounted for 85.5% of the total variance. The first mode alongshore eigenfunction
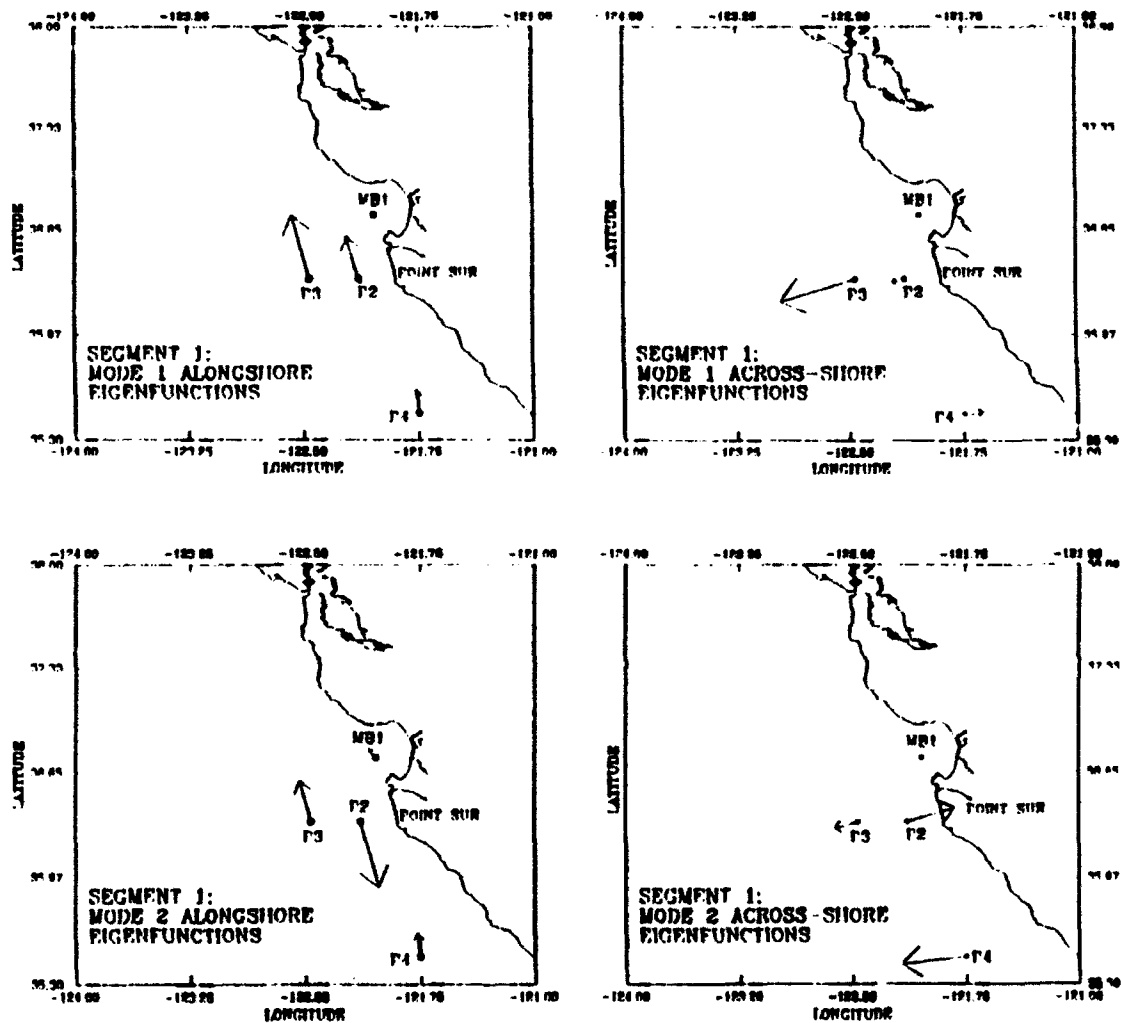
Figure 7. **Eigenfunction Amplitudes for Velocity Modes 1 and 2 During Time Segment 1:** ALS (left) and ACS (right) eigenfunctions are shown with vectors proportionally scaled for visual effect.

36

showed all moorings with the same sign (Figure 7, top left).
This represented the strong poleward current seen at moorings
P2, P3 and P4. The second mode alongshore eigenfunction
indicated an opposing structure between P2 and P3 with P4
again resembling the flow at P3 (Figure 7, bottom left).
This perhaps represents two dynamical regimes (discussed
later); an inshore or upper slope regime (including mooring
P2) and an offshore or lower slope regime (including moorings
P3 and P4). Mooring MB1 made only a small contribution to
these modes, due to its small amplitude and lack of
correlation with the other moorings.

For the across-shore component, the first two modes
accounted for 72.4% of the total variance (Table 4b). The
first mode eigenfunction indicated *opposing* flow between Pt.
Sur moorings (P2 and P3) and the Pt. Piedras Blancas mooring
(Figure 7, top right). The second mode eigenfunction however,
revealed an opposing structure between P2 and P3 with P4
resembling the flow at P3 (Figure 7, bottom right). This
again supported the idea that P3 and P4, both located over the
outer slope were contained within a somehow different
dynamical regime than P2 and MB1.

Alongshore modal amplitude and component velocity time
series were correlated to determine which mooring dominated
the different eigenmodes (Table 5). The correlation
coefficients showed a very high correlation between P3 and
mode 1 (.94/.95 at 350 m / 500 m). The P3 component velocity

37

time series and mode 1 amplitude were plotted and showed

strong similarities (Figure 8). This indicated that the

Table 5. SEGMENT 1 CORRELATION COEFFICIENTS FOR FIRST
AND SECOND MODE EIGENFUNCTIONS WITH TIME SERIES

	Across-shore		Alongshore	
	Mode 1	Mode 2	Mode 1	Mode 2
P4 350 m	0.33	0.71	0.59	0.32
P4 500 m	0.46	0.62	0.61	0.05
P2 350 m	0.24	0.61	0.76	0.62
P2 500 m	0.28	0.50	0.69	0.66
P3 350 m	0.98	0.19	0.94	0.32
P3 500 m	0.96	0.18	0.95	0.24
MB1 500 m	0.14	0.09	0.23	0.30

current at P3 contributed the most to the mode 1 variance.

Further, mode 2 showed the highest correlation at P2 (not

shown) suggesting that P2 contributed most to the mode 2

variance.

The across-shore modal amplitude time series were also

computed and correlated with each of the across-shore

component velocity time series (Table 5). Consistent with

the relative magnitudes presented in Figure 7, the first mode

amplitudes were highly correlated with the P3 time series at

both 350 m and 500 m (.98 and .96 respectively). The P3 350

m across-shore component time series was plotted with the mode

1 amplitude time series clearly showing the current's

influence on the mode 1 amplitudes (Figure 8). For mode 2,

P4 showed the highest correlation (.71 and .62 for 350 m and

Segment 1: P3 500 vs Mode 1 Amplitude (Alongshore Components)

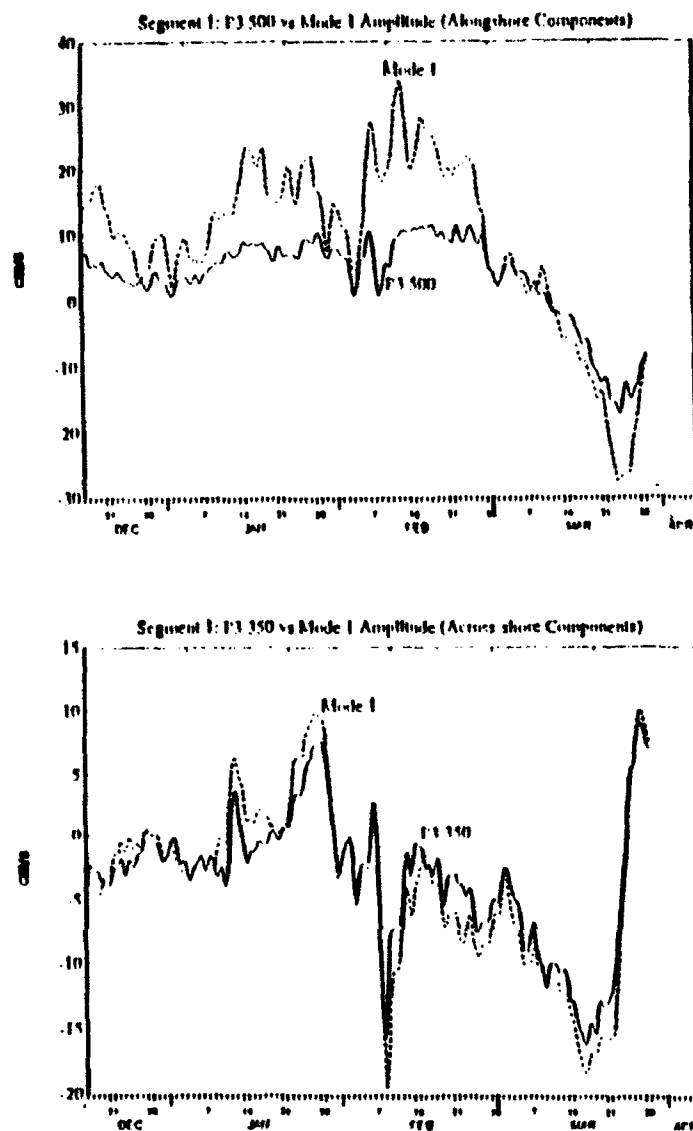Segment 1: P3 350 vs Mode 1 Amplitude (Across shore Components)

Figure 8.   A Comparison of the Mode 1 Velocity Amplitudes
with the Best Correlated Individual Time Series
for Segment 1: The top panel shows the
alongshore components and the bottom panel shows
the across-shore components.

500 m, respectively) with flow at P2 opposing that at P4 and

slightly less correlated. As expected, the flow at MB1

contributed very little to the overall structure in the first two modes with correlation coefficients close to zero (Table 5).

To summarize, time domain analysis described a current structure characterized by primarily poleward alongshore flow with a small offshore component at P2 and P3 and a small onshore component at P4. A secondary influence caused opposing flow between P2 and P3 with P4 generally following the P3 pattern. An interesting result showed that although P2 had a larger mean signature, P3 currents dominated the first empirical mode. The significance lies in the EOF analysis method where contributions from all moorings were considered to produce an overall spatial structure and will be discussed in greater detail later. Finally, results from MB1 suggested that this mooring was secluded from the offshore flow during this time segment.

2. Frequency Domain Analysis

Variance conserving spectra were plotted to determine the frequencies of maximum energy (Figures 9a through 9d). Since the currents were initially rotated in a manner that maximized alongshore variance, the alongshore component spectra generally showed the highest energy levels and are discussed first. Reported energy levels reflect the normalized values to be consistent with the plots.

Figure 9a. Segment 1 Variance Conserving Auto-Spectra for 350 m: Alongshore and across-shore component spectra are shown for P4 (top) and P2 (bottom).

41

Figure 9b. **Segment 1 Variance Conserving Auto-Spectra for 350 m:** Alongshore and across-shore components are shown for mooring P3 350 m.

42

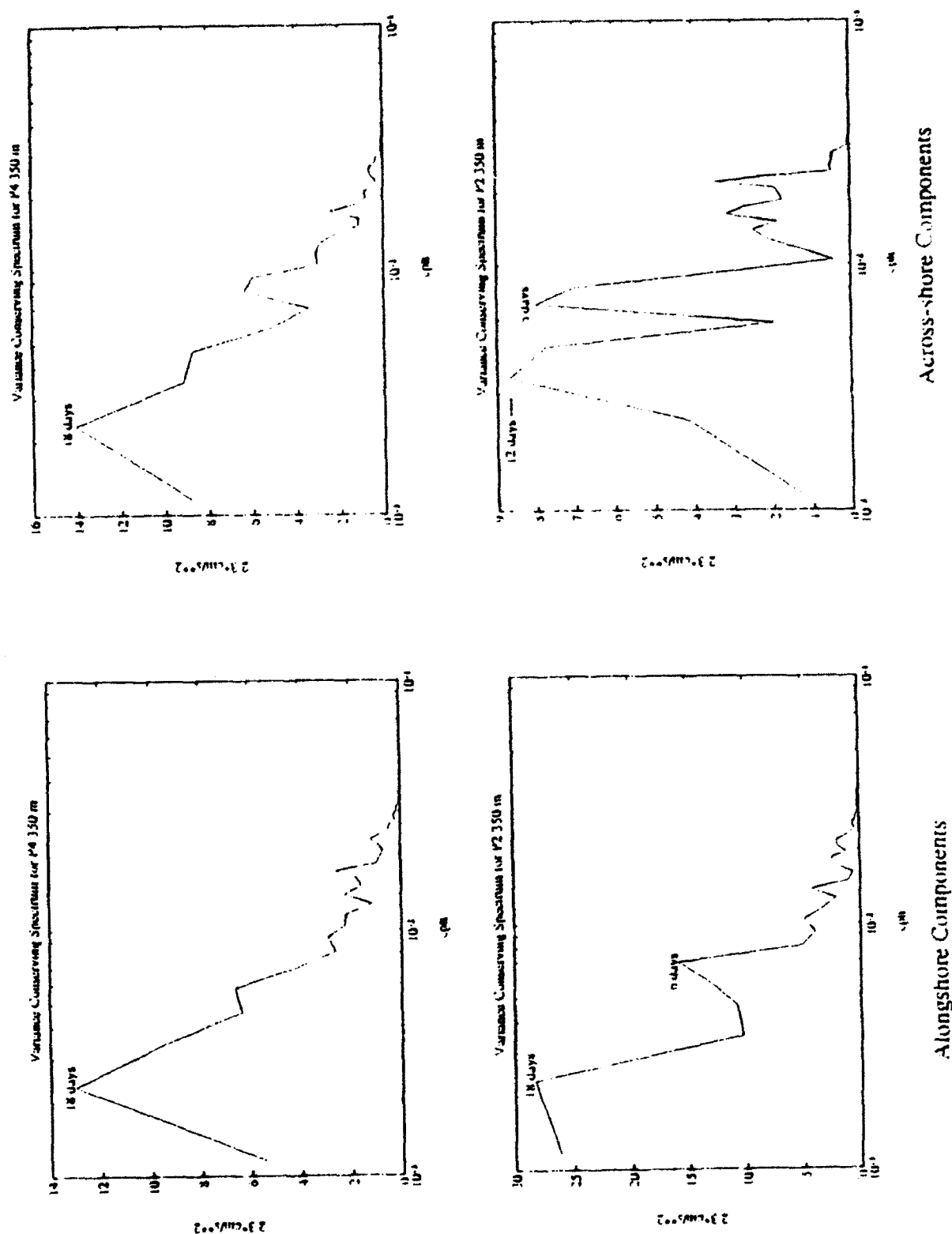**Figure 9c.** **Segment 1 Variance Conserving Auto-Spectra for 500 m:** Alongshore and across-shore component spectra are shown for P4 (top) and P2 (bottom).

43

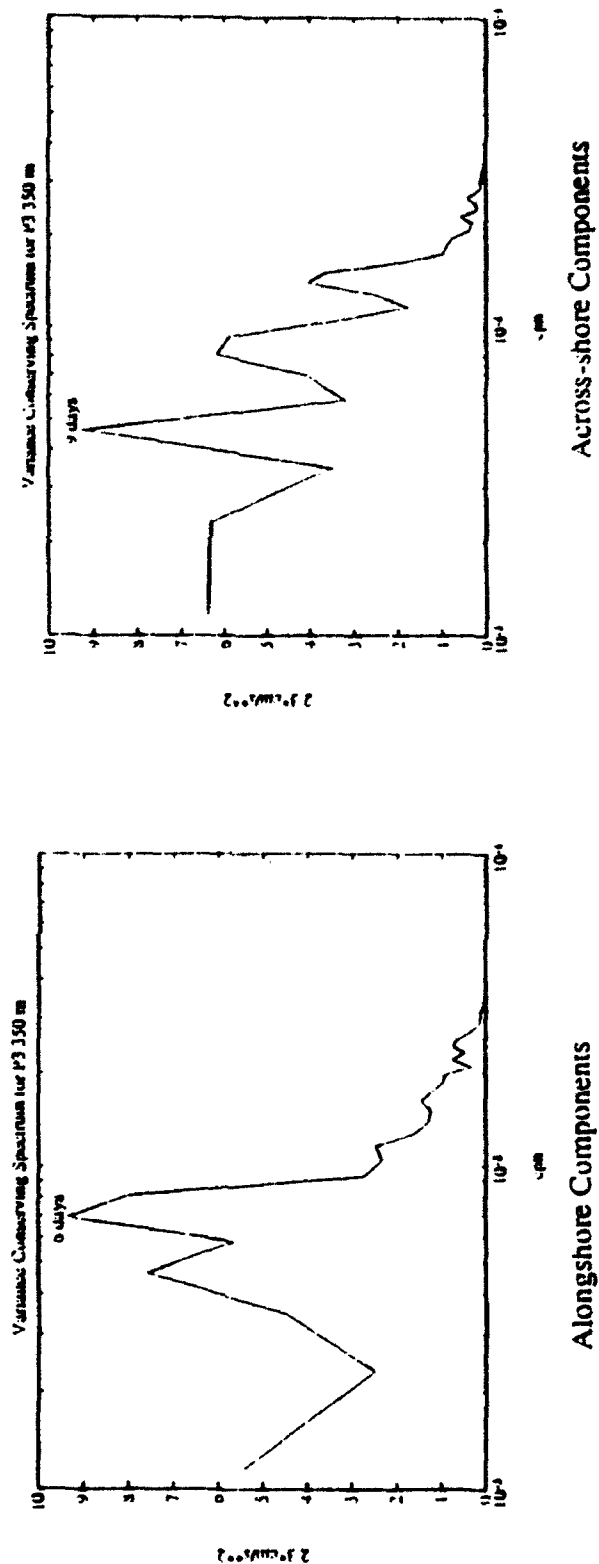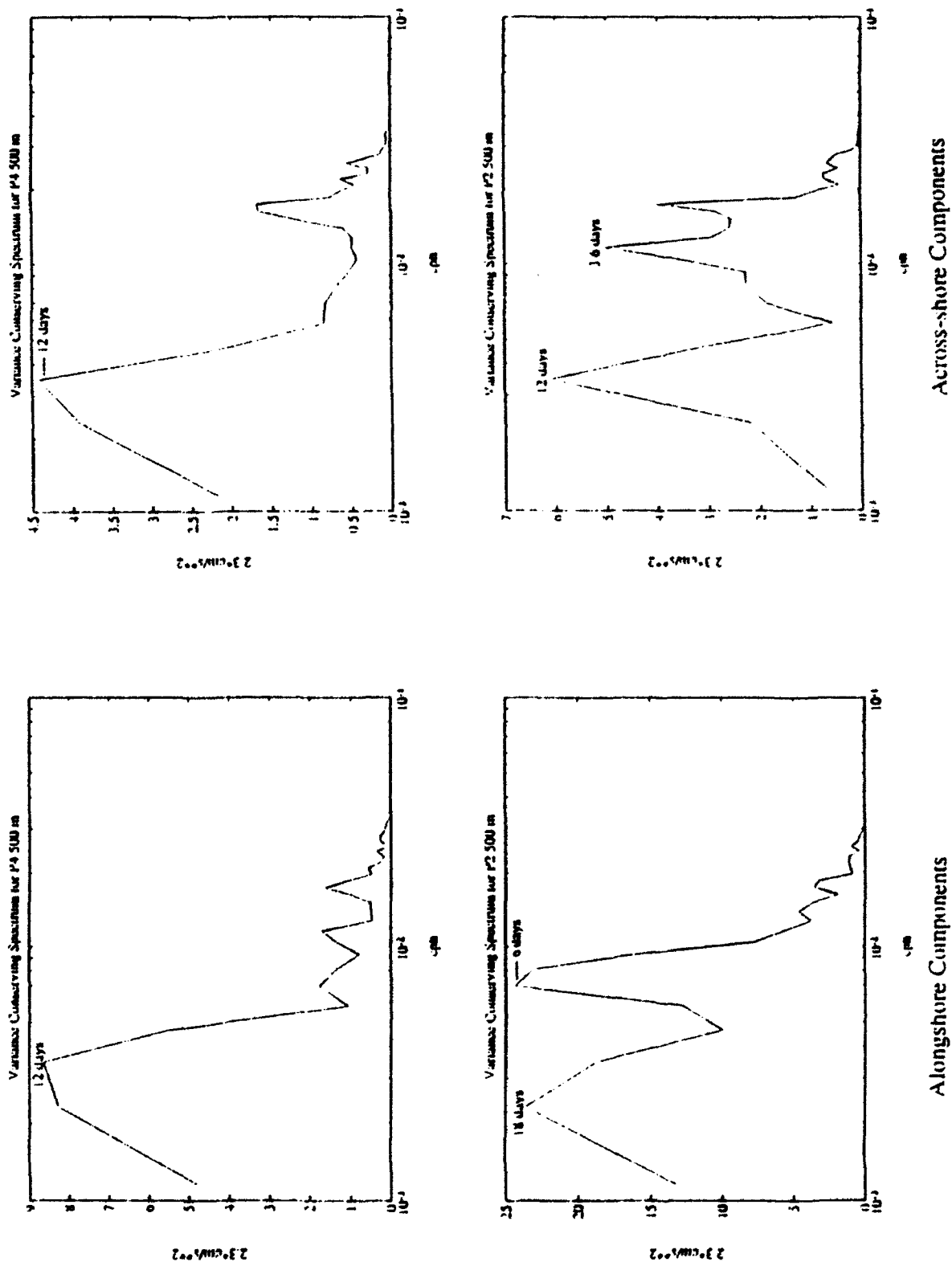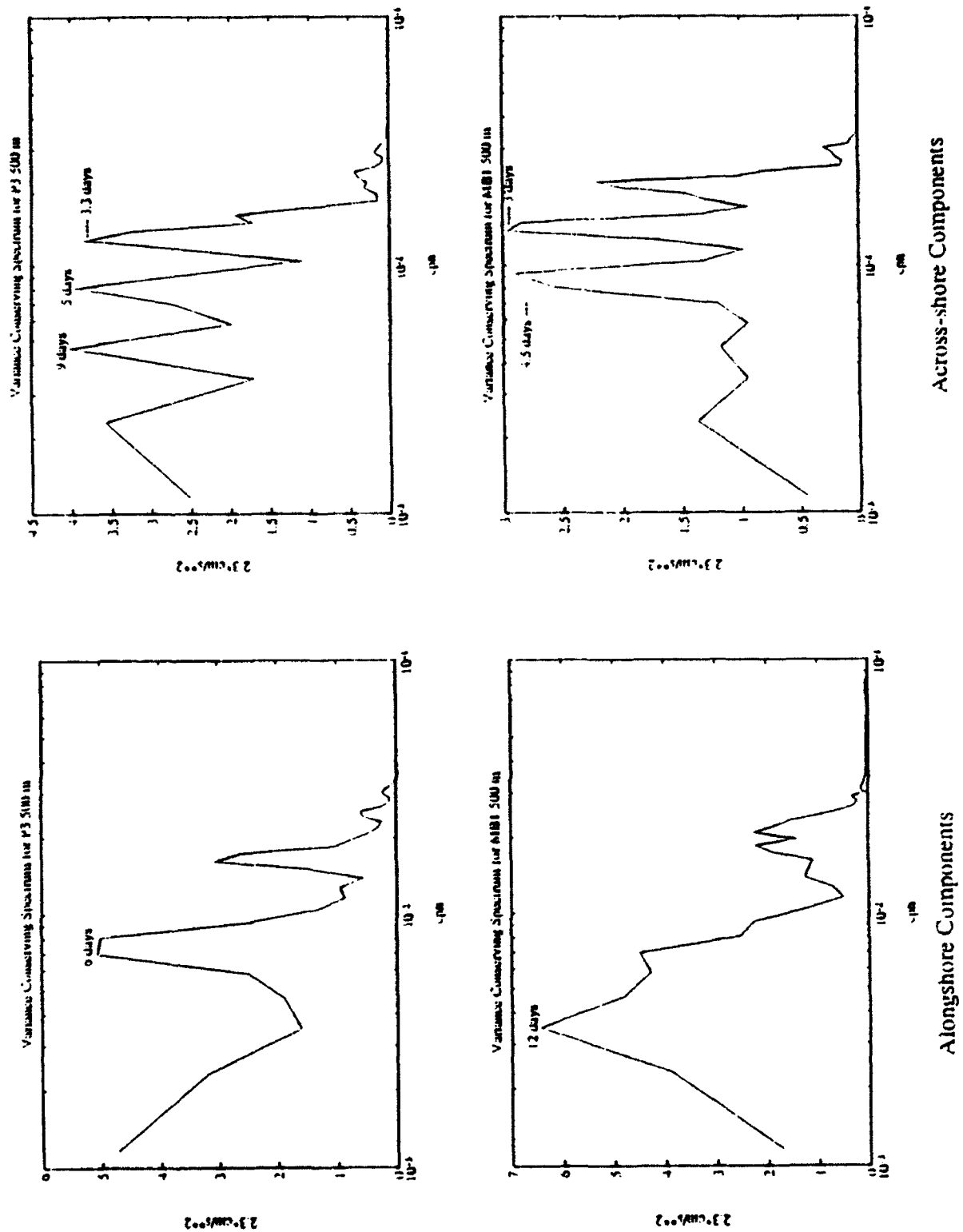**Figure 9d.** **Segment 1 Variance Conserving Auto-Spectra (500 m):** Alongshore and across-shore component spectra are shown for P3 (top) and MB1 (bottom).

44

At P4, the 350 m current spectrum showed an energy peak of 13.0 cm^2 sec^{-2} at 18 days (Figure 9a, top left). At 500 m, the energy decreased and shifted towards shorter periods, peaking at 8.6 cm^2 sec^{-2} with a period of 12 days (Figure 9c, top left). For P2, the maximum alongshore component energy level at 350 m was 28.3 cm^2 sec^{-2} and occurred at a period of 18 days . A secondary signal of 15.8 cm^2 sec^{-2} appeared at a period of 6 days (Figure 9a, bottom left). Similar peaks occurred at 500 m except the energy level at 6 days (24.4 cm^2 sec^{-2}) actually exceeded the 18 day signal of 23.6 cm^2 sec^{-2} (Figure 9c, bottom left). At P3 350 m, the energy level decreased from that at P2 to a peak level of 9.4 cm^2 sec^{-2} at a period of 6 days (Figure 9b, left). The 500 m spectrum here also exhibited a maximum energy level at a 6 day period but decreased to 5.0 cm^2 sec^{-2} (Figure 9d, top left). The MB1 alongshore spectrum (Figure 9d, bottom left) displayed a maximum energy level of 6.4 cm^2 sec^{-2} at a period of 12 days.

The across-shore component spectra exhibited energy peaks at periods similar to the alongshore components. The P4 350 m spectrum peaked at 18 days with an energy level of 14.1 cm^2 sec^{-2} (Figure 9a, top right). The energy maximum decreased to 4.4 cm^2 sec^{-2} at 500 m and occurred at 12 days (Figure 9c,top right). At mooring P2, the 350 m spectrum showed two peaks again at 12 days and 6 days. The first had an energy level of 8.7 cm^2 sec^{-2} while the second was slightly

45

less energetic at 8.0 cm^2 sec^{-2} (Figure 9a, bottom right). At 500 m, the energy also peaked at 12 days but decreased to 6.1 cm^2 sec^{-2}. A smaller 3.6 day peak occurred with an energy level of 5.0 cm^2 sec^{-2}. At P3, the 350 m spectrum peaked at 9 days with an energy level of 9.2 cm^2 sec^{-2} (Figure 9b, right). At 500 m, three distinct peaks at 9, 5, and 3.3 days occurred with energy levels close to 4.0 cm^2 sec^{-2} at all periods (Figure 9d, top right). The spectrum at MB1 displayed peaks at 4.5 and 3 days with energy levels around 2.9 cm^2 sec^{-2} (Figure 9d, bottom right). In general, the across-shore component spectra at moorings P4 and P3 displayed energy levels comparable to those for the alongshore components while P2 and MB1 exhibited higher energy level in the alongshore component again suggesting two distinct dynamical regimes.

In short, the alongshore component energy levels decreased with depth at moorings P4, P2 and P3 with the greatest energy at P2. The energy level at MB1 was comparable to the 500 m spectra at both P4 and P3.

Cross-spectra between moorings showed relatively few coherent signals. For the alongshore components (Figures 10a and 10b) P2 and P3 were coherent at periods of around 5-6 days. The signal at P3 led that at P2 by about 40° at 350 m and 16° at 500 m. The analysis also showed a coherent 4.5 - 6 day signal between P4 and P2 at 500 m and a 6 day signal between P4 and P2 also at 500 m. P4 led P2 by 26°, 35° and

46° for signals of 6 days, 5.1 days and 4.5 days respectively. P4 led P3 by 13° for the 6 day signal there. The significance of this 6 day fluctuation is not clear since it represented such a small fraction of the energy at P4. This may be a spurious coherence resulting from the strong 6 day peak at mooring P2. No significant coherence was observed at the dominant periods.

The only across-shore coherent signals were observed between P2 and P3 at both 350 m and 500 m. The 350 m data (not shown) exhibited coherence at 12 days, 5 days, and 3 days. At the 12 day and 3 day signals, P2 led P3 by 5° and 18° respectively while P3 led P2 by 29° at the 5 day signal. Coherence values just barely reached the 95% significance level at this depth. Although the P2 energy reached a maximum at 12 days, the P3 energy at 12 days represented a much smaller fraction of the total variance; likewise for the 5 day and 3 day signals. Thus the importance of these coherent signals is not clear. At 500 m, coherence levels were somewhat more significant (Figure 10c). Specifically, two wider coherent bands (9-12 days and 4.5-5 days) were observed with an additional peak at 3.6 days. P2 led P3 by about 57° for the first band while P3 led P2 by 8° and 48° for the second band and by 100° for the 3.6 day signal. These signals corresponded with the maximum energy levels observed at P2 500 m (12 and 3.6 days) and those at P3 (9, 5 and 3.3 days).
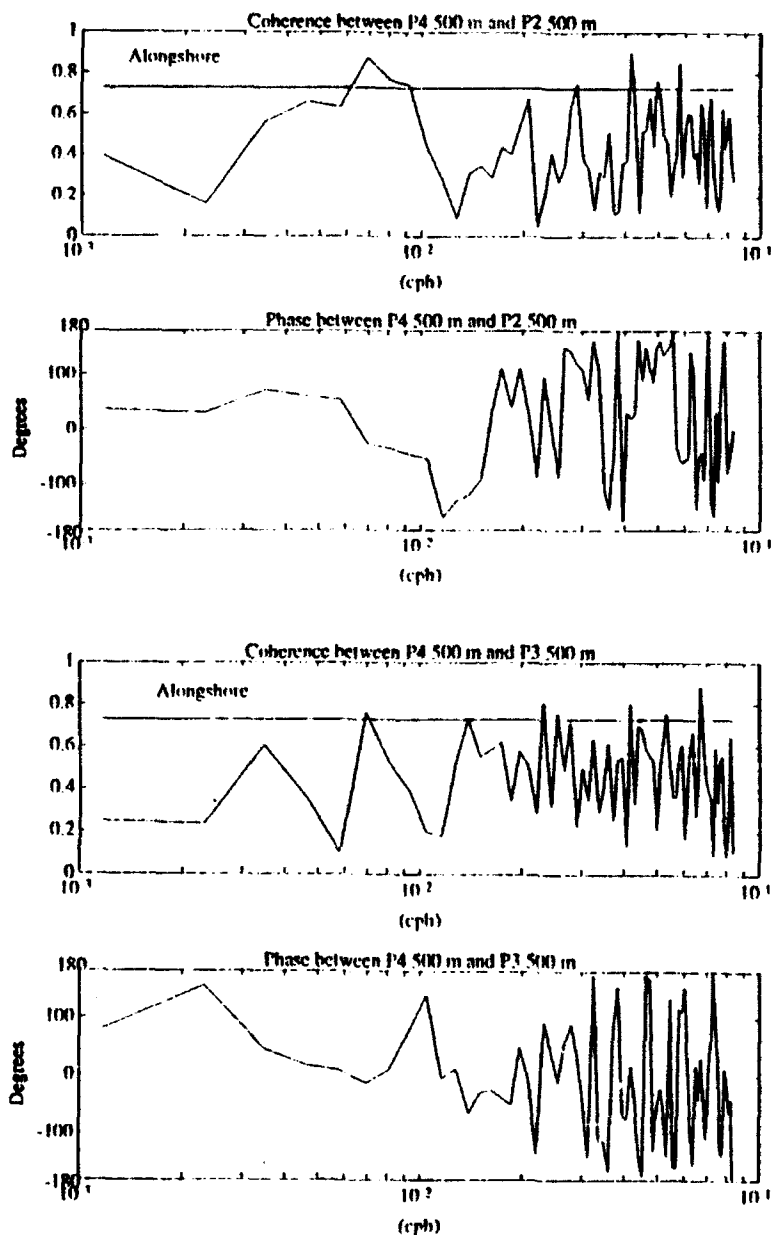
Figure 10a. **Segment 1 Coherence and Phase for Alongshore Current Components:** Coherence and phase are shown for P4 with P2 (top) and P4 with P3 (bottom). The solid line on the coherence plot indicates the 95% significance level. A negative phase means that the first series leads the second.

48
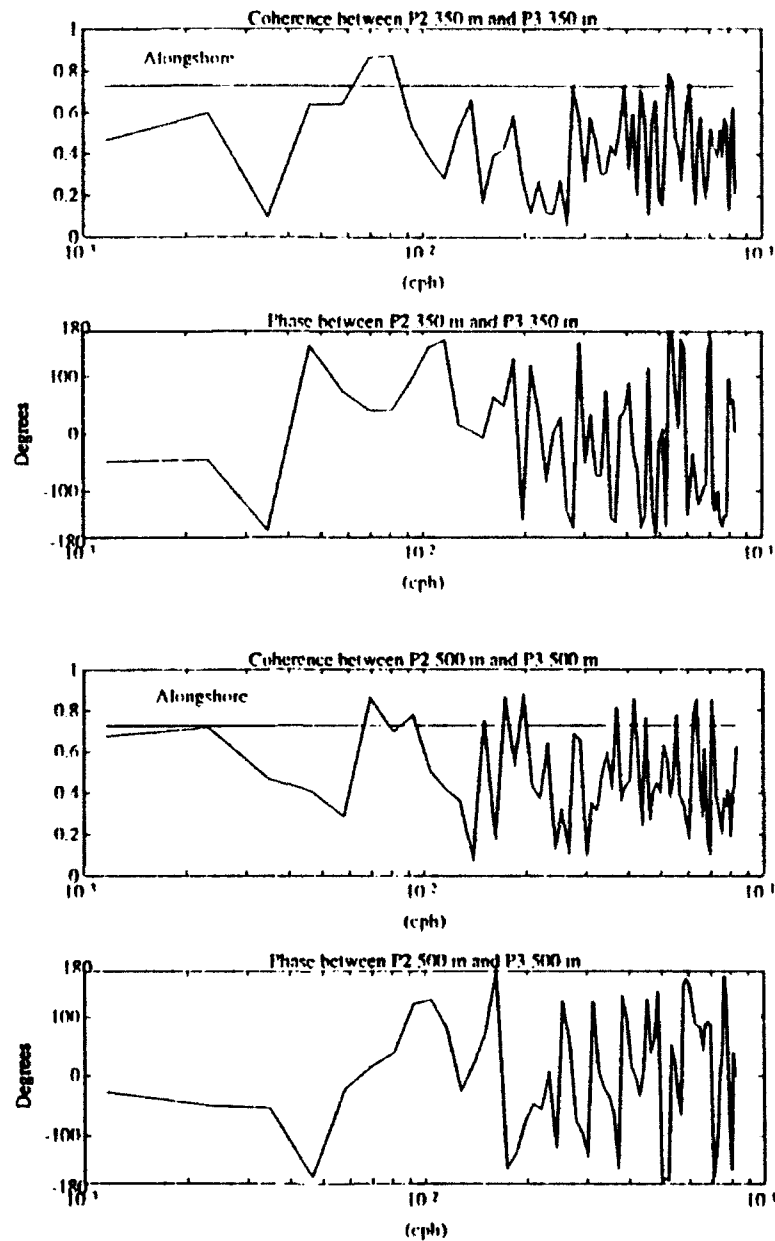
Figure 10b. **Segment 1 Coherence and Phase Between P2 and P3:** Coherence and phase are shown for 350 m (top) and 500 m (bottom). Other details are the same as in Figure 10b.
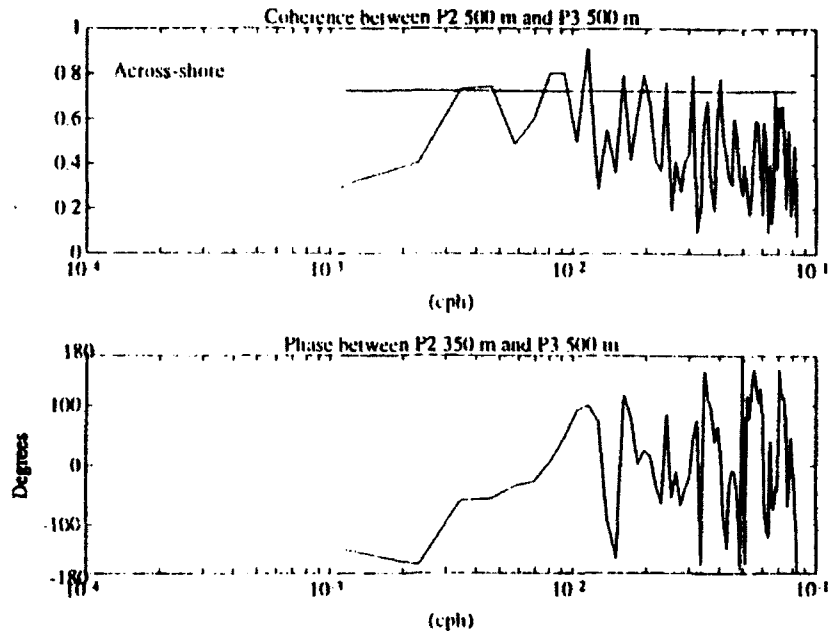
Figure 10c. Segment 1 Coherence and Phase for Across-shore Current Components: Details are as in Figure 10a except this figure shows the across-shore component coherence and phase between P2 500 m and P3 500 m only with three peaks from 9-12 days, 4.5-5 days and 3.6 days.

Therefore, it appeared that the lowest frequency across-shore component signal (periods between 9 and 12 days) propagated offshore from P2 to P3 while the higher frequencies (periods less than 5 days) moved onshore from P3 to P2 for both alongshore and across-shore components.

B. SEGMENT 2

Segment 2 spanned a time from 30 August 1990 through 17 March 1991 (200 days) (Figure 2). Data were collected from the Pt. Sur and Monterey Bay moorings only (P2, P3, MB1, and MB2). MB2 was positioned about 30 km seaward of MB1 and its

position relative to the others is shown schematically in Figure 11. The Pt. Sur moorings provided data at 350 m, MB2 at 416 m and MB1 at 500 m. The vertical coherence at mooring P2 during other time segments indicated that the currents at P2 350 m can reasonably be compared to currents at MB2 416 m.
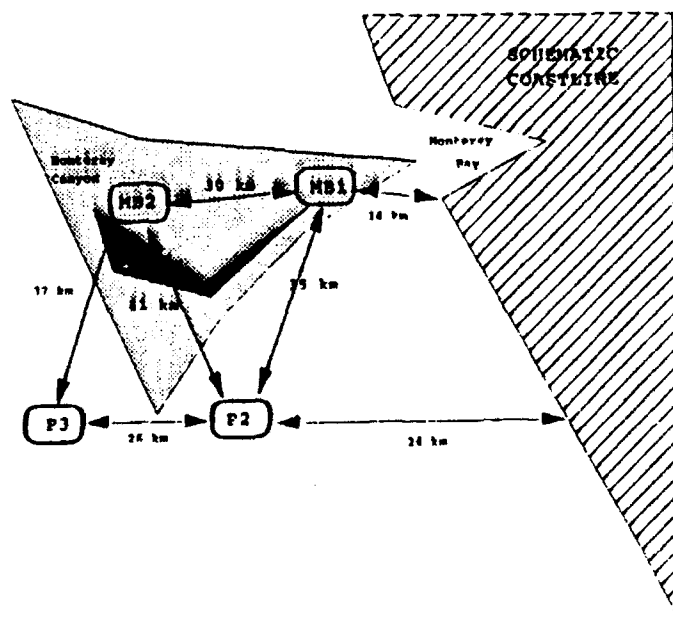
Figure 11.   **Schematic Mooring Locations for Segment 2:**
Distances between moorings are shown as in
Figure 4. Approximate location of the Monterey
Canyon is also illustrated. The canyon axis is
indicated by the darker shading.

1. Time Domain Analysis

In general, the mean flow during this time period was also directed poleward and offshore (Figure 12, Table 6). P2 had a mean alongshore flow of 5.6 cm sec^{-1} with a maximum of 23.8 cm sec^{-1} and a minimum of -10.1 cm sec^{-1} (Table 6a). The across-shore component (mean -0.4 cm sec^{-1}) was directed

51
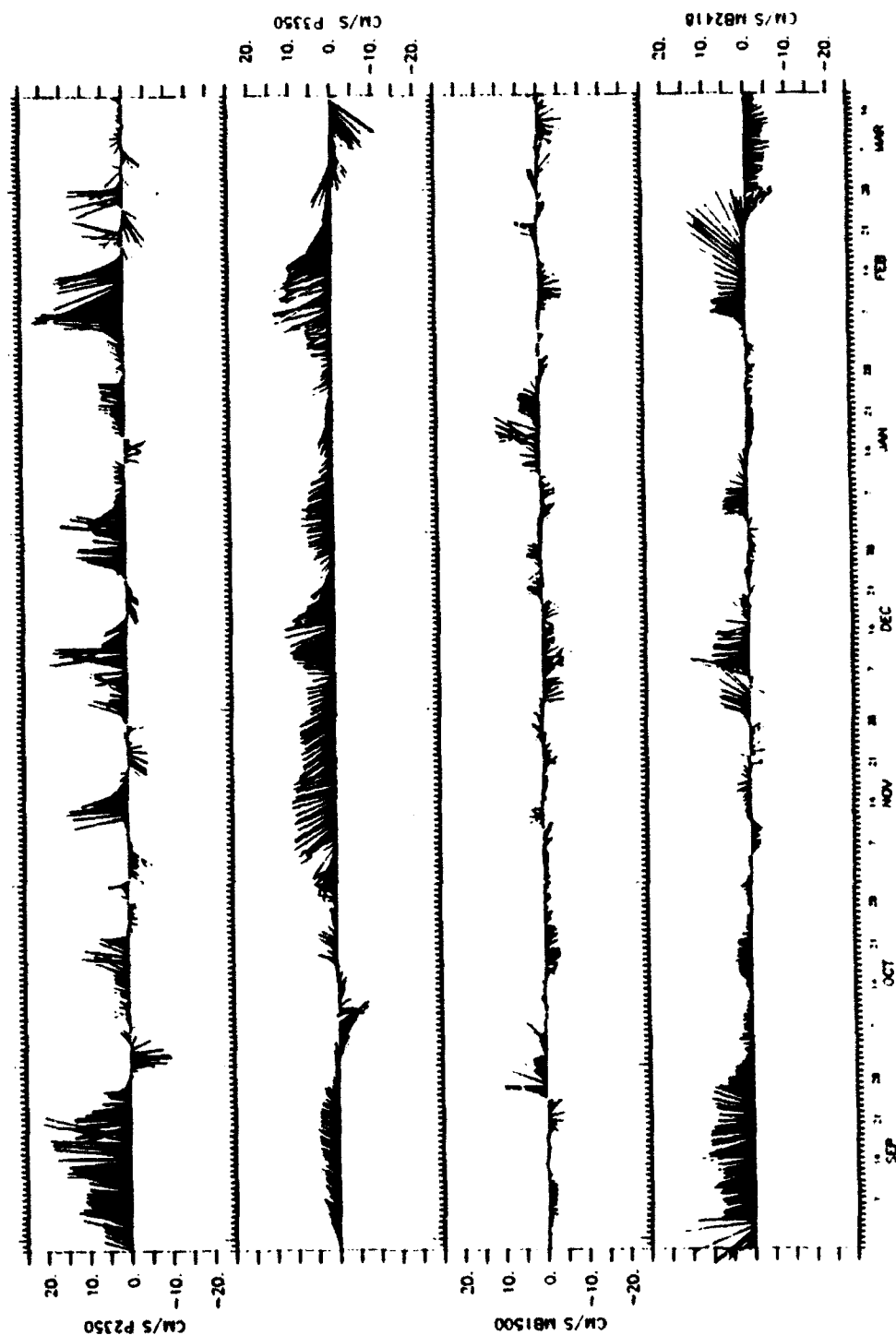
Figure 12. **Vector Velocities for Time Segment 2:** Velocity vectors are shown in cm sec^{-1} with poleward alongshore, as defined in the text, towards the top of the plot. Data are from P2 (top), P3 (second), MB1 (third), and MB2 (bottom).

Table 6a.   TIME DOMAIN STATISTICS FOR SEGMENT 2
(ALONGSHORE COMPONENT)

Mooring	Meter depth (m)	Mean (cm/s)	Maximum (cm/s)	Minimum (cm/s)	Standard Deviation (cm/s)	Mode 1 Eigenfunction (Eigenvalue = 63.22 (cm/s)² for 63.3 % of total variance)	Mode 2 Eigenfunction (Eigenvalue = 15.83 (cm/s)² for 15.8 % of total variance)
P2	350	5.6	23.8	-10.1	6.7	0.79	-0.26
P3	350	4.5	14.5	-12.0	4.6	0.33	0.93
MB1	500	-0.2	11.3	-7.4	3.1	-0.13	-0.10
MB2	416	2.6	17.7	-7.8	5.0	0.50	-0.24

offshore with a maximum offshore current of -7.9 cm sec^{-1} and a maximum onshore flow of 5.0 cm sec^{-1} (Table 6b). For the first month, steady poleward flow dominated (Figure 12). Around 28 September, a strongly periodic flow appeared with a period between 20 and 30 days. This signal was not clearly observed at P3, located about 25 km seaward of P2, but was observed at MB1 and MB2.

The flow at P3 was generally poleward and offshore with an alongshore component mean of 4.5 cm sec^{-1} with a maximum of 14.5 cm sec^{-1} and a minimum of -12.0 cm sec^{-1} (Table 6a). The across-shore component, with a mean of -2.2 cm sec^{-1}, was again directed offshore. The flow here had a strong offshore maximum of -17.5 cm sec^{-1} around 25 February with a maximum onshore current of 7.3 cm sec^{-1} (Table 6b). A weak ($\approx$ 7 cm sec^{-1}) equatorward shift appeared around 01 October and persisted for about 16 days thereafter (Figure 12). The current shifted back to poleward around 17 October

53

**Table 6b. TIME DOMAIN STATISTICS FOR SEGMENT 2
(ACROSS-SHORE COMPONENT)**

Mooring	Meter depth (m)	Mean (cm/s)	Maximum (cm/s)	Minimum (cm/s)	Standard Deviation (cm/s)	Mode 1 Eigenfunction (Eigenvalue = 22.88 (cm/s)2 for 64.5 % of total variance)	Mode 2 Eigenfunction (Eigenvalue = 5.99 (cm/s)² for 16.9% of total variance)
P2	350	-0.4	5.0	-7.9	2.4	-0.27	-0.12
P3	350	-2.2	7.3	-17.5	4.4	-0.88	0.43
MB1	500	1.2	6.2	-4.6	1.5	0.07	0.09
MB2	416	0.8	13.6	-9.9	2.9	0.38	0.89

and remained so until 07 March when another equatorward event
($\approx$ 12 cm sec^{-1}) dominated for the remainder of the segment.

At MB1, currents were directed equatorward and onshore
with a mean equatorward flow of 0.2 cm sec^{-1} and a larger
onshore mean of 1.2 cm sec^{-1} (Tables 6a and 6b). Although
weaker than the other moorings, the stick vector plot (Figure
12) also showed an oscillatory flow with a period of about 1
month with phase about opposite (180°) to the currents
observed at P2.

At MB2, alongshore flow was directed poleward with an
alongshore mean of 2.6 cm sec^{-1} , a maximum of 17.7 cm sec^{-1}
and a minimum of -7.8 cm sec^{-1} (Table 6a). The across-shore
flow (0.8 cm sec^{-1} mean) was slightly onshore exhibiting a
maximum of 13.6 cm sec^{-1} and a minimum of -9.9 cm sec^{-1}
(Table 6b). The flow here appeared steadily poleward from 30
August until 06 November. Beginning around 01 October the
currents appeared visually coherent with the equatorward

bursts described at P2, but were less energetic. The stick vector plots provided initial indications of a coastally trapped, poleward propagating disturbance between P2 and the Monterey Bay moorings that was less obvious as a modulation of the mainly poleward flow at the offshore mooring, P3.

EOF results during this time period were again consistent with the mean flow statistics. For the alongshore components, the first two modes explained 79.1% of the total variance. As in Segment 1, the mode 1 eigenfunction showed consistency at all moorings except MB1 (Figure 13, top left).

All first mode alongshore component eigenfunctions had the same sign. Together with the stick vector plots, this information indicated a tendency toward poleward flow at all moorings. The second mode showed a tendency for P2 and the Monterey Bay moorings to oppose the flow at P3 (Figure 13, bottom left). This could perhaps be attributed to the low frequency fluctuation which was present at P2 and MB2 but not at P3.

The first two across-shore modes, explaining 80.4% of the total variance (Table 6a), were used to describe the flow structure. The mode 1 across-shore eigenfunction described offshore flow at the Pt. Sur moorings with P3 supplying the largest amount of energy. To the north, an opposing flow could be seen at MB1 and MB2 (Figure 13, top right). The opposing mode 1 flow between Pt. Sur and MB2 is significant and is discussed in greater detail in association with

55
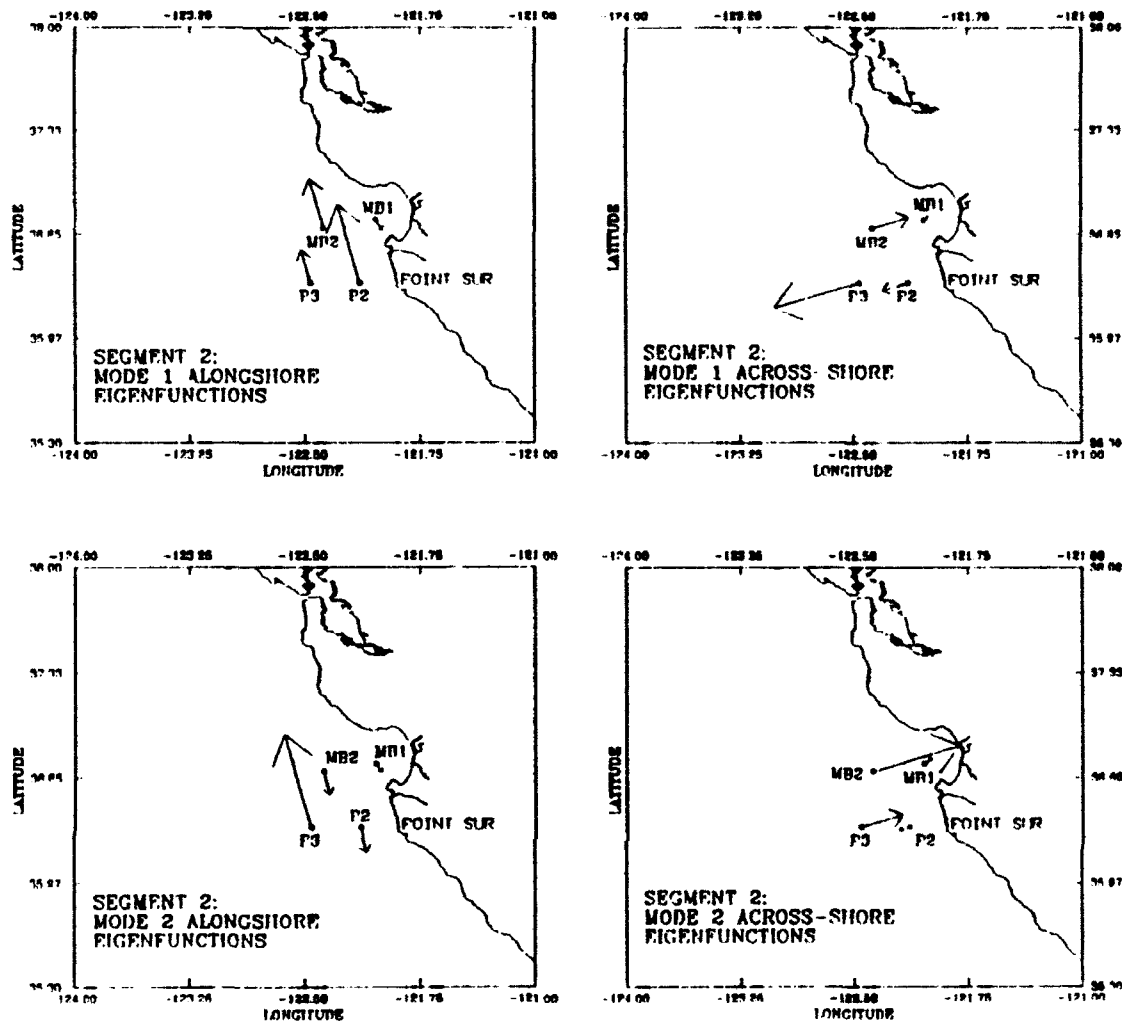
Figure 13. **Eigenfunction Amplitudes for Velocity Modes 1 and 2 During Time Segment 2:** Alongshore (left) and across-shore (right) eigenfunctions are shown with vectors proportionally scaled for visual effect.

Segment 3. Much like Segment 1, the mode 2 across-shore eigenfunction revealed an opposing structure between P2 and P3. MB2 followed the structure at P3 (Figure 13, bottom left) and appeared as an onshore flow also opposing P2. The flow at

MB1 contributed more to the total variance than it did during segment 1 but on the whole, it played a minor role in the overall current structure.

The mode 1 alongshore amplitude time series showed the highest correlation with the P2 alongshore velocity component time series (.94). Thus P2 most nearly resembled the mode 1 amplitude time series (Figure 14, top), showing P2 as the primary source for mode 1 variance. Mode 2 showed the highest correlation at P3 (.81) (Table 7).

Table 7. SEGMENT 2 CORRELATION COEFFICIENTS FOR FIRST AND SECOND MODE EIGENFUNCTIONS WITH TIME SERIES

	Across-shore		Alongshore	
	Mode 1	Mode 2	Mode 1	Mode 2
P2 350 m	0.53	0.12	0.96	0.15
P3 350 m	0.97	0.24	0.58	0.81
MB1 500 m	0.21	0.14	0.33	0.13
MB2 416 m	0.64	0.75	0.79	0.19

The across-shore modal amplitude and time series correlation showed P3 with the highest correlation (.97) for mode 1 while MB2 exhibited the highest correlation for mode 2 (.75) (Table 7). The P3 across-shore velocity components plotted with the mode 1 amplitudes showed this relationship very well (Figure 14, bottom). P2 and MB1 did not contribute significantly to the across-shore flow spatial structure.

In general, the primary current structure showed a poleward flowing current with a mean slightly smaller than that for Segment 1. The second mode alongshore eigenfunction

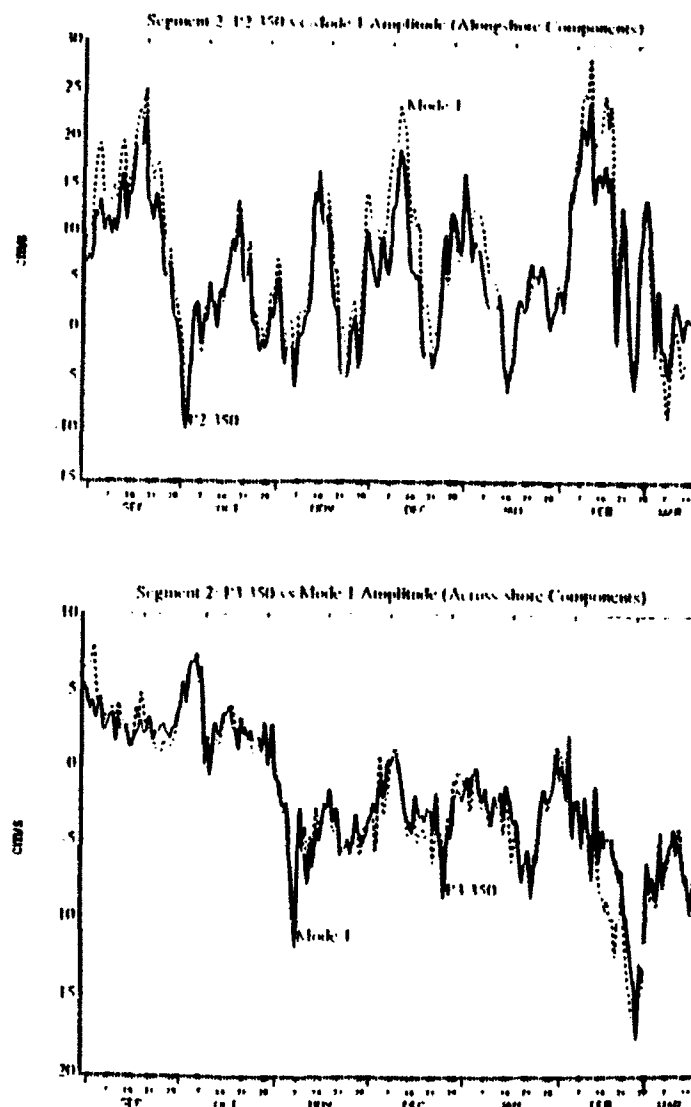**Figure 14.** A Comparison of the Mode 1 Velocity Amplitudes with the Best Correlated Individual Time Series: The top panel shows the P2 alongshore components and the bottom panel shows the across-shore components.

revealed consistent flow structures at P2, MB1 and MB2 that opposed the P3 structure. The equatorward bursts visible in the stick vector plots at these moorings could explain the second mode structure.

2. Frequency Domain Analysis

Variance conserving spectra were calculated for alongshore and across-shore velocity components. The alongshore component spectra showed energy peaks of 29.2 days at all moorings. The energy maximum at P2 (51.2 cm^2 sec^{-2}) greatly exceeded those at the other moorings (between 9 and 12 cm^2 sec^{-2}) (Figures 15a and 15b).

The across-shore component spectra showed significant peaks at 19.5 days for P2 and P3, 29.2 days for MB2 and 3.2 days for MB1. These peaks were all less than those described for the alongshore components (between 4 and 6 cm^2 sec^{-2}) (Figure 15b).

The alongshore components cross-spectra, showed coherent signals between several mooring pairs. These generally occurred at periods of 58.5, 29.2 and 19.5 days (Figures 16a and 16b). The phase varied with each period and between the mooring pairs. Phase diagrams for these three periods suggest complex phase relationships (Figure 17). Arrows indicate the direction of phase propagation, e.g. P2 leads MB2 by 37° at T = 29.2 days. No arrow indicates no significant coherence. A marginally significant arrow is sometimes shown as a dashed line if the phase was steady and consistent with the other pairs.
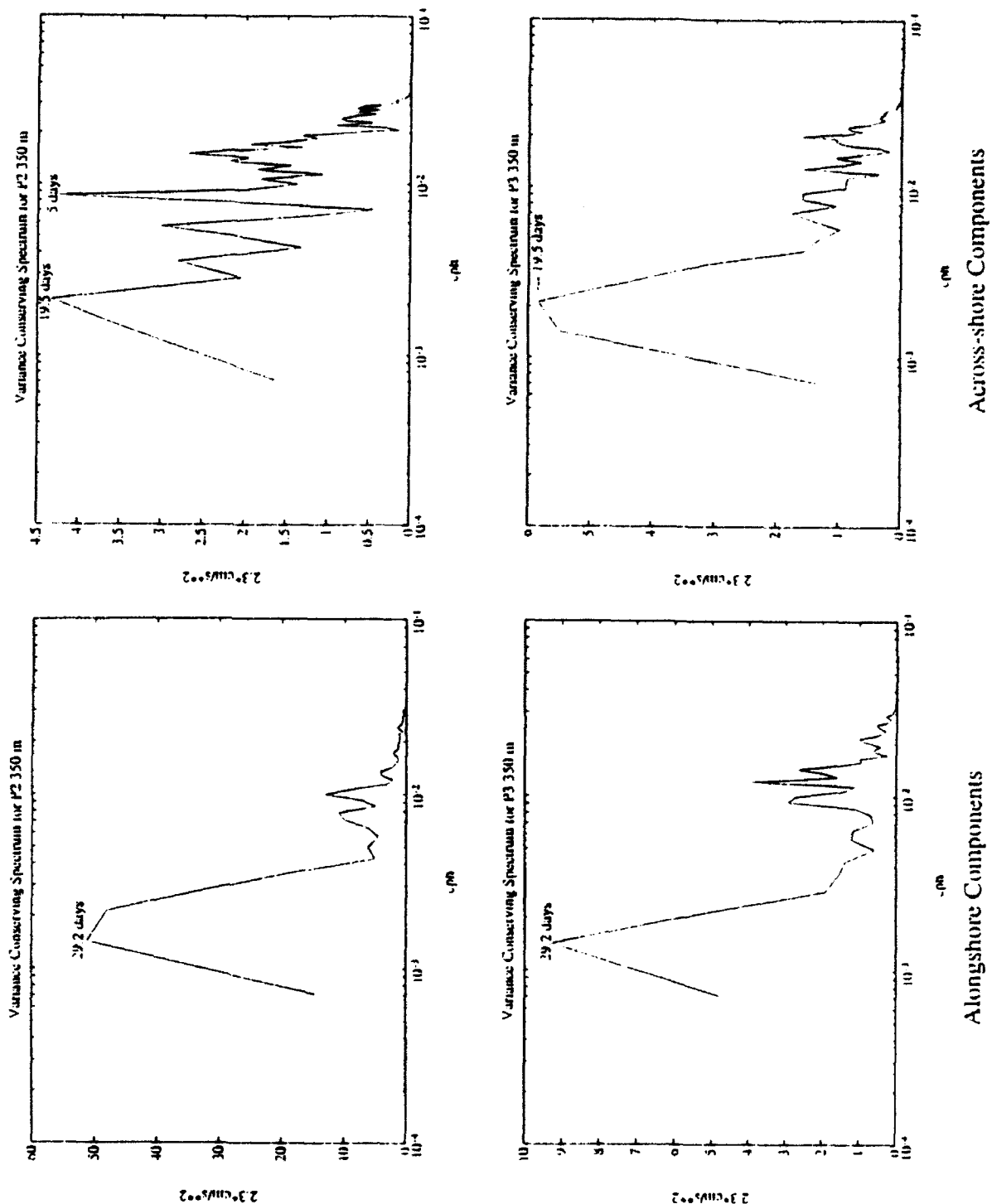
Figure 15a. **Segment 2 Variance Conserving Auto-Spectra for P2 (top) and P3 (bottom): ALS (left panels) and ACS (right panels) at 350 m are shown.**
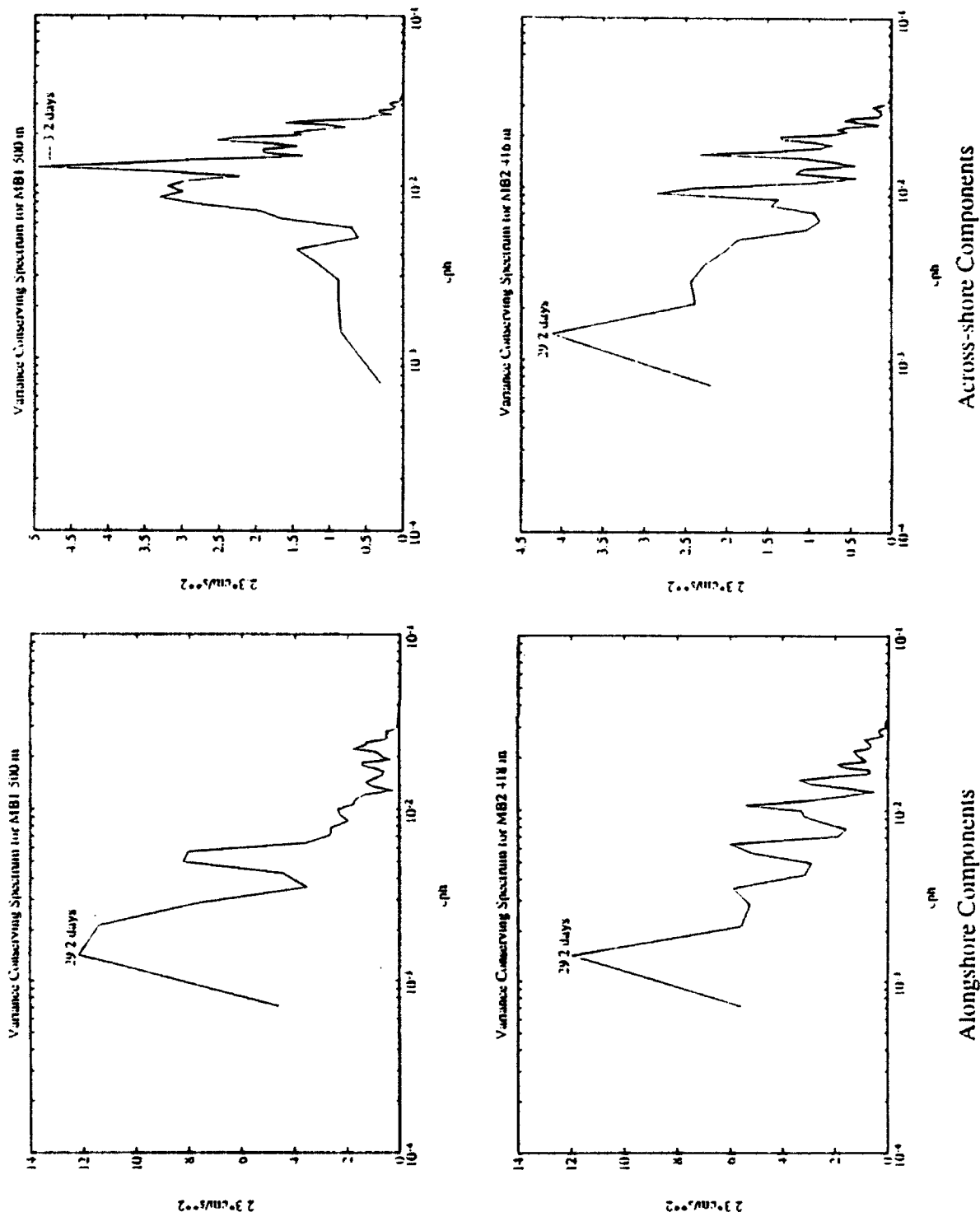
Figure 15b. **Segment 2 Variance Conserving Auto-Spectra for MB1 (top) and MB2 (bottom):** ALS (left panels) and ACS (right panels) are shown.

61
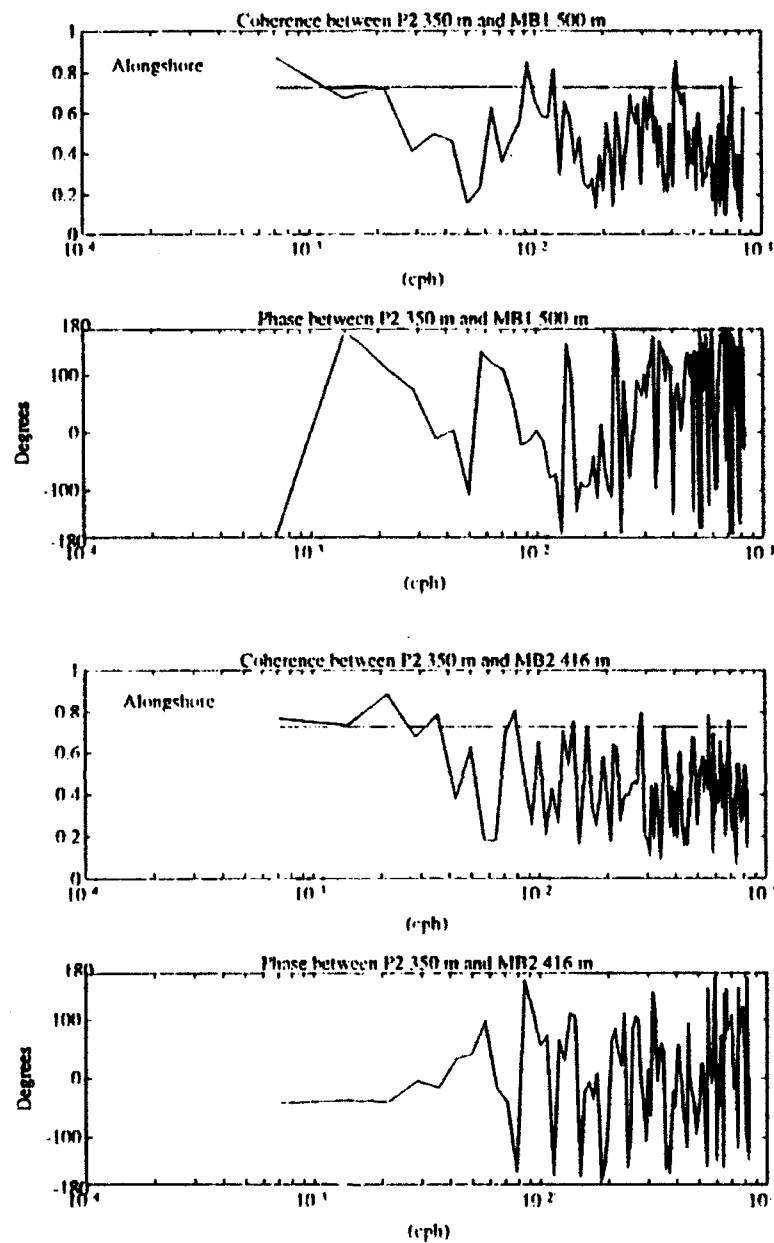
Figure 16a. **Segment 2 Coherence and Phase for Alongshore Current Components:** Plots are shown for P2 with MB1 (top) and P2 with MB2 (bottom). Other details are as in Figure 10a.

62
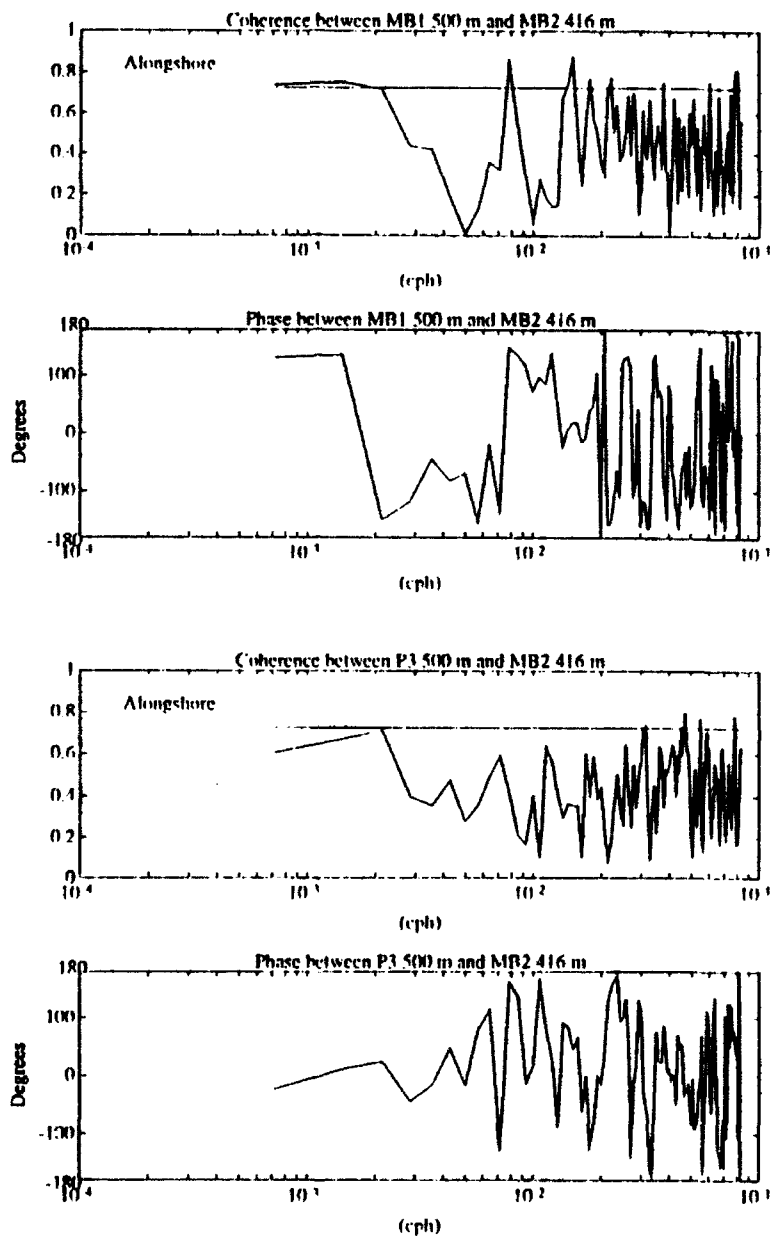
Figure 16b. **Segment 2 Coherence and Phase for Alongshore Current Components:** Plots are shown for MB1 with MB2 (top) and P3 with MB2. Other details are as in Figure 10a.

The 29.2 day signal (Figure 17, middle) represented the largest energy peak. At this period, P2 led P3 by 48° and MB2 by 38° consistent with a poleward propagating disturbance. Another interesting observation could be made by inspecting the phase between P2, MB2 and MB1. P2 led MB2 by around 40° and MB2 led MB1 by about 135°. Also, consistent with the stick vector plots, MB1 appeared to be 180° out of phase with P2. Adding the phase from P2 to MB2 with that from MB2 to MB1, yields a result consistent with the phase between P2 and MB1 and adds confidence to the results.

The 19.5 day signal showed some characteristics that were consistent with the other two periods. Specifically, P2 led both MB2 and P3 by 42° and 23°, respectively. In contrast to the other signals, MB2 led P3 by 24° and MB1 led P2 by 170°. The energy at 19.5 days was less than that of 29.2 days but significantly higher than the 58.5 day signal.

For the 58.5 day signal, P2 led MB2 by 42°, MB1 by 170°, and MB2 by 23°. P3 was coherent with MB1 and led by 136° and MB2 led MB1 by 132°, much like the 29.2 day signal. In general, energy seemed to propagate in a poleward direction but the significance of this picture is probably small since the energy level at 58.5 days was the lowest of all coherent periods.

By knowing the phase and mooring separation distances, alongshore wavelengths between P2 and MB2 and across-shore wavelengths between P2 and P3 could be calculated. The

64
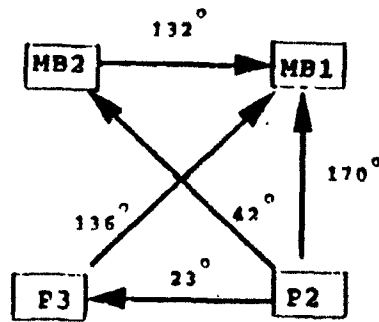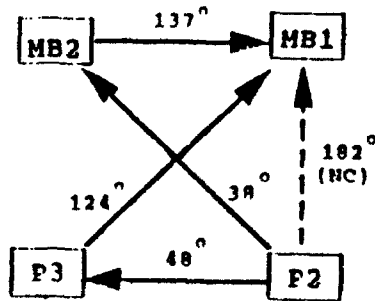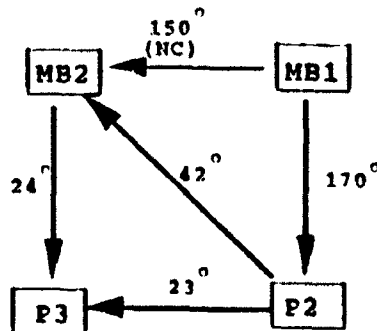
Figure 17. **Segment 2 Phase Diagram:** Arrows indicate the direction of phase propagation between moorings. The phase in degrees is shown for each period of significant coherence.

results for the most significant energy levels (29.2 and 19.5 days) are summarized in Table 8. The phase error of cross-spectral analysis are also presented here. It is important to note the phase errors since this could introduce a significant

source of error in the wavelength calculations, which will be compared to theory in Chapter V.

Table 8. **OBSERVED PHASE AND WAVELENGTHS FOR LOW FREQUENCY OSCILLATION (SEGMENT 2)**: A positive phase speed indicates that the first mooring leads the second.

	Mooring Pair	Phase (o)	Phase (days)	Phase error (o)	Phase speed (km/day)	Observed wavelength (km)	Separation Distance (km)
T = 29.2 days	P2 & MB2	38	3.1	49	+13	389.5 (ALS)	41
T = 29.2 days	P2 & P3	48	3.9	34	+7	192.1 (ACS)	26
T = 29.2 days	MB1 & MB2	137	11.1	46	-3	78.8 (ACS)	30
T = 19.5 days	P2 & MB2	42	2.3	26	+18	351.0 (ALS)	41
T = 19.5 days	P2 & P3	75	1.2	41	+6	122.3 (ACS)	26

Observed wavelengths were calculated by multiplying the separation distances by 360° and dividing by the phase difference. This procedure produced alongshore wavelengths of 390 km for the 29.2 day signal and 351 km for the 19.5 day signal. The across-shore wavelengths were 192 km and 122 km for the 29.2 and 19.5 day signals, respectively at Pt. Sur. Between the Monterey Bay moorings, an across-shore wavelength of 78.8 km was calculated for the 29.2 day signal but with a phase speed in the opposite direction from off Pt. Sur (Table 8). This procedure calculated the largest possible wavelength based on the phase differences. The phase speed was calculated by dividing the alongshore separation (41.1 km between P2 and MB2) and the across-shore separation (26 km

66

between P2 and P3, 30 km between MB1 and MB2) by the time lags.

Cross spectra calculations showed little coherence between the across-shore velocity components. The only significant coherence occurred between moorings P2 and MB2 at a period of 19.5 days (not shown). MB2 led P2 by about $175°$ so the two moorings were generally out of phase in the across-shore component. A similar situation existed in Segment 3, where a mesoscale meandering feature dominated the currents at these moorings.

C. SEGMENT 3

Segment 3 lasted from 26 May 1991 until 18 November 1991 (177 days) (Figure 2). In addition to the Pt. Sur and Monterey Bay moorings, this time segment included data from moorings D and E near the Farallon Islands. Mooring D was located about 110 km to the north of MB2 and mooring E was positioned 32 km to the north of D (Figure 18). Currents at P2 were obtained at depths of 350 m and 500 m but the other moorings only had data at 400 m. For purposes of EOF and spectral analyses, the currents at P2 were linearly interpolated to a depth of 400 m to approximately match the others (Figure 19).

1. Time Domain Analysis

Time domain statistics again showed a poleward alongshore component mean at all moorings. At P2, the mean
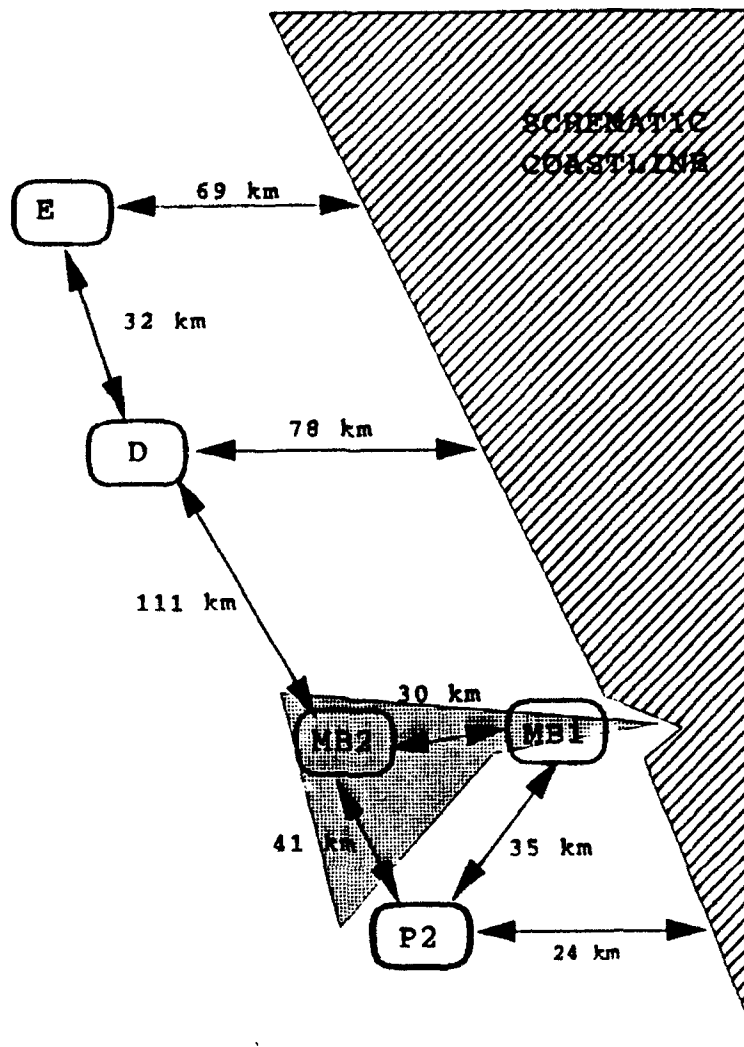
Figure 18. **Mooring Separation Distances for Segment 3:**
Details are as in Figure 4.

alongshore current was 6.3 cm sec^{-1} with a maximum of 33.3 cm

sec^{-1} and a minimum of -19.0 cm sec^{-1} (Table 9a). The

across-shore statistics (Table 9b) showed a mean offshore flow
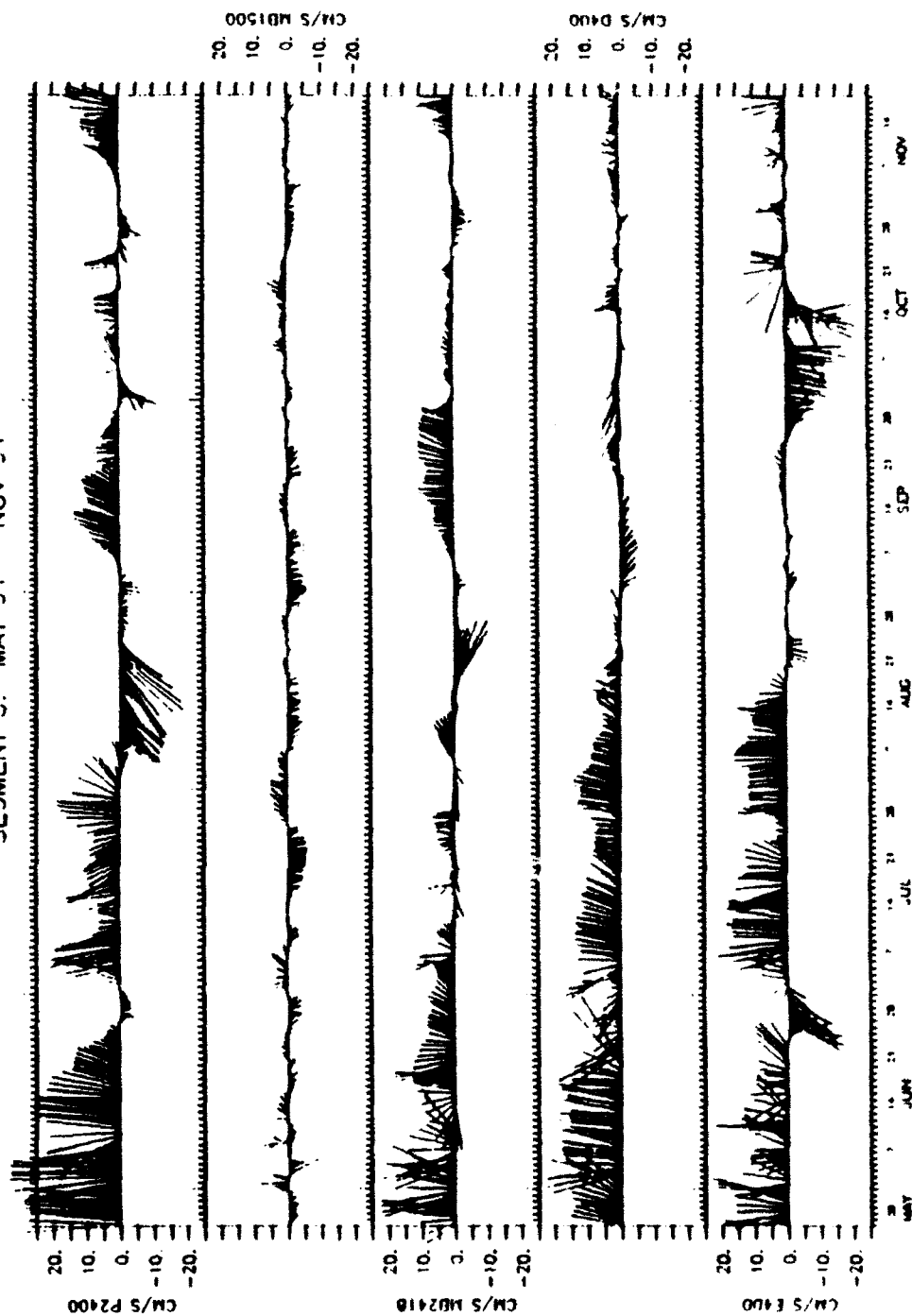
Figure 19.   **Segment 3 Vector Velocities:** Velocity vectors
are shown as in Figure 5. Data are from P2
(interpolated to 400 m; top), MB1 (second from
the top), MB2 (third from the top), D (second
from the bottom) and E (bottom).

69

of -1.0 cm sec^{-1} with a maximum onshore flow of 9.8 cm sec^{-1} and a maximum offshore flow of -18.6 cm sec^{-1}.

The statistics at MB2 were similar showing an alongshore mean of 4.2 cm sec^{-1} with a maximum of 23.2 cm sec^{-1} and a minimum of -10.2 cm sec^{-1} (Table 9a). The across-shore component had a mean of 0.9 cm sec^{-1} with a maximum of 17.9 cm sec^{-1} and a minimum of -10.9 cm sec^{-1} (Table 9b).

Table 9a.   TIME DOMAIN STATISTICS FOR SEGMENT 3
(ALONGSHORE COMPONENT)

Mooring	Meter depth (m)	Mean (cm/s)	Maximum (cm/s)	Minimum (cm/s)	Standard Deviation (cm/s)	Mode 1 Eigenfunction (Eigenvalue = 193.80 (cm/s)2 for 64.7% of total variance)	Mode 2 Eigenfunction (Eigenvalue = 65.18 (cm/s)^2 for 21.7% of total variance)
P2	400*	6.27	33.3	-19.0	10.73	0.70	-0.47
MB1	500	-0.56	8.4	-8.7	2.78	0.02	-0.07
MB2	416	4.19	23.2	-10.4	6.19	0.30	-0.38
D	400	5.99	23.6	-6.3	6.42	0.36	0.07
E	400	3.64	24.6	-21.8	9.84	0.53	0.79

* velocities interpolated between 350 m and 500 m

From the beginning of the time segment until 27 June the flow was poleward at P2 400 m, with the maximum over the entire segment (33.3 cm sec^{-1}) occurring around 02 June. On 27 June, the flow abruptly shifted to equatorward for four days and then reversed back to poleward until early August.

From around 07 August to 07 September a relatively strong (10-20 cm sec^{-1}) equatorward event dominated the currents at both P2 and MB2. The across-shore components at

these two moorings exhibited a remarkably strong negative correlation. Examination of the across-shore components of P2 and MB2 alone (Figure 20), clearly showed onshore flow at MB2 opposing offshore flow at P2 suggesting the presence of a mesoscale, rotating feature between the two moorings.

Table 9b.   TIME DOMAIN STATISTICS FOR SEGMENT 3
             (ACROSS-SHORE COMPONENT)

Mooring	Meter depth (m)	Mean (cm/s)	Maximum (cm/s)	Minimum (cm/s)	Standard Deviation (cm/s)	Mode 1 Eigenfunction (Eigenvalue = 31.96 (cm/s)2 for 41.3% of total variance)	Mode 2 Eigenfunction (Eigenvalue = 19.45 (cm/s)^2 for 25.1% of total variance)
P2	400*	-1.0	9.8	-18.6	4.9	-0.81	0.16
MB1	500	1.2	6.4	-3.6	1.3	-0.06	0.03
MB2	416	0.9	17.9	-10.9	4.0	0.56	-0.01
D	400	0.8	19.3	-12.9	4.2	-0.17	-0.67
E	400	-0.6	10.4	-19.0	4.2	-0.04	-0.73

* velocities interpolated between 350 m and 500 m

P2 currents in early August prior to the event were poleward but rotated clockwise slowly until 03 August. The current then shifted abruptly to equatorward and onshore briefly. Finally, it turned offshore on 07 August to begin the event. The current maintained an offshore, equatorward direction at P2 until the event ceased around 07 September (Figure 21). Following the event, the current shifted to poleward and onshore for approximately one month until an equatorward burst of about -10 cm sec^{-1} interrupted the flow on 28 September (Figure 19). A similar deviation occurred on

71

28 October. These equatorward signals appeared at about the same period as those observed in Segment 2 (30 days).

Currents at MB2, directed poleward and onshore during the beginning of the event, did not appear to feel the feature's influence until 13 August. On this day the current
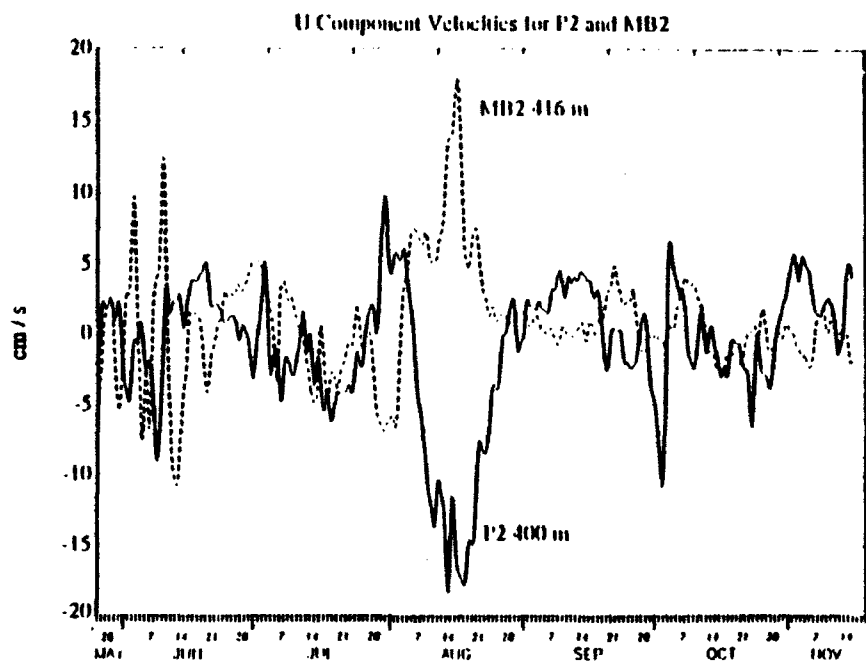
Figure 20. **Across-shore Component Velocities at P2 and MB2:** A mesoscale event commenced around 07 August, characterized by negative correlation for the next 25 days.

turned to equatorward and onshore and remained so until 07 September (Figure 21). Flow also shifted to poleward after the event here and followed a similar pattern as that described for P2; i.e. a poleward relaxation to a near 0 cm sec⁻¹ current on 28 September followed by an equatorward shift (-5 cm sec⁻¹) 30 days later. The flow at both P2 and MB2 during October and November appeared remarkably similar to

that during the same months, one year earlier in Segment 2 (Figure 12).

In general, poleward flow dominated from May until early August at both Farallon moorings. At mooring E though, the flow shifted to equatorward (max. -18 cm sec^{-1}) on 22 June and remained so for about 9 days thereafter. This occurred about five days prior to the equatorward shift described at P2, approximately 183 km to the south. However, moorings MB2 and D located between P2 and E, did not show such a shift so a connection between these equatorward interruptions does not seem likely. The shift at mooring E was probably due to a cold filament observed off Pt. Reyes, north of San Francisco Bay during this time segment (Ramp et al., 1992). Around 21 August, approximately two weeks after the start of the event at P2 and MB2, flow at moorings D and E weakened significantly and shifted from poleward to equatorward. This raised the question of whether or not a mesoscale event occurring some 140 km to the south could manifest itself into the flow pattern at D and E. With the limited data available, a connection between these two events seemed speculative but it does present an interesting possibility.

At mooring D, the flow shifted back to poleward around 27 September and remained weak (< 6 cm sec^{-1}) for the remainder of the segment (Figure 19). At mooring E, a strong equatorward reversal occurred around 23 September, which was
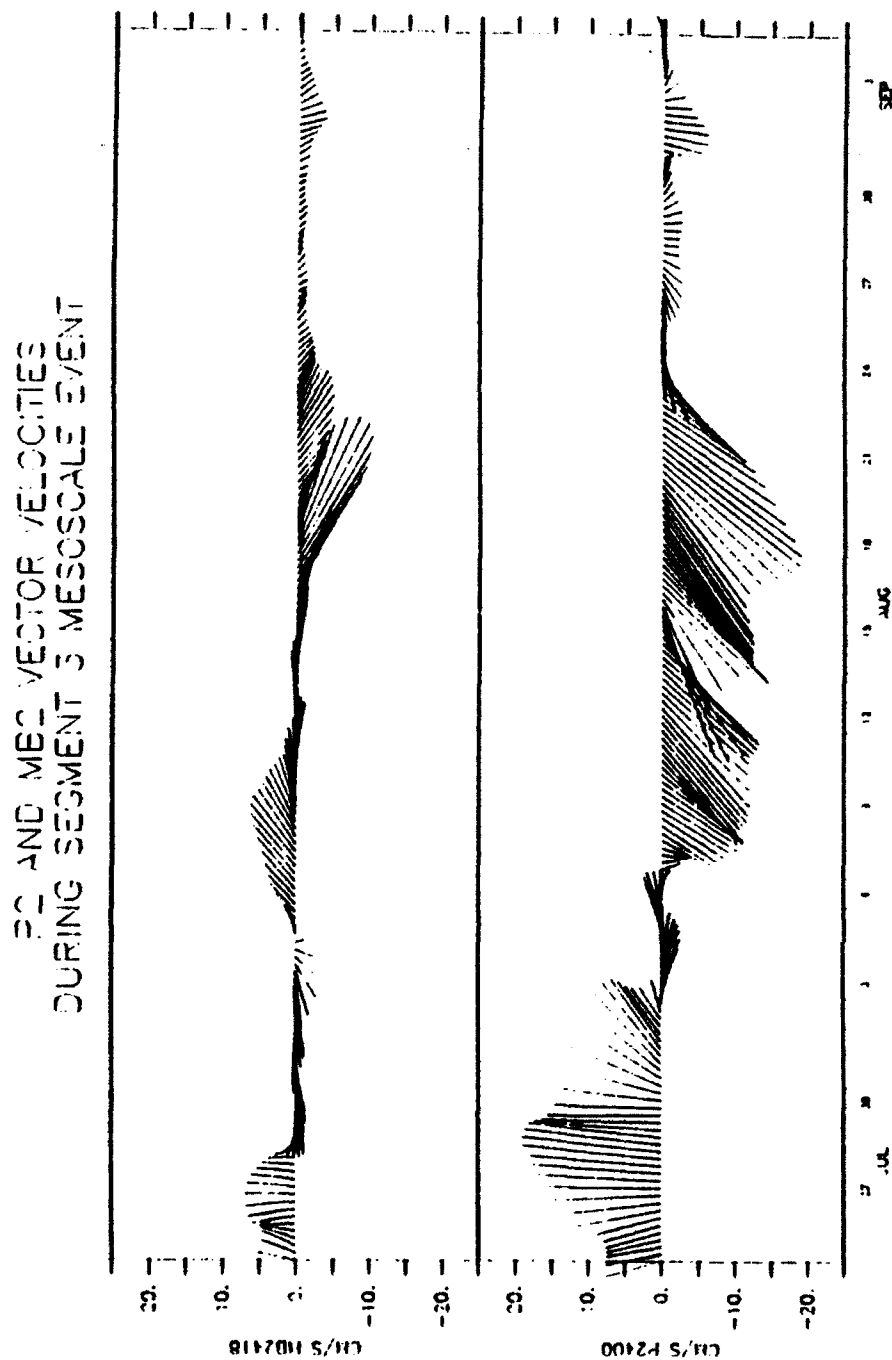
Figure 21. **Segment 3 Vector Velocities During Mesoscale Event:** Velocity vectors are shown 25 July through 04 September with details as in Figure 5. Data are from MB2 (top) and P2 (bottom).

74

not observed at mooring D. For the next month, the current at E grew steadily to a maximum of -18 cm sec^{-1}. It then shifted back to poleward on 21 October and remained fairly weak and much more variable (Figure 19).

In the empirical mode decomposition, the first two alongshore modes accounted for 66.4% of the variance. The mode 1 alongshore eigenfunction (Figure 22, top left) showed the flow at all moorings to have the same sign. As discussed previously, this could be interpreted as the poleward undercurrent seen in the stick vector plots. The mode 2 alongshore eigenfunction showed a divergent flow between the Farallon moorings and those to the south (Figure 22, bottom left). This could perhaps be due to the rotating feature observed at P2 and MB2, which impacted the currents there but not farther north at moorings D and E.

As with the other segments, the mode 1 across-shore eigenfunction at P2 and MB2 described an opposing flow structure (Figure 22, top right). Moorings D and E were not strongly correlated with the Pt. Sur and Monterey Bay moorings indicating that the mesoscale event at these southern locations dominated the mode 1 across-shore component structure. The mesoscale feature described earlier appeared to influence the mode 2 across-shore current structure as well. The MB2 mode 2 eigenfunction had a sign opposite to P2 (Table 9b) but the magnitude (-0.01) was much smaller than that at P2 (0.16) and thus does not show in Figure 22.

75

Modal amplitudes were again correlated with alongshore component time series (Table 10). P2 showed the strongest correlation with the mode 1 amplitudes having a correlation coefficient of 0.91. The P2 alongshore component plot and modal amplitude time series showed that this mooring
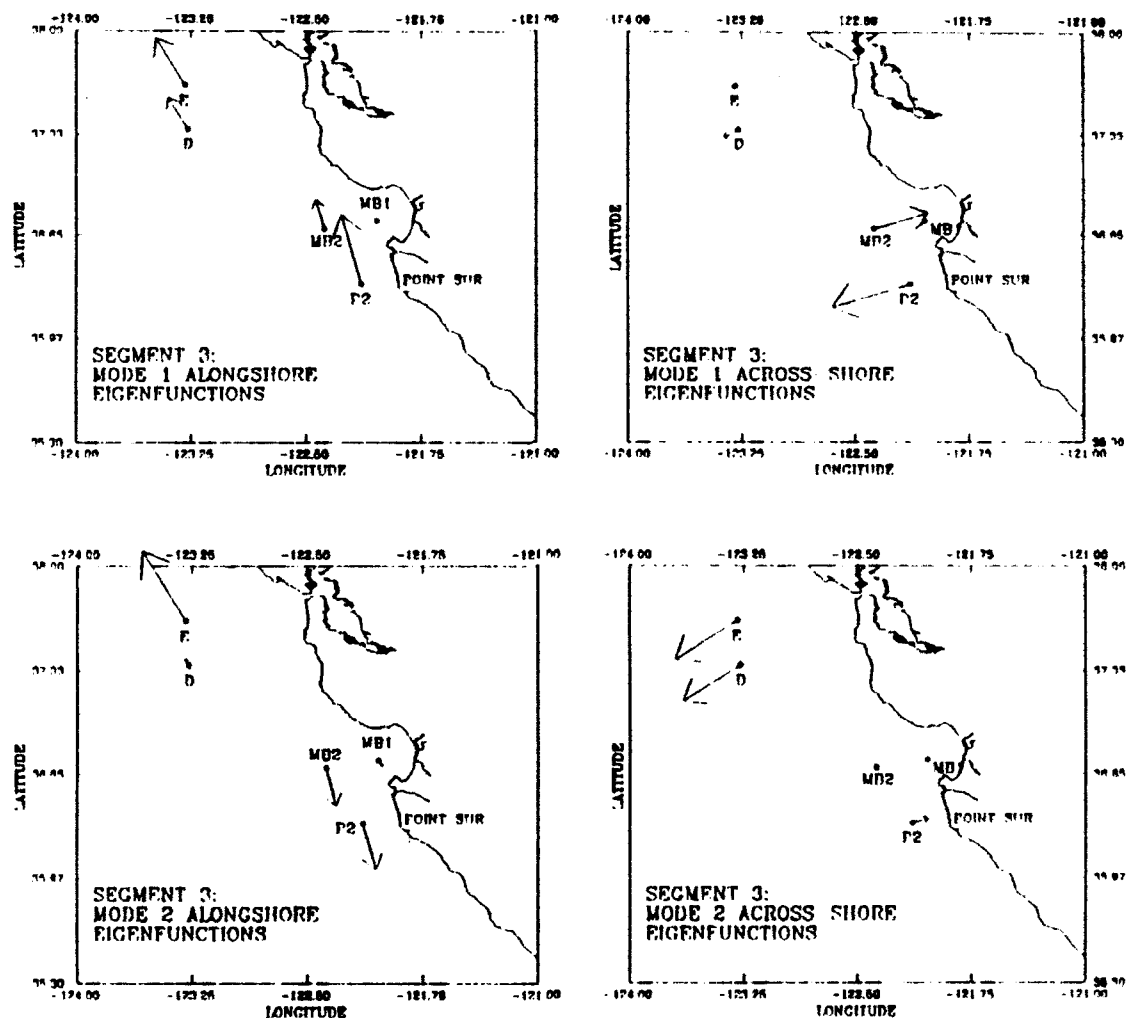
Figure 22. **Eigenfunction Amplitudes for Velocity Modes 1 and 2 During Time Segment 3:** Alongshore (left) and across-shore (right) eigenfunctions are shown with vectors proportionally scaled for visual effect. The across-shore modal

76

Table 10. **SEGMENT 3 CORRELATION COEFFICIENTS FOR FIRST AND SECOND MODE EIGENFUNCTIONS WITH TIME SERIES**

	Cross-shore		Alongshore	
	Mode 1	Mode 2	Mode 1	Mode 2
P2 400 m	0.91	0.35	0.92	0.15
MB1 500 m	0.10	0.20	0.26	0.09
MB2 418 m	0.67	0.50	0.80	0.01
D 400 m	0.78	0.09	0.23	0.70
E 400 m	0.75	0.65	0.05	0.76

contributed most of all the moorings to the mode 1 variance (Figure 23). Mooring E was most nearly correlated with the second mode alongshore eigenfunction (Table 10). P2 again showed the strongest correlation (0.92 coefficient) and the relationship between the two is illustrated in Figure 23. Much like the alongshore components, mooring E was best correlated with the mode 2 eigenfunction.

2. Frequency Domain Analysis

The variance conserving spectra (Figures 24a through 24 c) for alongshore components showed that Moorings D, E and P2 peaked at 29.2 days, similar to Segment 2. MB2 experienced a maximum energy level at a shorter period of 14.6 days. Mooring E contained the most energy, 102.9 cm^2 sec^{-2}. P2 had less energy with a 68.4 cm^2 sec^{-2} peak. MB1 showed a 19.5 day peak with an energy level of 11.0 cm^2 sec^{-2}. D and MB2 peaked
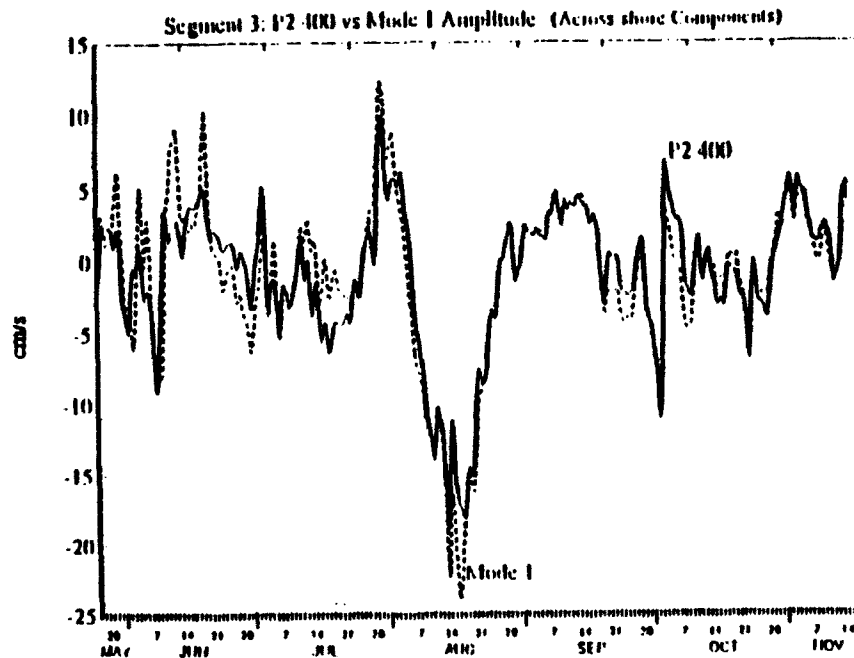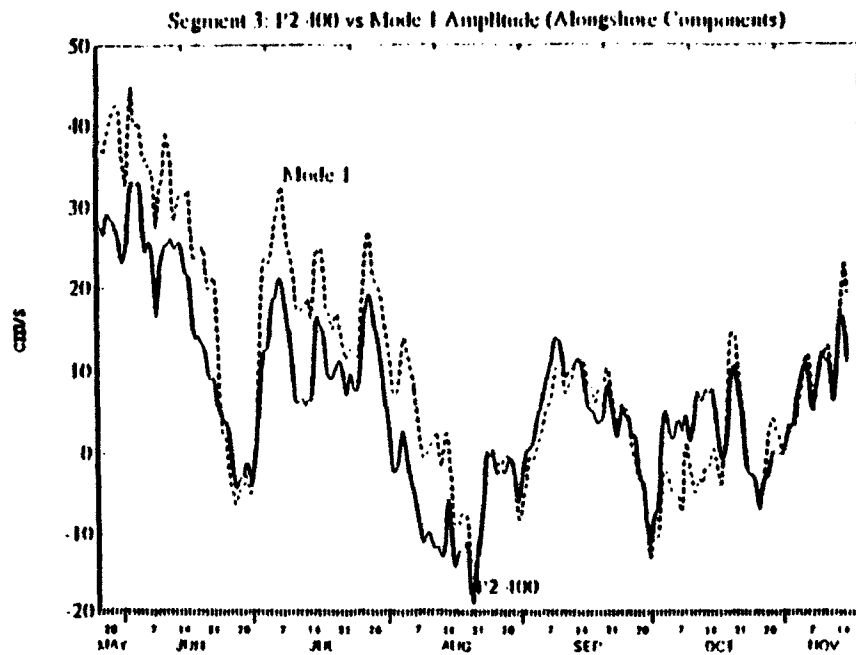
Figure 23. A Comparison of the Mode 1 Velocity Amplitudes with the Best Correlated Individual Time Series: The top panel shows the alongshore components and the bottom panel shows the across-shore components.

78
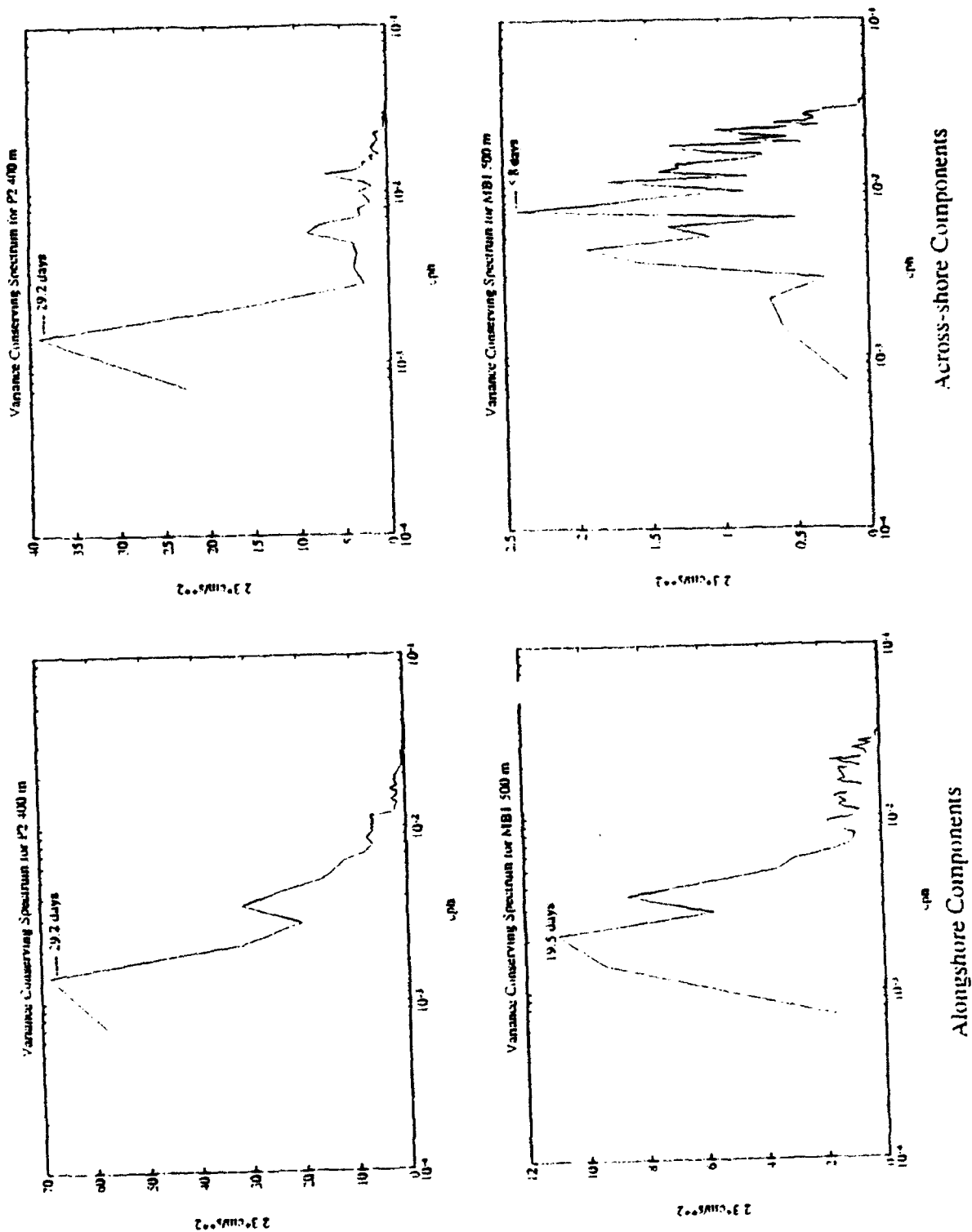
Figure 24a. Segment 3 Variance Conserving Auto-Spectra for P2 (top) and MB1 (bottom).
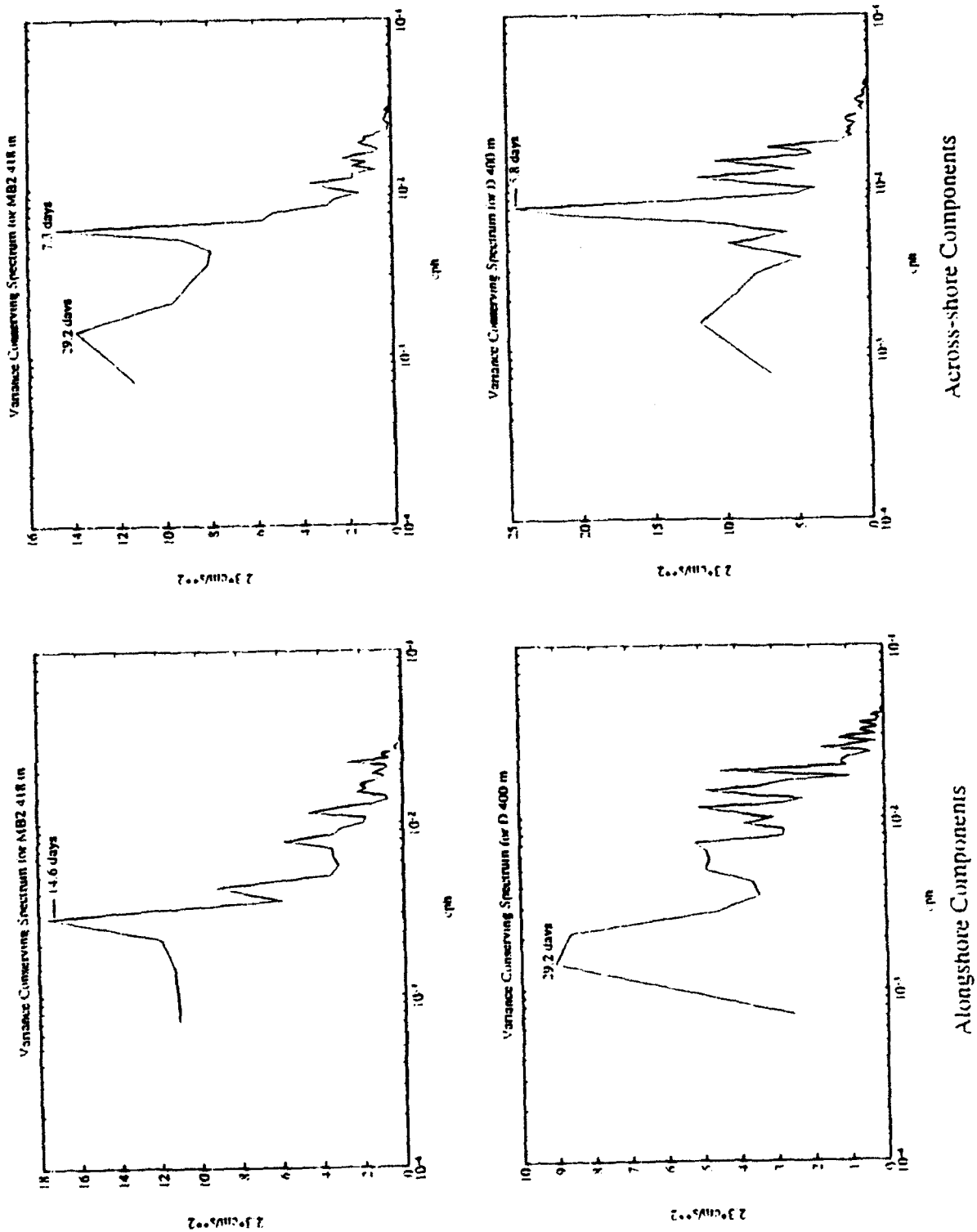
Figure 24b.   Segment 3 Variance Conserving Auto-Spectra for
MB2 (top) and D (bottom).

80
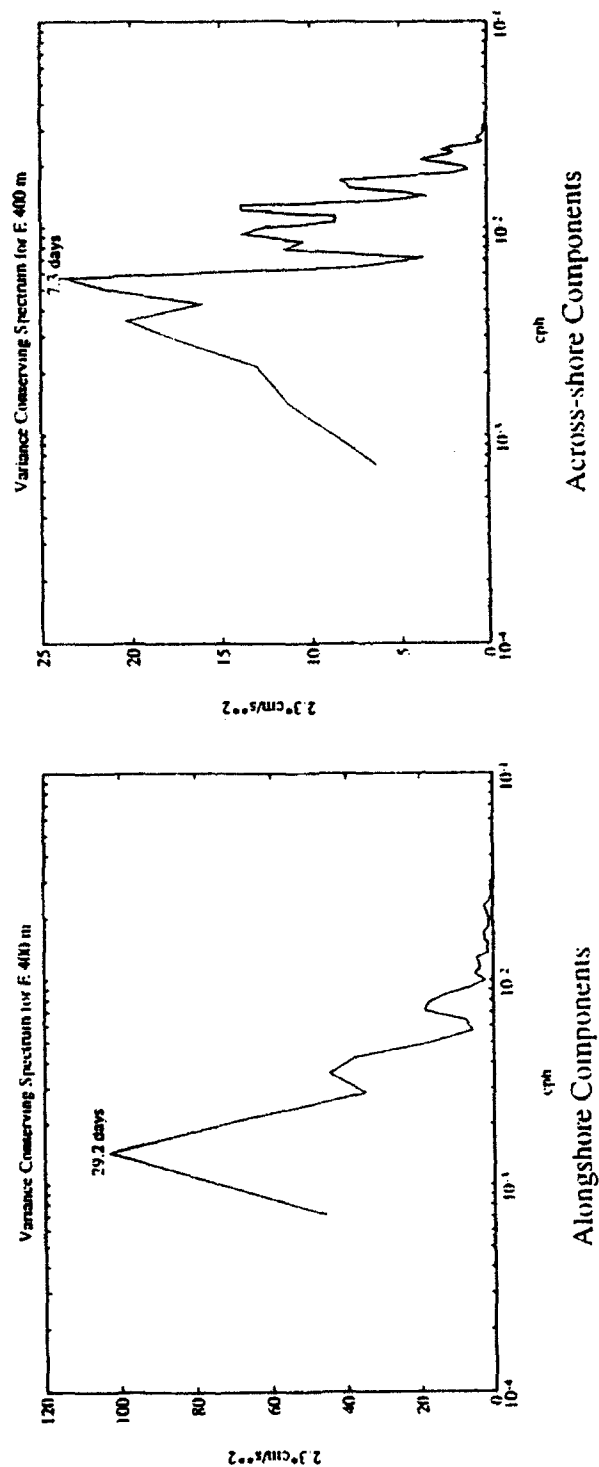
Figure 24c. Variance Conserving Auto-Spectra for Segment 3 Mooring E

with energy levels of 9.0 and 17.6 cm^2 sec^{-2} respectively (Figures 24a through 24c).

Across-shore component energy peaks occurred at periods ranging from 5.8 days (moorings D and MB1), 7.3 days (moorings E and MB2) and 29.2 days at P2 (Figures 24a through 24c). The peak at P2 contained the maximum energy of all moorings (39.0 cm^2 sec^{-2}) (Figures 24a through 24c). The pervasiveness of the 29.2 day peak is interesting, but missing this time at MB2 in both the alongshore and across-shore components.
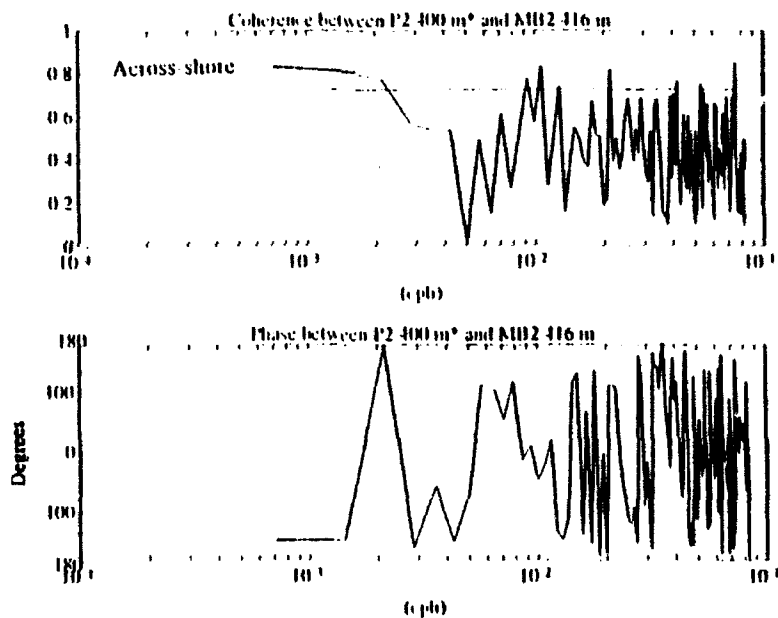
Figure 25. **Segment 3 Coherence and Phase for Across-shore Components for P2 and MB2·** The solid line on the coherence plot indicates the 95% significance level. The two mooring locations are coherent but 180° out of phase.

Cross spectra showed the only coherent alongshore component signal between moorings D and E at periods from 9.7 to 8.4 days. The energy levels at these periods were significantly smaller than at longer periods; thus the importance of this coherence is not clear. Significant coherence occurred between the P2 and MB2 across-shore components at periods from 58 to 19.5 days (Figure 25). These signals were $\approx 180°$ out of phase supporting the opposing flow structure resulting from the presence of a rotating mesoscale feature. No other coherent signals were observed between any other mooring pairs.

V. DISCUSSION

A. CALIFORNIA UNDERCURRENT

Time series plots and EOF analysis consistently demonstrated a predominantly poleward flow during the three time segments at all moorings. These results were generally consistent with the flow of the California Undercurrent (CUC) as described by Chelton (1984), Wickham et. al (1987) and Robson (1990). Chelton (1984) computed seasonal geostrophic velocities and found the maximum poleward current occurred during December off Point Sur. Segments 1 and 2 time series, however, showed current maxima during February. Chelton based his calculations on long term averages of all available data from the California Cooperative Oceanic Fisheries Investigations (CALCOFI). The reliability varied from month to month and from location to location and could possibly explain the difference between Chelton's findings and those of Segments 1 and 2. Also, Chelton considered the entire water column to include currents extending to the surface while these results examined the 350 - 500 m depths only. The important point is that definite poleward maxima existed during winter in both Segments.

The CUC signature during Segment 3 agreed well with Wickham et. al (1987) who found predominantly annual

variability at Point Sur with a maximum poleward flow in May and June. Specifically, Segment 3 time series clearly showed a maximum at all locations to include Point Sur, Monterey Bay, and the Farallon Islands moorings during May 1991. During the first two segments, the flow at P3 provided the most consistent poleward flow and did not exhibit the periodic reversals to equatorward flow seen at P2.

B. COASTAL TRAPPING

Although the poleward flowing CUC dominated the mean currents, a low frequency oscillation was superimposed on the poleward undercurrent during Segment 2 (October 1990 to January 1991). This deviation was observed more clearly at P2 than at P3 indicating the presence of a coastally trapped phenomenon. If a wavelike feature is assumed, the coherence and phase information presented earlier can be used to calculate phase speeds and wavelengths for the different energetic peaks in the spectrum (Table 8). These can be compared with the dispersion relations for different kinds of simple coastally trapped waves to see if they provide a reasonable explanation for the frequencies, wavelengths and phase speeds observed.

1. Rossby radius of deformation

Significant evidence supported the importance of coastal-trapping. First, calculation of the internal Rossby Radius of deformation revealed that P2 lied close to one

Rossby radius of the shelf break while P3 was located outside of this radius. The internal Rossby radius of deformation represents the horizontal scale at which rotation effects become as important as the buoyancy effects (Gill 1982). An expression for this scale can be derived following the procedure outlined in Gill (1982):

$$a_n = \frac{c_n}{\lceil f \rceil} \qquad (14)$$

where $c_n = \sqrt{gH_n}$ represents the wave speed of the nth mode and

$H_n = \frac{\overline{N}H}{gn\pi}$ is the equivalent depth. An expression for the

Rossby radius was determined by substituting the equivalent depth into the equation for c_n and then substituting c_n into (14) to get:

$$a_n = \frac{\overline{N} H}{n\pi f} \qquad (15)$$

CTD casts conducted near P2 provided Brunt-Vaisala (N^2) profiles for October, November, December 1990 and February, 1991. Using the standard equation:

$$N = (-\frac{g}{\rho}\frac{\partial\rho}{\partial z})^{\frac{1}{2}}$$

a depth averaged value of 5.50×10^{-3} rad sec^{-1} was found. Using the current meter mooring depth at P2 (800 m) for H and the Coriolis parameter of 8.65×10^{-5} rad sec^{-1} produced a

86

first mode (n=1) Rossby radius of 16.2 km, and explained why
coastal trapping influenced the flow at P2 more strongly than
it did at P3 (Figure 26).

DISTANCE OFFSHORE (KM)
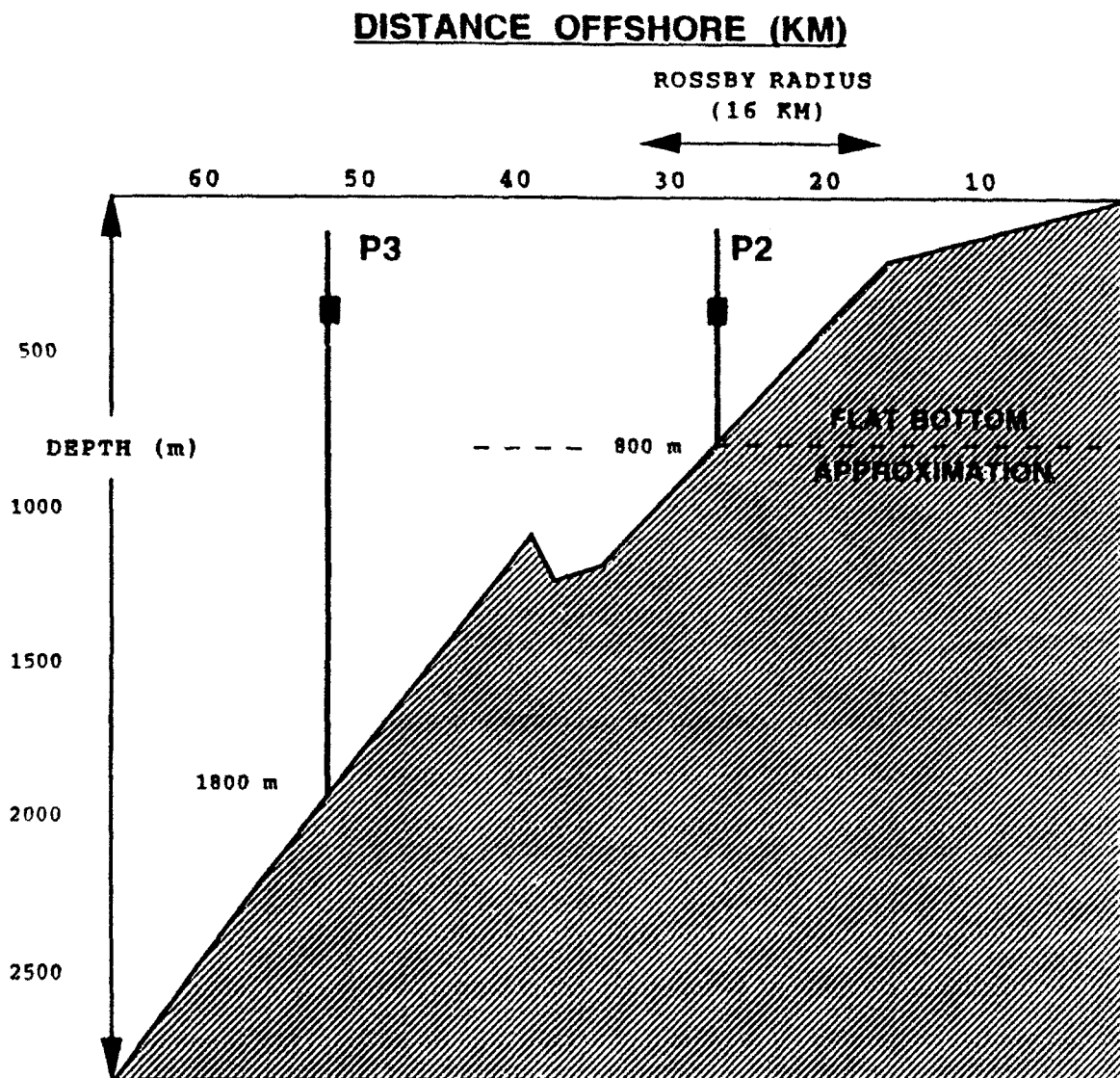
ROSSBY RADIUS
(16 KM)

Figure 26. **Schematic Cross Section Between P2 and P3:**
Diagram shows the bottom slope and the Rossby
radius of deformation, drawn to scale at the top
of the plot.

2. Critical Latitude for Coastal Trapping

Additional support for coastal-trapping in the vicinity of Point Sur came from a study by Clarke and Shi (1991). A simple formula produced the critical frequency at which waves become trapped at a given latitude:

$$\omega_c = \frac{\beta c_n}{2 f_o} \cos\theta \qquad (16)$$

where β is the latitudinal change in planetary vorticity (2×10^{-11} m^{-1} sec^{-1}), c_n = the phase speed for the nth internal mode, f_o = the Coriolis parameter (8.64×10^{-5} sec^{-1}) and θ is the angle between the coastline and true north determined from a chart to be 35°. Using the expression:

$$c_n = \frac{\overline{N} H}{n \pi}$$

with $\overline{N} = 5.5 \times 10^{-3}$ rad sec^{-1} and H = 800 m, gives a value of $c_1 = 1.40$ m sec^{-1}. Substituting into (16) yields a frequency of 1.33×10^{-7} sec^{-1} or a period $(T=\frac{2\pi}{\omega})$ of 548 days. Waves with periods greater than this will leak offshore in the form of a planetary Rossby wave while smaller periods are coastally trapped. Both observed periods (29.2 and 19.5 days) were well within this maximum trapping period offering additional evidence to strengthen the argument that the low frequency

oscillations observed off Point Sur were trapped near the coast.

3. Poleward Propagation

Alongshore component phase observations from Segment 2 show that the oscillation propagated poleward at all periods (Figures 16 and 17). This supports the theory presented in Chapter I that coastally trapped phenomena propagate in a direction such that the coastal boundary is on the right in the northern hemisphere. In all cases except the 19.5 day signal, the equatorward reversals propagated from P2 towards the north (Figure 17). This evidence along with the Rossby radius information and critical trapping latitude prompted a more detailed analysis of possible coastal trapping mechanisms. The analysis focused on alongshore component phase observations only, since the majority of the variance was contained here.

C. Possible Coastal Trapping Processes

1. Internal Kelvin Waves

As discussed in Chapter I, the presence of an IKW first required the assumption of a flat bottom with a vertical boundary at the coast. The solution to the momentum equations based on these assumptions produced two waves: one that exponentially decayed from the coast seaward and the other which grew exponentially from the coast seaward. The former represents the only physical solution and propagates poleward

along an eastern boundary. The dispersion relationship of Equation (12) facilitated a comparison between the observed wavelengths and theoretical wavelengths. Only the periods of maximum energy (29.2 and 19.5 days) were considered. Since ω and H were well known compared with 1, the dispersion relation was rearranged to produce a solution for the alongshore wave number for each internal mode (n):

$$l^2 = \frac{(\frac{n\pi}{H}\omega)^2}{(N^2 - \omega^2)} \qquad (17)$$

By substituting known quantities into (17), a theoretical value for the alongshore wave numbers and hence wavelengths for the two periods of interest could be obtained. In (17): $T_1 = 29.2$ days, $\omega = \frac{2\pi}{T_1} = 2.49 \times 10^{-6}$ rad sec^{-1} ($T_2 = 19.5$

days, $\omega_2 = 3.70 \times 10^{-6}$ rad sec^{-1}), H = the P2 mooring depth (800 m) and $\bar{N} = 5.5 \times 10^{-3}$ rad sec^{-1}, i.e., the same value used in the Rossby radius calculation. The results (Table 11) show that IKWs of these periods are expected to have much larger wavelengths than those observed. The wavelengths decrease with increasing n, but modes higher than 1 or 2 have not been observed in the ocean so this seems an unlikely explanation. Our $\bar{N}$ is, if anything an underestimate, and larger H makes the theoretical wavelength larger so this cannot reduce the discrepancy.

90

Table 11. OBSERVED WAVELENGTHS COMPARED WITH INTERNAL
KELVIN WAVE (IKW) AND CONTINENTAL SHELF
WAVE (CSW) THEORY

	Observed Wavelength (km)	IKW Theoretical Wavelength (km)		CSW Theoretical Wavelength (km)
		n = 1	n = 2	
T_1 = 29.2 Days	390	3538	1769	28
T_2 = 19.5 Days	351	2381	1191	27

Since $\overline{N}$ was well observed, we conclude that pure IKWs cannot explain the observed phase relationships during Segment 2.

2. Barotropic Continental Shelf Waves

These waves provide the opposite "end point" for comparison with the calculations. As in the IKW procedure, rearranging the CSW dispersion relationship from Chapter I provided a means to calculate a theoretical alongshore wavenumber and wavelength for a CSW:

$$l^2 = \frac{2fk\lambda}{\omega} + k^2 + \lambda^2 \tag{18}$$

where f is the Coriolis parameter (8.64×10^{-5} rad sec^{-1} for $36°$-20' N), k is the observed across-shore wave number, λ is the bottom slope parameter $(-\frac{1}{2H}\frac{dh}{dx})$ and ω is the observed wave frequency. Using a depth of 800 m (P2 mooring depth), a **dh** of 1800 m, a **dx** of 52 km (distance to P3), λ = 2.16×10^{-5} m^{-1}. Alongshore wavenumber calculations produced a wavelength of 28 km for the 29.2 day signal and 27 km for

the 19.5 day signal (Table 11). Assuming that less than one complete wavelength fit between mooring locations, these waves are too short to explain the observations. The preliminary conclusion is that the waves are either 1) hybrid waves where both bottom slope and stratification are important or 2) waves which are scattered/reflected by the Monterey Canyon, which renders conventional dispersion relations useless.

3. Limitations of CTW Theory

The differences in Table 11 can be explained by examining the governing assumptions behind each dispersion relationship. First, IKW theory assumed a flat bottom with a vertical wall. This assumption is not valid since the Monterey Canyon passes directly between P2 and MB2 (Figures 1 and 11). On the other hand, CSW theory assumed homogeneity with a sloping bottom. Hydrographic data in this region shows vertical density stratification (Robson, 1990) and weakens the homogeneous assumption. Therefore, it seems that the observed oscillations are produced by a complex interaction of both processes.

Finally, while the wavelength calculations for IKW is non-ambiguous, it is possible in the case of shelf waves that more than one wavelength "fits" between moorings P2 and MB2. If the actual phase difference, for instance, was $360° + 38°$ = $398°$, rather than $38°$, then a wavelength of 37 km is implied, in closer agreement with the observed wavelength.

92

This idea is speculative, but does represent an alternate solution to the problem.

4. Additional Evidence Supporting Coastal Trapping

Vertical coherence and phase were calculated at P2 from May 1989 through October 1990 (17 months). Current meter data at 100 m, 350 m and 500 m showed an upward vertical phase propagation consistent with results of Romea and Allen (1983) suggesting an IKW presence. Romea and Allen (1983) focused on low frequency behavior with periods similar to those observed during Segment 2 (T ≈ 20 - 40 days). They employed a model that examined "the response of a rotating, stratified, f-plane ocean with a rigid lid, forced by an alongshore wind stress at the coast." They calculated the response for three different types of wind stresses: winds acting for a brief time at a single point, winds acting for a longer time at a single point and more generally, winds acting over a larger area for a long time. Their model showed that bottom reflections could be ignored if (1) the bottom is highly dissipative, (2) if the waves have sufficiently low frequencies and travel a great distance before hitting the bottom or (3) if the waves are internally dissipated prior to reaching the bottom. They also showed that a poleward travelling wind forced a poleward propagating component in the form of a coastally trapped IKW that had a phase velocity directed upward and a group velocity

directed downward i.e., consistent with the results observed at P2.

Several other models have addressed CTW forcing mechanisms. Chapman (1987) applied wind forced, long coastal-trapped wave theory in an attempt to hindcast quantities observed during the Coastal Ocean Dynamics Experiment (CODE) which took place in the vicinity of Point Arena during 1981 and 1982. He found that bottom pressure and alongshore current were forced by winds between Pigeon Point, (200 km south of the CODE site) and the CODE site itself. Battisti and Hickey (1984) also found that sub surface pressure (SSP) response off Washington and Oregon resulted from wind forcing between San Francisco and Cape Mendocino over the entire low frequency band for periods greater than 5 days. They found that local wind forcing was negligible during the summers of 1972 and 1978, and thus remote forcing was responsible for fluctuations in SSP observed then. Finally, Lopez and Clarke (1989) considered a solution forced by combined local and remote winds where the local solution disregarded the alongshore pressure gradient but allowed local winds and the remote solution assumed local winds were zero and the alongshore pressure gradient $P_y \neq 0$. They considered periods between 22 and 45 days. Although these models focused on continental shelf phenomena, the results consistently show that remote wind forcing, south of the current observation

resulted in coastal trapping at periods in general agreement with those observed during Segment 2.

Vertical coherence and phase were also calculated at P3 with data from October 1990 through May 1991 (8 months). During this time period current meters were located at depths of 100 m, 350 m, 500 m and 1000 m. In contrast to the results at P2, a downward vertical phase propagation was observed for all current meter combinations. This indicates that P3 was more affected by surface phenomena such as meanders and eddies, than by coastal trapping.

As discussed in the previous chapter, other significant dynamical differences between P2 and P3 were observed during the first two time segments. To review, the current at P3 during Segment 1 showed a persistent poleward flow interrupted only by a strong equatorward event toward the end of the segment. This event appeared at the surface and extended down to at least 1000 m (unpublished data). Additionally, the equatorward reversals observed at P2 and the Monterey Bay moorings during Segment 2 were less apparent at P3, i.e., currents at P3 appeared to be influenced less by the coastal boundary. This makes sense in light of P3's location well outside of the Rossby radius. With this evidence, we conclude that data from P2 and P3 were representative of two dynamically unique environments: an upper slope or near shore regime (P2) and a lower slope or offshore regime (P3).

5. Further Possible Analysis

A more rigorous analysis of this problem would require a dedicated numerical model that considers both irregular bathymetry and density stratification. Wilkin and Chapman (1990) used such a model to study freely-propagating CTWs. Their model attempted to simulate scattering of CTWs at a site on the East Coast of Australia. They found that CTW scattering strength varied with both bottom topography and density stratification creating an extremely complex interaction between these processes. The region studied in Segment 2 of this analysis appeared to be influenced by similar complicated interactions. A model specifically designed to account for the highly variable bathymetry of the Monterey Canyon would be necessary to produce more meaningful results.

D. THE MONTEREY BAY MEANDER

1. General Description

Satellite imagery from the Advanced Very High Resolution Radiometer (AVHRR) on the NOAA 11 satellite reveals that a distinct meander dominated the surface flow on 01 September 1991 (Figure 27). This picture provides the best image during the time frame of the energetic feature which dominated Segment 3. The image exhibits characteristics similar to those observed by Tracy (1990). In particular, a warm core, anti-cyclonic meander with a radius of

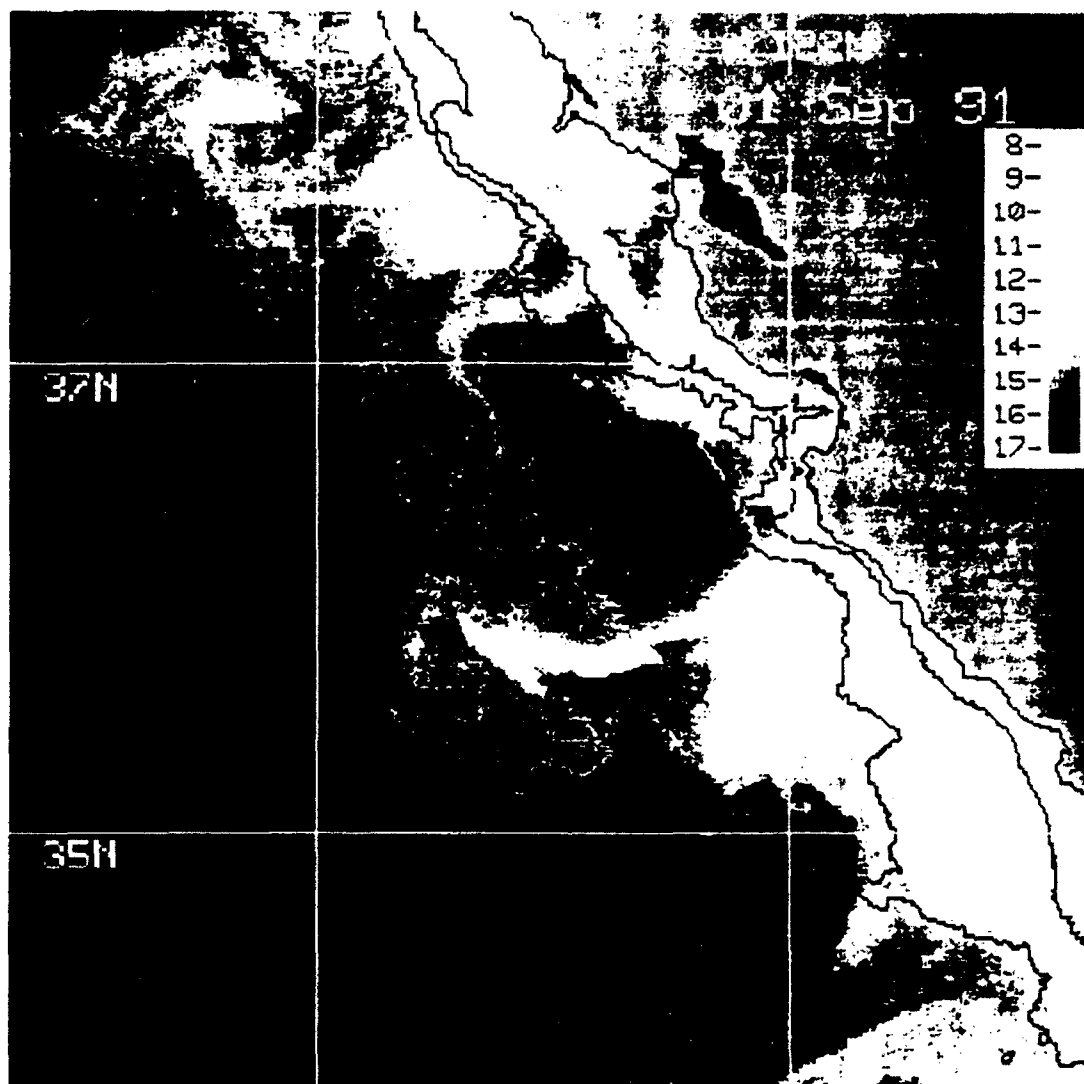**Figure 27.** **AVHRR Sea Surface Temperature Image for
01 September 1991:** The different gray shades
correspond to different temperatures with white
representing the coldest water (<12° C) and
black the warmest water (17° C). Velocity
vectors from 400 m at P2 (to the south) and MB2
(to the north) are shown in white and indicate
equatorward flow at both moorings. Vectors are
proportionally scaled for visual effect.

approximately 65 km can be inferred off Monterey Bay from the temperature gradient in the image (Figure 27). The meander is bounded to the south by a pronounced cold filament extending some 150 km ofr Point Sur and to the north by a pocket of cold water off Ano Nuevo probably due to intense upwelling often observed there. Tracy (1990) described conditions that allowed a similar meander to move shoreward and cause radical temperature changes inside the Monterey Bay.

It is important to examine whether features such as this impact the currents at 400 - 500 m depth. Ramp et al. (1991), Huyer et al. (1991), and Kosro et al. (1991) described a similar meander and cold filament off Point Arena in June 1987. The Point Arena meander displaced isopycnals to depths greater than 500 m. Geostrophic velocities calculated by Robson (1990) confirmed that surface flow reached depths of 500 m just outside of Monterey Bay. Additional measurements at mooring P3 at other times show strong eddy-like features extending to depths > 1000 m during spring 1990 and 1991. The current patterns described in Segment 3 also suggested that the surface feature extended to the instrument depths at P2 (500 m) and MB2 (418 m).

Poleward currents dominated the flow at both P2 and MB2 prior to 07 August (Figures 19 and 21). It is believed that the shoreward movement of the meander caused this poleward flow to reverse at P2 first and then MB2. From 07 to 24 August, currents were onshore at MB2 and offshore at P2

suggesting that MB2 was located in the northern boundary of the meander while P2 was in the southern boundary. From 14 August until 03 September, the flow was equatorward at both moorings indicating that the surface jet seen in the satellite image extended down to the current meter depths at P2 and MB2. The mean current vectors from 01 September at 400 m are superimposed on the image, and verify this equatorward flow on the edge of the meander.

Temperature records at P2 and MB2 also showed the meander's influence at depth. As the meander moved onshore, the temperature at the two instruments increased steadily (Figure 28). After this rise frequent temperature fluctuations, perhaps associated with the highly variable frontal position, were observed at both moorings (Figure 28). As the meander retreated, both moorings experienced a sharp, simultaneous drop in the temperature around 24 August possibly due to the cold tongue of water surrounding the meander (Figure 27).

The Segment 3 vector velocity plot (Figure 19) presented another remarkable issue. Shortly after the onset of the deep meander near Monterey Bay, steady poleward flow at the Farallon moorings D and E, weakened significantly and actually reversed to equatorward. Could deep interaction nearly 200 km to the south somehow "shut off" the source of the poleward flowing California Undercurrent? Although at
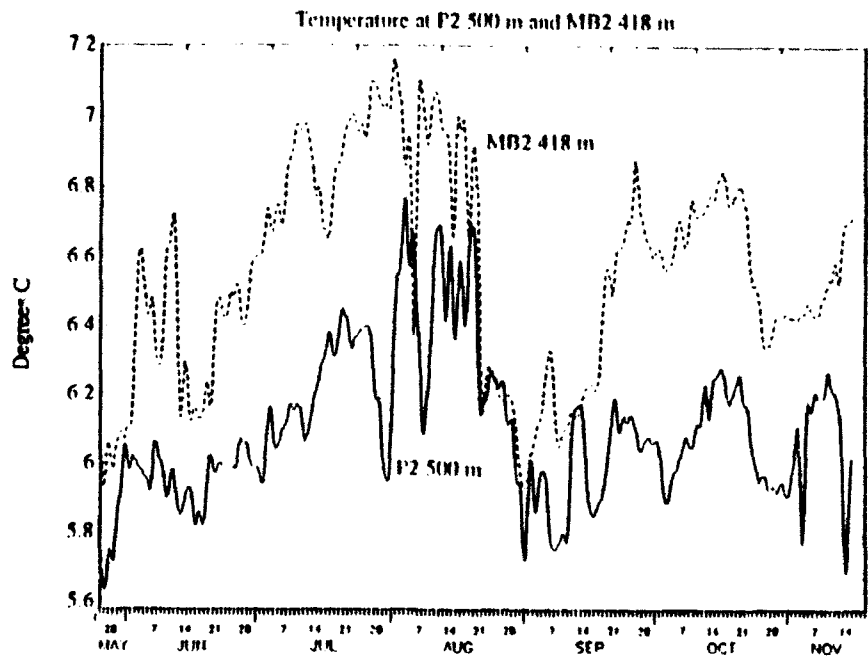
Figure 28. **Temperature Time Series at P2 500 m and MB2 418 m:** Plots show the rise and subsequent drop in temperature at the moorings due to across-shore excursions of the Monterey Bay Meander.

first glance there appeared to be some connection, it would be imprudent to speculate further without additional evidence.

E. EXPLAINING THE EOF'S

1. Mode 1 California Undercurrent

EOF analysis provided additional evidence to support the presence of the CUC. Throughout all three time segments, first mode EOF results consistently depicted a poleward flow at all locations except MB1, located inshore of the CUC in the Monterey Canyon. The utility of this technique relied on the

100

orthogonality principle; i.e., eigenvalues of a covariance matrix are orthogonal to each other and allow the flow to be separated into distinct patterns. EOF analysis works best when the first few modes explain most of the variance. Wallace and Dickinson (1972) described this as a necessary criteria to establish physical significance. The first mode alongshore eigenvalues explained between 64% and 66% of the variance with higher modes decreasing significantly (Figure 29). Therefore, the mode 1 result is attributed to the dominant poleward flow of the California Undercurrent.

2. Segment 2

The mode 2 EOF structure is most likely due to the presence of significant deviations from the mean flow. In Segment 2, the mode 2 structure can be attributed to the coastal trapping phenomenon believed to dominate the segment. Figure 13 (bottom left) shows this idea the best. Specifically, the mode 2 structure at P3 opposed that at P2 and MB2 suggesting that the trapping occurred most efficiently shoreward of P3.

3. Segment 3

In Segment 3, both mode 1 and mode 2 eigenfunctions displayed characteristics consistent with the Monterey Meander that dominated the flow at P2 and MB2 (Figure 22). In the alongshore component, the mode 2 eigenfunction showed that both MB2 and P2 had the same sign which opposed the flow at D
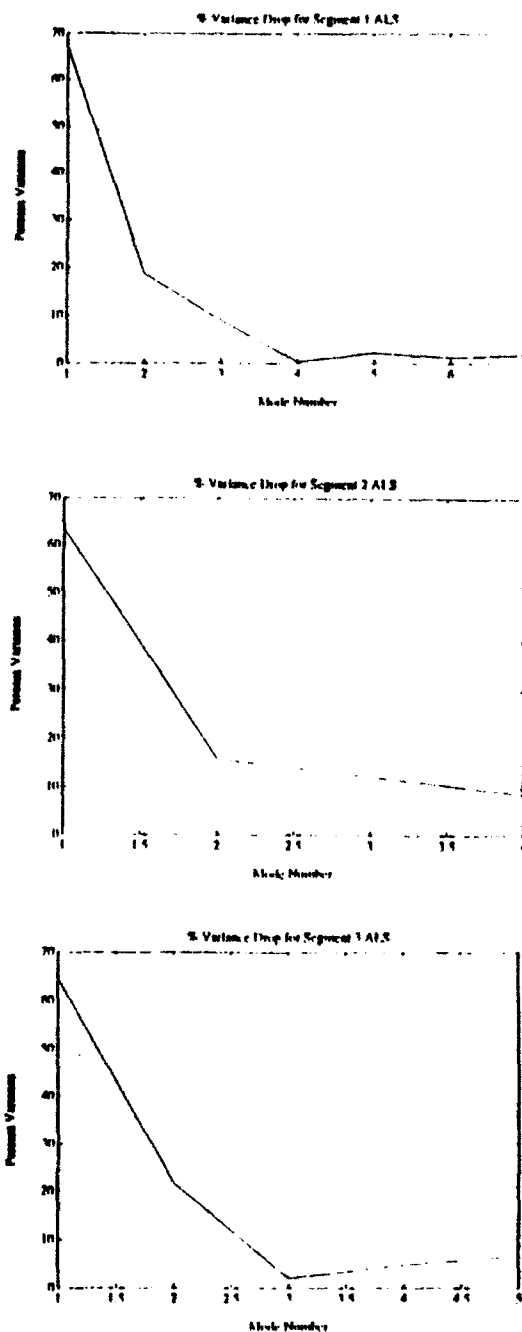
Figure 29. **Percent Variance Decrease for Alongshore Eigenmodes:** Shown are the percentages of variance explained (ordinate) vs. mode number (abscissa) for Segment 1 (top), Segment 2 (middle) and Segment 3 (bottom).

and E. This could be attributed to the strong equatorward influence of the meander as described above. In the across-shore component, mode 1 showed this structure the best with flow at P2 opposing that at MB2. This can be explained by the onshore flow at MB2 opposing the offshore flow at P2 while the meander passed through these moorings.

VI. CONCLUSIONS AND RECOMMENDATIONS

Three time segments of sub-thermocline (350 - 500 m) current meter data along the central California coast were examined to determine alongshore low frequency variability on time scale of two days to several months. Time and frequency domain analyses yielded three basic conclusions: (1) the poleward flowing California Undercurrent (CUC) dominated the mean flow during all segments; (2) the presence of a coastal-trapped significantly influenced the flow between P2 and MB2 during Segment 2 and (3) the deep flow at P2 and MB2 was influenced by a strong equatorward meander of the California Current.

The mean flow in all segments closely resembled that expected for the CUC. Segment 1 (December 89 - April 90) most nearly followed this mean pattern with few significant deviations. The first empirical mode in all segments consistently revealed a poleward current structure. Seasonal maxima occurred during February and May and showed close agreement with other findings in the vicinity of Point Sur.

Segment 2 (August 90 - March 91) displayed a significant deviation from the mean flow in the form of a coastal-trapped wave. The observed wavelengths between those for an internal Kelvin wave and a continental shelf wave were suggestive of a complex interaction between density stratification and the

104

complicated bathymetry of the Monterey Canyon. The wave influenced P2 and MB2 much more than P3, located outside of the internal Rossby radius. Though not specifically addressed in this research, wave forcing models developed by other researchers yielded results not inconsistent with the possible forcing mechanism in the Segment 2 wave. Further study of coastal-trapping should include an intensive numerical analysis that considers both density stratification and complex bathymetry.

Segment 3 (May 91 - November 91) represented another deviation from the mean poleward flow. An anti-cyclonic meander, clearly visible from satellite imagery, appeared to influence the flow down to 500 m. Cross-shore velocity component analysis at P2 and MB2 showed a strong negative correlation indicating the presence of an anti-cyclonic rotating feature. Additionally, temperature time series fluctuated in a manner that clearly showed the meander's influence. The meander appeared to disrupt the California Undercurrent some 200 km to the north at the Farallones moorings. An intensive hydrographic study encompassing Monterey Bay would provide insight into the surface feature-depth interaction and possibly improve the understanding of the California Undercurrent forcing.

REFERENCES

Aanderaa Instruments Technical Description No. 159, 1990: *Operating Manual RCM 7 & 8*, Aanderaa Instruments, Bergen, Norway, 74 pp.

Anderson, N., 1974: "On the Calculation of Filter Coefficients for Maximum Entropy Spectral Analysis," *Geophysics*, **39**, 69-72.

Battisti, D.S., and B.M. Hickey,1984: "Application of Remote Wind-Forced Coastal Trapped Wave Theory to the Oregon and Washington Coasts," *J. Phys. Oceanogr.*, **14**, 887-903.

Beardsley, R.C., D.C. Chapman, K.H. Brink, S.R. Ramp, and R. Schlitz, 1985: "The Nantucket Shoals Flux Experiment (NSFE79). Part I: A Basic Description of the Current and Temperature Variability," *J. Phys. Oceanogr.*, **15**, 713-748.

Chapman, D.C., 1987: "Application of Wind-Forced, Long, Coastal-Trapped Wave Theory Along the California Coast," *J. Geophys. Res.*, **92**, 1798-1816.

Chelton, D.B., 1984: "Seasonal Variation of Alongshore Geostrophic Velocity Off Central California," *J. Geophys. Res.*, **89**, 3473-3486.

Chelton, D.B., A.W. Bratkovich, R.L. Bernstein, and P.M. Kosro, 1988: "Poleward Flow Off Central California During the Spring and Summer of 1981 and 1984," *J. Geophys. Res.*, **93**, 10,604-10,620.

Clarke, A.J. and C. Shi, 1991: "Critical Frequencies at Ocean Boundaries," *J. Geophys. Res.*, **96**, 10,731-10,738.

Daggett, F.L., *A Study of the Velocity Structure Near a Cold Filament from ADCP and CTD Measurements*, Master's Thesis, Naval Postgraduate School, Monterey, California, September 1989.

Denbo, D.W., K. Lolain, J.S. Allen, A. Huyer, and R.L. Smith, 1984: "Current Meter Observations Over the Continental Shelf Off Oregon and California February 1981 - January 1984," Data Report 112, Ref. 84-12, November 1984, College of Oceanography, Oregon State University, Corvallis, Oregon.

Denbo, D.W. and J.S. Allen, 1987: "Large-Scale Response to Atmospheric Forcing of Shelf Currents and Coastal Sea Level Off the West Coast of North America: May - Juy 1981 and 1982," *J. Geophys. Res.*, **92**, 1757-1782.

Gill, A.E., *Atmosphere-Ocean Dynamics*, Academic Press, 1982.

Halliwell, G.R., Jr. and J.S. Allen, 1987: "The Large-Scale Coastal Wind Field Along the West Coast of North America, 1981 - 1982," *J. Geophys. Res.*, **92**, 1861-1884.

Hickey, B.M., 1979: "The California Current System - Hypotheses and Facts," *Prog. Oceanogr.*, **8**, 191-279.

Hickey, B.M., 1989: Poleward Flow Near the Northern and Southern Boundaries of the U.S. West coast, in *Poleward Flows along Eastern Oceanic Boundaries*, Coastal and Estuarine Studies, No. 34, pp. 160-174, Springer-Verlag, New York, Inc.

Huyer, A., 1983: Coastal Upwelling in the California Current System, *Prog. Oceanogr.*, **12**, 259-284.

Huyer, A., R.L. Smith and B.M. Hickey, 1984: "Observations of a Warm-Core Eddy Off Oregon, January to March 1978," *Deep Sea Research*, **31(2)**, 97-117.

Huyer, A., 1990, *Shelf Circulation*, in The Sea, Vol. 9, J. Wiley and Sons, New York, 1990, pp. 423-465.

Huyer, A., P.M. Kosro, J. Fleischbein, S.R. Ramp, T. Stanton, L. Washburn, F.P. Chavez, T.J. Cowles, S.D. Pierce, and R.L. Smith, 1991: "Currents and Water Masses of the Coastal Transition Zone Off Northern California, June to August 1988," *J. Geophys. Res.*, **96**, 14,809-14,831.

Kosro, P.M., A. Huyer, S.R. Ramp, R.L. Smith, F.P. Chavez, T.J. Cowles, M.R. Abbott, P.T.Strub, R.T. Barber, P. Jessen, and L.F. Small, 1991: "The Structure of the Transition Zone between Coastal Waters and the Open Ocean Off Northern California, Winter and Spring 1987," *J. Geophys. Res.*,**96**, 14,707-14,730.

Kundu, P.K., J.S. Allen and R.L. Smith, 1975: "Modal Decomposition of the Velocity Field near the Oregon Coast," *J. Phys. Oceanogr.*, **5**, 683-704.

Kundu, P.K., 1976: "An Analysis of Inertial Oscillations Observed Near the Oregon Coast," *J. Phys. Oceanogr.*, **6**, 879-893.

Little, J.N. and L. Shure, *Signal Processing Toolbox, User's Guide*, Math Works, Inc., 1992.

Lopez, M., and A.J. Clarke, 1989: "The Wind-Driven Shelf and Slope Water Flow in Terms of a Local and A Remote Response," *J. Phys. Oceanogr.*, 19, 1091-1101.

Pillsbury, R.D., L.H. Pilskaln, F. Pittock, R.E. Still, 1992: "Deep Water Flow Characteristics of Monterey Bay: A Two Year Current Meter Data Set," Data Report 143, Ref. 92-2, August, 1992, College of Oceanography, Oregon State University, Corvallis, Oregon.

Ramp, S.R., P.F. Jessen, K.H. Brink, P.P. Niiler, F.L. Daggett, and J.S. Best, 1991: "The Physical Structure of Cold Filaments Near Point Aren California, during June 1987," *J. Geophys. Res.*, **96**, 14,859-14,883.

Ramp, S.R., N.A. Garfield, C.A. Collins, L.K. Rosenfeld, F.B. Schwing, *Circulation Studies Over the Continental Shelf and Slope Near the Farallon Islands, California*, Executive Summary, Naval Postgraduate School, Monterey, California, 1992.

Robson, A.J., *Circulation of the California Undercurrent Near Monterey in May 1989*, Master's Thesis, Naval Postgraduate School, Monterey, California, June 1990.

Romea, R.D. and J.S. Allen, 1983: "On Vertically Propagating Coastal Kelvin Waves at Low Latitudes," *J. Phys. Oceanogr.*, **13**, 1241-1254.

Tisch, T.D., *Seasonal Variability of the Geostrophic Velocity and Water Mass Structure Off Point Sur, California*, Master's Thesis, Naval Postgraduate School, Monterey, California, September 1990.

Tracy, D.E., *Source of Cold Water at Monterey Bay Observed by AVHRR Satellite Imagery*, Master's Thesis, Naval Postgraduate School, Monterey, California, December 1990.

Wallace, J.M. and R.E. Dickinson, 1972: "Empirical Orthogonal Representation of Time Series in the Frequency Domain Part I: Theoretical Considerations," *J. Applied Met.*, **11**, 887-892.

Wickham, J.B., A.A. Bird, and C.N.K. Mooers, 1987: "Mean and Variable Flow Over the Central California Continental Margin, 1978-1980," *Continental Shelf Res.*, **7(8)**, 827-849.

Wilkin, J.L., and D.C. Chapman, 1990: "Scattering of Coastal-Trapped Waves by Irregularities in Coastline and Topography," *J. Phys. Oceanogr.*, **20**, 396-421.

Winant, C.D., R.C. Beardsley, R.E. Davis, 1987: "Moored Wind, Temperature, and Current Observations Made During Coastal Ocean Dynamics Experiments 1 and 2 Over the Northern California Continental Shelf and Upper Slope," *J. Geophys. Res.*, **92**, 1569-1604.

Wooster, W.S., and J.L. Reid Jr., *Eastern Boundary Currents*, in The Sea, Vol. 2, M.N. Hill, New York, 1963, pp. 253-280.

INITIAL DISTRIBUTION LIST

No. Copies

1. Defense Technical Information Center   2
   Cameron Station
   Alexandria, VA 22304-6145

2. Library, Code 52   2
   Naval Postgraduate School
   Monterey, CA 93943-5000

3. Chairman (Code OC/Co)   1
   Naval Postgraduate School
   Monterey, CA 93943-5000

4. Chairman (Code MR/Hy)   1
   Naval Postgraduate School
   Monterey, CA 93943-5000

5. Dr. S. R. Ramp (Code OC/Ra)   5
   Naval Postgraduate School
   Monterey, CA 93943-5000

6. Dr. L. K. Rosenfeld (Code OC/Ro)   1
   Naval Postgraduate School
   Monterey, CA 93943-5000

7. Dr. C. H. Pilskaln   1
   Monterey Bay Aquarium
   Research Institute
   160 Central Ave
   Pacific Grove, CA 93950

8. Commandant (G-PO-2)   1
   U.S. Coast Guard
   Washington, D.C. 20593

9. Dr. M. Noble   1
   U.S. Geological Survey
   345 Middlefield Road, MS 999
   Menlo Park, CA 94025

10. Dr. T. Kinder   1
    Office of Naval Research, Code 1122CS
    800 N. Quincy Street
    Arlington, VA 22217

11. Superintendent (ds)   1
    U.S. Coast Guard Academy
    15 Mohegan Avenue
    New London, CT 06320-4195